Development and Applications of Coherent Imaging with Improved Temporal and Spatial Resolution

Rajmund Mokso

To cite this version:

Rajmund Mokso. Development and Applications of Coherent Imaging with Improved Temporal and Spatial Resolution. Physics [physics]. Université Joseph-Fourier - Grenoble I, 2006. English. NNT : . tel-00255334

HAL Id: tel-00255334
https://theses.hal.science/tel-00255334

Submitted on 13 Feb 2008

EUROPEAN SYNCHROTRON RADIATION FACILITY
UNIVERSITÉ JOSEPH FOURIER-GRENOBLE I

THÈSE
présenté par
Rajmund Mokso

Pour obtenir le grade de
DOCTEUR DE L'UNIVERSITÉ JOSEPH FOURIER
discipline: Physique

Development and Applications of Coherent Imaging with Improved Temporal and Spatial Resolution

2006

composition du jury:

Prof. J. Chevrier	Université Joseph Fourier	Président
Dr. A. Renault	CNRS Rennes	Rapporteur
Prof. T. Salditt	Universität Göttingen	Rapporteur
Dr. F. Polack	Synchrotron SOLEIL	Examinateur
Dr. F. Graner	Université Joseph Fourier	Invité
Dr. J. Baruchel	ESRF	Directeur de thèse
Dr. P. Cloetens	ESRF	Directeur de thèse

Dedicated to
my mother

Life is like riding a bicycle. To keep your balance you must keep moving
-Albert Einstein-

Acknowledgements

There were several reasons for which I decided to start a PhD at the ID19 at ESRF. One of the main expectation was to finally be able to do a real team work. I am glad to state that I have not been disappointed. Peter has always chosen people who it was the greatest pleasure to work with. And so I come to the main point of this short acknowledgment. I know that I would have had long abandoned the idea of completing a PhD study not having Peter Cloetens for my supervisor.

Many researchers tend to produce papers which look at a given problem in a more complicated way than it has been proposed before. This is certainly not the case of Jean-Pierre, my office mate throughout the whole three years. But what more, Jean-Pierre has explained me very often complicated things in a simplified way and pushed me t new results often by inviting me to participate in the development of his great ideas.

I would like to express my warm thank-you to Jose Baruchel, who as far as my PhD thesis concerns, has always used his competences as group leader to help me in all including administrative and interpersonal matters.

Thank-you to my examiners, J. Chevrier, A, Renault, T. Saldit, F. Polack and F. Graner for managing to read the whole thing so throughly and for the surprisingly pleasant thesis defense. I have in addition very much appreciated the plentiful comments of F. Polack on the presented manuscript and I hope I have succeeded to incorporate them in this corrected version.

The whole ID19 group was a place I would recommend to do a PhD to anyone. I tell you at least one good reason. There is usually a period of increasing pressure towards the end of the 3 years. In this situation I was so pleased to experience that the offers to help me from the side of people in the offices near me were more then I had the capacity to really use. And all this without asking anybody... Who would not be delighted with this approach? Special thanks to Wolfgang, also for introducing me to “ski de randonee” and taking me to experience the flight in his sail plane. One of my first contact in Grenoble was with the family of Petra during the first 3-4 days I have spent in their house. This was an important moment for me. Lukas was too quick in downhill when it was mountain biking time, but maybe if I get a better bike I will one day keep closer to him. Sabine was always there when needed any help, I think she would even give me her whole computer if I wanted to. And finally it would be difficult to not to mention Elodie, with a spirit of keeping together the most of the ID19 team and acting naturally in so many situations. It is impossible for me to imagine somebody else on her place at ID19, but I hope that wherever I will work next, there will be a person at least a little similar. Thanks to

Pascal, who put together the whole focusing system and many other things, it is nice to have around somebody with his patience when I put a block of aluminum upside down for example.

Carlos and Imma from tbe University of Zaragoza are the two people standing behind the practical realization of fast tomography. I realy liked to be with them during their short visits at ESRF. I wish our plans would have came true concernant my eventual stay in Zaragoza.

Let me now come to two groups of people each being essential for the results in my thesis.

First the “foam people”. Jerome Lambert and the whole group in Rennes is so nice to work with. Moreover for Jerome it also applies that he offered me more help than I was able to use during the intensive period of writing the manuscript. Certainly the best school/course I ever took part was the winter school on foams organized by Francois Graner et al. With people like Jerome, Francois and James it is so easy to get passionate with any kind of research, being it foams or other subject. Thanks to these people I learned that foams are more interesting than I could imagine before.

The second group to express my gratitude is the one from the INSA Lyon. Eric Maire and Jean - Yves Buffiere is just a big fun to do an experiment with, even when it is the Xth night without proper sleep. I have admired their ability to take the things with such a nice approach and still so professionally.

An essential background for all my stay in Grenoble has been provided by my friends with who I shared the house in Fontaine. The first two boys, Christoff and Yvon were so entertaining and though often (for my nature) too eager to make a big party in the house, there can be no doubt that they kept the spirit of the house in Fontaine to what it was famous for. And thanks to Alex and Elsa this spirit has not disappeared even after The two boys have left the house.

Jarda, Michal, Aaron, Mathiew, it was so nice to be able to enjoy what nature provided for people who come to see around Grenoble.

I hope I will be of at least half that useful for Froydis when she will be completing her degree as she was to me. Or at least as pleasant?

The last word has often the biggest weight. I reserved the last line of the acknowledgment to express the importance of every single action and thought of my mother during the last three years and just as well before. The same stands for what concerns my grandfather who would be very happy if he could see me now.

More and more people are coming to my mind who I should include in this list, but all must come to an end some time (and this must be really true, if even this manuscript came to this stage).

Contents

Introduction en français

L'Installation Européenne de Rayonnement Synchrotron à Grenoble (ESRF) est une source de rayons X de troisième génération. Le faisceau de rayons X de cette source, partiellement cohérent et avec une brillance élevée est un outil très favorable pour l'imagerie à haute résolution spatiale et temporelle. Couplé avec la technique tomographique, il nous permet de visualiser la structure tridimensionelle de objects divers.

Le travail qui suit se subdivise en deux grandes parties. Dans la première partie nous décrivons les modifications faites sur la ligne de lumière ID19 de l'ESRF, pour rendre la tomographie plus efficace et en conséquence plus rapide. La nouvelle configuration nous a permis d'effectuer une expérience unique sur les mousses liquides - un système dynamique. La deuxième partie traite de l'autre aspect de la tomographie, la résolution spatiale. Avec un système optique pour la focalisation des rayons X, nous avons amelioré la résolution spatiale en tomographie. Les premières images tomographiques ont été acquises avec ce système de tomographie avec grandissement, et présentent une résolution de 290 nm.

Ce mémoire s'organise de la façon suivante:

Le chapitre 1 rappelle les bases physiques essentielles pour comprendre la suite.

Au chapitre 2 et Annexe nous présentons la théorie de formation d'une image dans une faisceau partiellement cohérent. L'Annexe contient un article qui décrit une méthode de mesure de la longueur de cohérence transverse du faisceau.

Le chapitre 3 traite d'un aspect plus technique de la tomographie: l'augmentation de la vitesse d'acquisition tomographique pour pouvoir suivre en 3D les systèmes dynamiques.

Le chapitre 4 présente les résultats d'expérience avec les mousses liquides en 3D. La corrélation entre les mesures effectuées sur images microtomographiques tridimensionelles et les résultats des simulations recemment publiés, est étudiée. L'évolution des paramètres pour deux mousses différentes est analysée.

Le chapitre 5 donne une description du système optique constitué par deux miroirs en géometrie dite de 'Kirkpatrick-Baez'. La stabilité thermique et les principes de l'imagerie avec ce type de système sont traités.

Le chapitre 6 est consacré aux applications à très haute résolution spatiale. La tomographie avec grandissement requiert quelques modifications des méthodes de reconstruction de la phase. La méthode optimale de reconstruction de la phase est présentée dans ce chapitre pour deux types d'échantillon. Sur le dernier exemple, l'évolution des particules pendant une traitement thermique est étudié.

Ce travail a pour ambition d'améliorer la résolution temporelle et spatiale de la tomographie aux rayons X durs.

Introduction

The goal of x-ray computed tomography is to reveal the internal structure of an object by x-raying it from many different directions and then by mathematical methods combining all these projections into a final three dimensional image. If all goes as foreseen, the result prevents to cut the object in order to 'look inside'. This was, throughout the history an ever growing desire of mankind, because the understanding of the internal structure of materials had, and will answer many questions both scientific and driven by pure curiosity. Sometimes the two latter may be coupled and perhaps this has been the motor for us to challenge the resolution (spatial and temporal) in imaging with x-rays.

This work has a twofold goal. Firstly to gain insight into the bulk of certain materials at a spatial resolution superior to what has been achieved so far and secondly to improve the speed at which tomography can be performed. The common point for the two is hence the tomography.

The spatial resolution with laboratory x-ray sources has achieved remarkable results in the last decade. Commercially available systems routinely offer spatial resolutions close to a few micrometers. Very recently even sub-micrometer resolution laboratory systems are reported. The image quality is however often poor when imaging real materials. In this work we also address sub-micrometer resolution in tomography but with 3rd generation synchrotron radiation x-ray beams that do offer additional possibilities to those used in laboratory setups.

The unique properties of the x-rays emerging from an instrument such as the European Synchrotron Radiation Facility (ESRF) allow to develop and implement state-of-art instruments, a tool for applications that can hardly be addressed elsewhere with the same resolution (in many senses of the word). The current limit in spatial resolution at the synchrotron sources imposed mainly by the x-ray detector is of the order of $1\,\mu$m. The ID19 beamline at the ESRF is 145 m away from the source, which when taking into account the opening angle of the beam provides an x-ray beam well adapted to imaging in its dimension and coherence properties. Yet another aspect of the beamline design was important in our work. From optics, the demagnification of an optical system is given by the ratio of the object and image plane distances. If one introduces focusing optics in the path of the beam, a de-magnified, "new" source can be created and the beam will be divergent instead of parallel. When putting an object into such a divergent beam a small distance from the focal plane and the detector further downstream, we observe a magnified image on the detector. Hence the spatial resolution is no longer determined by the detector pixel size, but rather by the quality of the beam, the stability and the precision of the mechanics. Moreover we have put as a goal to combine projection microscopy with tomography, so the requirements are even stronger on the stability and beam quality, in consequence these became one of the principal challenges in the work here presented.

To all the above said there comes another factor whose importance is growing, given by the orientation of today's society. The time. Things must be done as fast as possible and preferably without loss of quality. This, coupled with the desire for higher efficiency and the interest in physical systems that exhibit fast evolution was the inspiration for us to address the temporal resolution in tomographic acquisition. Returning once more to laboratory sources, the acquisition time for a complete tomographic set at a resolution of few micrometers is of the order of hours. At synchrotron sources the situation is far better because of the available high flux of x-ray photons. In spite of this, only 2-3 years ago it was difficult to achieve at ID19 acquisition times shorter than 2-3 minutes. The reason was the ineffective way of the communication between the individual units in the tomographic chain. It was truly a chain as all occurred sequentially rather than in parallel.

The parallelization of the acquisition process, by distributing intelligent units that are synchronized by hardware signals is the ultimate goal. One part of this process is presented in this work. The successful way of synchronization has brought its fruits also in the form of unique experimental results on three-dimensional liquid foams. Liquid foams are systems that require fast data collection during tomography because of their evolution. In spite of the apparent simplicity of this system, their behavior in three dimensions is not yet fully understood. It is certainly not the main motivation for the foam community but from detailed astronomical studies of the Universe the following picture begins to emerge from redshift surveys:

“The 3-dimensional distribution of luminous matter has a "soap-bubble" appearance, with the visible galaxies mostly on the surface of these soap bubbles.

The superclusters appear as elongated strands where different soap bubbles come together.”

One, much more important motivation was to reveal the existence of a so-called scaling state of the foam in which the evolution can be compared to “zooming” through time meaning that the distributions of relative parameters (such as relative bubble volume or mean number of faces, etc.) are constant in time. The key experimental results on this subject are presented in this work which is organized as follows.

Chapter 1 is a short trip into the physics relevant for the thesis.

Chapter 2 and the Appendix focus on a key property of synchrotron radiation, the coherence. An overview of phase retrieval methods is provided to help the understanding of the manner the results in later chapters have been obtained. The Appendix is a common article that presents a novel way of measuring the degree of coherence of a synchrotron beam using the partial Talbot effect.

Chapter 3 is more technical and presents the modifications in the tomographic acquisition chain at the ID19 beamline. The message from this chapter are the parameters for the optimal setup for experiments on 3D liquid foams.

Chapter 4	contains the experimental results and interpretations on the imaging of liquid foams. The principal goal was to get as close as possible to the scaling state and to access the various characteristic distributions for three dimensional foams with statistics not available from earlier experimental studies.
Chapter 5	starts with an overview of focusing methods for x-rays, leading to the description of the instrument that uses two mirrors in cross-geometry to provide a two-dimensional focus. The thermal stability, the distortion of the wavefront due to mirror imperfections and the principle of imaging with such an instrument form the core of this chapter.
Chapter 6	contains the first scientific applications with the focusing system. Aluminum alloys have been scanned using the magnified tomography, yielding sub-micrometer spatial resolution. The two types of samples here analyzed require two different approaches from the point of view of phase retrieval. The optimal phase retrieval procedures are described and resulting phase maps presented as well as the three-dimensional reconstruction of a static and an annealed sample. On the latter the evolution of particles can be followed at a resolution not reached earlier.

Summing up, we made the parallel beam divergent and the sequential scanning process parallel.

CHAPTER 1

X-ray imaging

1. The source: synchrotron radiation

It was the community of heavy particle physicists who constantly had to deal with the unpleasant parasitic radiation emerging from relativistic accelerated charged particles of energy $E = \gamma mc^2$, with $\gamma \gg 1$ and m being the rest mass on circular trajectories created by a magnetic field. Thick shielding walls had to be built to absorb the very intense radiation that in addition had a relatively big penetration depth as a consequence of it's short wavelength. Finally in the seventies the opinion on the parasitic nature of this x-ray radiation changed when it became available for condensed matter physicists. It has been proven since then again and again that this moment was an important milestone in material research utilizing x-rays. From then on around the ring there were not only the mentioned heavy particle scientists, but an increasing number of x-ray scientists as well. Even before this new group of x-ray scientists achieved a generation change the ring was one head in front and in the eighties the second generation of dedicated synchrotron facilities had seen the daylight. In 1993 the first photons were produced by ESRF, a 3rd generation source. By "3rd generation" it is referred to storage ring architecture with extensive use of straight sections for insertion devices and typically low emittance. Today we have several high brilliance 3rd generation synchrotrons and new projects to further increase the brightness of X-rays for material research (see figure 1 for the timeline of x-ray sources development)

A single figure-of-merit called the **brilliance** allows to compare the quality of different X-ray sources combining the photon flux, the collimation of the beam and the source dimension. We can write $brilliance = \frac{brightness}{s_x s_y}$, $s_x$and s_y being the dimensions of the transverse area of the source and the **brightness** being defined as (Raoux, 1993)

$$(1) \qquad B(photons/sec/mrad^2/\frac{\Delta\lambda}{\lambda} = 10^{-3}) = 1.327\, 10^{13} E_p^2\, [GeV]\, I\, [A]\, H_2(\frac{\lambda_c}{\lambda})$$

E_p is the particle energy, I the current stored in the storage ring and H_2 a dimensionless function of the reduced variable $\frac{\lambda_c}{\lambda} = \frac{\omega c}{\omega}$. This function has a broad maximum around the critical wavelength (see next paragraph) and drops rapidly when $\frac{\lambda_c}{\lambda} \gg 1$. For nonrelativistic accelerated charges the energy flux is emitted isotropically around the acceleration, in a large solid angle. At relativistic energies the radiation pattern becomes sharply peaked in the direction of motion of the radiated charge because of the relativistic space-time Lorentz transformations.

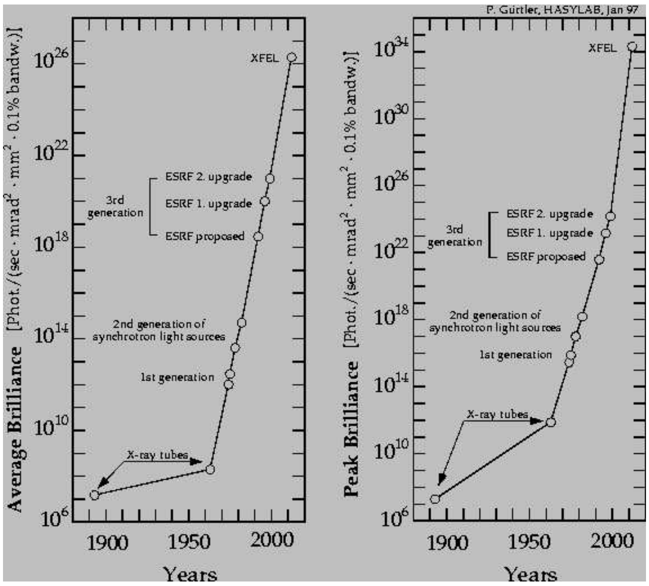

FIGURE 1. The evolution of the brilliance of x-ray sources since the discovery of x-rays in 1895

Following the classical treatment by Jackson (Jackson, 1975), the light emitted at angle θ' relative to the direction of motion of the charged rest frame is viewed at an angle θ in the laboratory frame such as:

$$\tan\theta = \frac{\sin\theta'}{\gamma(\beta + \cos\theta')} \approx \frac{1}{\gamma}\tan(\frac{\theta'}{2})\ (since\ \beta \approx 1) \tag{2}$$

At $\theta' = 90°$, we get $\theta \approx \tan\theta \approx 1/\gamma$. Thus $1/\gamma$ is the typical opening angle of the radiation in the laboratory frame. In practice this means a typical aperture of $80\ \mu rad$ for a $6\ GeV$ electron (or positron) source ($\gamma = 1957\, E\, [GeV]$). Because of the circular trajectory of the electrons this collimation is only preserved along the direction perpendicular to the plane of the orbit, usually the vertical one.

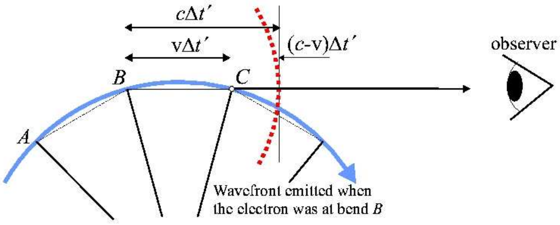

FIGURE 2. Spectral properties of the bending magnet radiation. A stationary observer only receives the radiation as it traverses an arc between points B and C.

The qualitative explanation of the spectral characteristics is presented in figure 2. An observer O, located far away from the particle only receives the radiation produced by the particle as it traverses an arc of angle about $2/\gamma$ as a consequence of the natural collimation of synchrotron radiation. If R is the radius of the curvature, the duration of this pulse is

$$2\tau = \frac{4}{3}\frac{R}{c\gamma^3}, \tag{3}$$

hence the radiation from a synchrotron has pulsed character and this can be used for performing time resolved measurements. τ is referred to as the characteristic (critical) time scale of synchrotron radiation. To this corresponds the critical frequency ω_c and wavelength $\lambda_c = 2\pi c/\omega_c = c\tau$ emitted by the broad white beam. These values are defined so that the half of the total power is radiated at frequencies higher than the critical one. In practical units, for the critical energy we have:

$$E_c = \hbar\omega_c = 0.665\,BE_p^2 \; and \; \lambda_c = 18.64/BE_p^2 \tag{4}$$

where B is the magnetic field which deviates the particle trajectories.

As noted the collimation in horizontal direction is not preserved in the bending magnet case. But, in the straight sections, by imposing an alternating (in polarity and in space) magnetic field in the direction perpendicular to the plane of motion the collimation of emerging radiation can be preserved in both directions enhancing thus the flux/brilliance of the X-ray beam. The forced wiggling motion of electrons results in emission of radiation at each individual wiggle and the observer on the axis of the device receives a power $2N_w$ times higher than in the bending magnet case if N_w is the number of periods. These devices are installed in the straight sections of the storage ring of third generation synchrotrons. We shall now briefly characterize the Wigglers and Undulators also because all the experiments in this work (except the measurement of coherence by means of the Talbot effect) were performed with radiation from insertion devices.

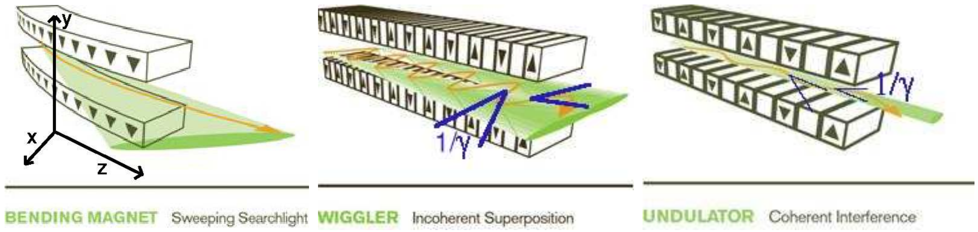

(a) (b) (c)

FIGURE 3. Schematic picture of bending magnet (a) multipole wiggler (b) and undulator (c) regime. The insertion devices are based on an alternating magnetic field. The difference in the performance of the two insertion devices arises from the difference in the opening angle of the electron oscillation in the horizontal plane. The radiation cone of an undulator is compressed by the factor $1/\sqrt{N_w}$.

The axis of the wiggler magnet is parallel to the unperturbed electron motion in the given straight section and the alternating magnetic field of period λ_W in the z-direction is to a good approximation sinusoidal. The maximal deflection, α_e of the electrons in the horizontal plane is expressed by means of a dimensionless *field strength parameter* K as $\alpha_e = K/\gamma$ and

$$K = 0.93 B_W \,[T]\, \lambda_W \,[cm] \tag{5}$$

The K value will determine the character of the radiation emerging from an insertion device. $K \gg 1$ results in a large amplitude of angular deviation K/γ of the particles and it is referred to as a multipole wiggler device shown in figure 3(b). The intensities from the wiggles are summed up and the spectrum of resulting radiation is the same as the bending magnet spectrum only the intensity is higher.

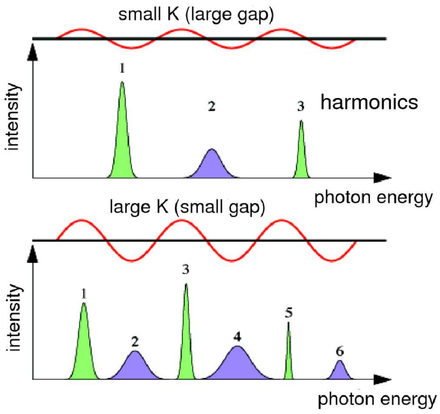

FIGURE 4. The Undulator spectrum can be tuned by changing the gap which by means of equation 5 influences the K value. A larger gap implies a lower magnetic field and a higher energy of the harmonics.

It is also possible to bring in phase the emitted radiation from consecutive wiggles. This is the case of undulators (figure 3(c)) where $K \leq 1$ and the cone of the beam is compressed by a factor $1/\sqrt{N_W}$. Due to the transverse deflection, the average electron velocity divided by the speed of light is

$$\beta_e \simeq 1 - \frac{1 + K^2/2}{2\gamma^2} \tag{6}$$

Two wavefronts emitted by an electron passing through multiple periods of the magnet follow each other by a time interval

$$T_1 = \frac{\lambda_W}{\beta_e c} - \frac{\lambda_W}{c} \tag{7}$$

and an observer downstream the magnet looking in the forward direction sees a radiation spectrum comprised of the fundamental frequency $\omega_1 = 2\pi/T_1$ and its odd harmonics. Away from the forward direction, the radiation spectrum is comprised of both, odd and even harmonics of the fundamental frequency. By Krinsky (Krinsky, 1983) the brillance of the first harmonic of an undulator may be approximated as

$$B_{u1} \cong \frac{2.10}{\varepsilon_x \varepsilon_y} \frac{N_w K}{1 + K/2} \tag{8}$$

Undulators may be tuned as explained in figure 4. Different harmonics are used depending on the energy or peak intensity required in the experiment. From the formula 8 it is seen that to achieve high brillance, we need small electron beam emittance ε_x and ε_y. These vary quadratically with electron energy γ therefore the emittance can be reduced by lowering the energy. However the photon energy is $\sim \gamma^2/\lambda_w$ so the undulator period λ_w must be decreased with the energy to maintain the hardness of the radiated spectrum. Some key characteristics related to this discussion are listed in table 1 for the three comparable synchrotron sources, ESRF, APS and SPring-8

	ESRF	APS	SPring-8
E(GeV)	6	7	8
γ	11.74	13.7	15.66
ε_x(mm.rad)	3.7	3.9	6

TABLE 1. Representative parameters for the 3rd generation synchrotron sources ESRF, APS and SPring-8.

For the experiments described in this work, we used the undulator and wiggler radiation of ID19 beamline at ESRF.

2. X-ray interactions with matter

The analysis of any experiment in which a sample is involved can not be complete if one or more important processes contributing to the measurement are omitted or not well understood. Therefore a brief overview of the processes involved when radiation is incident on a sample is useful.

The four principal kinds of x-ray interactions with matter are

- Photoelectric effect and emmission of fluorescent radiation. The energy of a photon is completely absorbed by an atom and the photon disappears. An electron is ejected with the energy of the incident photon minus the binding energy of the electron in the atom. After the electron is removed from an internal shell (generally K or L), an X-ray photon can be emitted. These characteristic x-ray photons are emitted isotropically and are called fluorescence photons.
- Rayleigh scattering (elastic scattering). Photons are deviated from their initial direction without the loss of energy. This is strongly forward directed.
- Compton effect (inelastic scattering). The incident photon has an inelastic shock with an electron. The photon transfers a part of its energy to the electron. The photon is scattered and the electron obtains kinetic energy.
- Pair creation. This interaction involving the annihilation of the photons appears when the incident energy is above 1.02 MeV, and they are not relevant for our experiments.

One advantage of sub-100 keV x-rays is that the dominant interaction mechanisms with matter are absorption and coherent scattering. Contributions from incoherent scattering can be neglected because of its small cross section at these energies. In addition, multiple scattering is unlikely since the cross section σ_{coh} for coherent scattering is much smaller than that for photoelectric absorption σ_{abs}. With these assumptions, the theoretical treatment of x-ray interactions with an atom is rather simple. Following an approach by Henke (Henke, 1981), taking the ratio of the incident and radiated beam intensity and integrating the *differential* cross-section over all scattering angles the *total* cross-sections for *Thomson scattering* can be expressed as

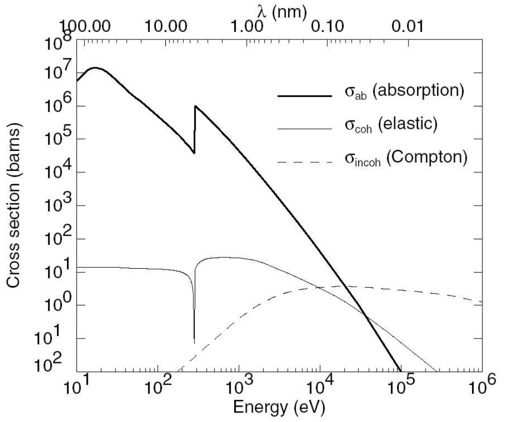

FIGURE 5. Photon cross section in carbon as a function of energy illustrated which process is important at the given energy.

$$\sigma_{coh} = \frac{8}{3}\pi r_e^2 (f_1^2 + f_2^2) \tag{9}$$

$$\sigma_{abs} = 2 r_e \lambda f_2 \tag{10}$$

where $r_e = \frac{e^2}{4\pi\varepsilon_0 mc^2} \simeq 2.8\, fm$ is the classical electron radius (or the Thomson scattering length), f_1 and f_2 are the so called dispersion corrections. If Z is the atomic number, then $f(\omega) = Z + f_1(\omega) + i f_2(\omega)$ is the *complex atomic scattering factor*; $Z + f_1$ is usually associated with the refraction and f_2 with absorption. This latter is the proportionality factor for the attenuation of the intensity $I(z)$ by absorption

$$-dI = I(z) N(dz) \sigma_{abs} \tag{11}$$

then instead of the total number $N(V)$ of atoms per cm^3 we write $\frac{\rho_m N_A V}{A}$ with N_A, ρ_m and A the Avogadro's number, the mass density, and the atomic mass number, respectively. Through the substitution

$$\mu = \frac{\rho_m N_A}{A} \sigma_{abs} \tag{12}$$

we write the solution of 11 with boundary condition $I(z=0)=I_0$ to obtain the the usual form of the *Beer-Lambert law*

$$I(z)=I_o e^{-\mu z} \tag{13}$$

μ is referred to as the linear attenuation coefficient.

When instead of the intensity we regard the wave function in the media traveling a distance Δz described as $u(P)=u_0(P)e^{ink\Delta z}$, where $k=\frac{2\pi}{\lambda}$ is the wave vector and n is the refractive index, the Born approximation (Born and Wolf, 1990) gives the value of refractive index decrement δ for all electrons in the atom:

$$1-n=\delta=\frac{\lambda^2 N_A \rho_m r_e}{2\pi}\frac{\sum_i N^{(i)}(f_1^{(i)}+Z^{i)})}{\sum_i N^{(i)}A^{(i)}} \tag{14}$$

Finally by writing the wave function in terms of the complex refractive index $n=1-\delta+i\beta$ as $e^{i(1-\delta)k\Delta z}.e^{-\beta k\Delta z}$ where $\beta=\frac{\mu}{2k}$, it becomes clear that the δ is responsible for the phase shift $\varphi=-\frac{2\pi}{\lambda}\int\delta dz$ and β for the amplitude attenuation. Though β is expressed through the imaginary part of f and δ through its real part, they are not independent. The knowledge of one over the whole energy range will determine the other through the Kramers-Kronig relations (Jackson, 1975). As the function of energy they will then determine the fraction $\beta/|\delta|\propto E^{-2}$. Far from absorption edges, it is useful to introduce an approximate form for the refractive index decrement using the density of the object, ρ_m,

$$\delta\approx 1.36\times 10^{-6}\rho_m[g.cm^{-3}]\lambda^2[\text{Å}] \tag{15}$$

The effect of refraction can be several orders more pronounced than the attenuation effect. Moreover high energies mean less deposited dose $\beta\propto E^{-4}$. The last two statements bring up the advantages of phase contrast imaging. However this imposes requirements on the light source and the imaging system, moreover not in all cases the phase contrast is beneficial as will be discussed in the next section.

3. Coherent vs. incoherent imaging

The *coherence* is the property of a signal or data set in which the phase of the constituents is measurable and plays a significant role in the way in which several signals or data combine. This term is also used to characterize radiation in two distinct respects. The first is the *longitudinal (temporal) coherence* which is related to the monochromacity of the source. The coherence length $l_{coh}=\frac{\lambda^2}{2\Delta\lambda}$ is the distance of propagation over which radiation of wavelength λ and spectral width $\Delta\lambda$ becomes out of phase by π. The *transverse coherence* is related to the source size and its distance. Depending on the source of radiation that is used in a given imaging system we can consider two limiting cases: the spatially coherent and the incoherent case. One way of defining our system is to say that it is incoherent if the transverse coherence length is much smaller than the resolution of the images we acquire. Changing from coherent to incoherent illumination changes the blurring process substantially. A coherent imaging system has an abrupt cut-off in the frequency domain, which results in “ringing” around edges. Incoherent illumination produces a smooth drop-off in the frequency domain which blurs edges gradually. To explain this we need to consider the process of image formation in the two cases.

Under the quasi-monochromatic assumption, the wave amplitude U_i behind the (linear) imaging system is given by the convolution equation

$$U_i(x,y) = \int\int h(x-x_0, y-y_0) U_G(x_0,y_0) dx_0 dy_0 \tag{16}$$

where $U_G(x,y)$ is the wave amplitude predicted in the geometrical optics approximation and $h(x,y)$ stands for the impulse response to a point-source object. This will be our formula of depart. We will seek the formula for the intensity in the image plane.

If the illumination is perfectly incoherent, the wave behaves in a statistical manner

$$\langle U_G(x,y) U_G^*(x+\xi, y+\eta) \rangle = \kappa \sqrt{I_G(x,y) I_G(x+\xi, y+\eta} \delta_{\mathrm{D}}(\xi,\eta) \tag{17}$$

here κ is a real constant and δ_{D} the Dirac distribution. This equation is not exact, but for most practical purposes correct and simple. From here it follows for the intensity

$$\left\langle |U_i(x,y)|^2 \right\rangle = I_i(x,y) = \kappa \int\int |h(x-x_0, y-y_0)|^2 I_G(x_0,y_0) dx_0 dy_0 \tag{18}$$

thus the image intensity is found as a convolution of the object intensity I_G with an impulse response $|h|^2$. Since the intensity of any given impulse response is proportional to the intensity of the object point that gave rise to it, it follows that an incoherent system is a linear mapping of intensity. It is of interest to transform equation 18 into the Fourier domain where it takes up the form of a simple multiplication

$$\tilde{I}_i(f,g) = H(f,g) \tilde{I}_G(f,g) \tag{19}$$

The function H is called the *optical transfer function* (OTF) of the system and can be regarded as an additional weighting factor applied by the system to the frequency component at (f,g) relative to the weighting factor applied to the zero frequency component ($\tilde{I}$ and H in expression 19 are normalized by their zero frequency values). The modulus $|H|$ is known as the *modulation transfer function* (MTF).

The coherent imaging system is linear in complex field amplitude and we have to work with the amplitude instead of the intensity in the case of an incoherent source. Writing equation 16 in Fourier space it follows directly that

$$\tilde{U}_i(f,g) = P(f,g) \tilde{U}_G(f,g) \tag{20}$$

where $P(f,g) = FT[h(x,y)]$ is called the *coherent transfer function* and will be the matter of discussion in chapter 2.

We can find the relationship between P and H using the autocorrelation theorem

$$H(f,g) = \frac{\int\int P(\xi', \eta') P^*(\xi' - f, \eta' - g) d\xi' d\eta'}{\int\int |P(\xi',\eta')|^2 d\xi' d\eta'} = \int |h(x,y)|^2 e^{-i2\pi(fx+gy)} dxdy \tag{21}$$

or in a symmetrical form with $\xi = \xi' - f/2, \eta = \eta' - g/2$

$$H(f,g) = \frac{\int\int P(\xi + f/2, \eta + g/2)P^*(\xi - f/2, \eta - g/2)d\xi d\eta}{\int\int |P(\xi,\eta)|^2 \, d\xi d\eta} \tag{22}$$

This expression offers a simple and important geometrical interpretation of the OTF; the numerator represents the area of overlap of two displaced pupil functions, one centered at $(\xi + f/2, \eta + g/2)$ and the second at a diametrically opposite point $(\xi - f/2, \eta - g/2)$. The denominator normalizes this area of overlap by the total area of the pupil.

The OTF of a diffraction-limited system extends to a frequency that is twice the cutoff frequency of the coherent transfer function. It is tempting therefore to conclude that incoherent illumination will invariably yield “better” resolution than coherent illumination. In reality the situation is complex as it depends on the object itself and the information aimed for, which illumination will yield higher resolution. Incoherent imaging does not cary phase information as coherent imaging does. This already discriminates certain objects to be successfully imaged with incoherent illumination. The incoherent system is linear in intensity while the coherent one is not (its linearization with respect to different quantities allowing to simplify its dependency will be the subject of section 3.3). We can write

$$\tilde{I}_{incoh} = [P \star P][\tilde{U}_G \star \tilde{U}_G] \tag{23}$$

for the incoherent case and

$$\tilde{I}_{coh} = P\tilde{U}_G \star P\tilde{U}_G \tag{24}$$

for the coherent case, where $\star$ is the operation of autocorrelation. More considerations for the effect of the illumination type on the resolution with illustrative examples can be found in (Goodman, 1988).

In reality we always have partially coherent illumination whose quality is expressed in terms of the degree of partial coherence. It’s amplitude can be measured as detailed in chapter 3.1.

4. Detectors and the physics of detection

The detection of an object in a digital system is related to its contrast, the pixel size and the background noise.

A perfect detector should image a delta function in the object plane, the input, as a delta function in the image plane, the output and have a quantum efficiency $DQE = 1$, in other words the signal-to-noise ratio is the same at the input and at the output. Due to imperfection this is not the case in practice and the delta function is smeared out. The intensity distribution in the image plane is given by the point spread function (PSF) or in the Fourier space by its optical transfer function (OTF). Unlike truly shift invariant detectors the PSF is usually non-zero and the spatial resolution of the detector depends on it.

In imaging science it is most usual to use CCD based detectors functioning on the principle of charge transfer in a depleted region. CCD cameras are generally sensitive to the visible spectrum of radiation and for x-ray tomography a converting optics is required. This typically consists of a scintillator and a magnifying lens system. A very critical component for synchrotron imaging is the scintillator. The question in high resolution imaging is always to select the material that balances between the principal requirements imposed on the scintillator. These are:

- to maximize x-ray stopping power one needs high density ($\rho > 5$ g.cm^{-3}) and large atomic number ($Z > 50$) because the absorption in the scintillator due to the photoelectric effect is proportional to $\rho_m.Z^4$
- high x-ray to visible light conversion efficiency (> 15 visible photons per KeV) with emission wavelength well matched to the CCD readout ($550 - 650$ nm), low afterglow (four decades of magnitude over 2 ms) and linearity of the produced light with the x-ray flux
- high transmittance and no scattering
- machinable, non-toxic and mechanically strong

A very usefull overview on scintillators, x-ray detectors in general and few perspectives for synchrotron radiation has been recently published by (Martin and Koch, 2006). It was resumed that powder phosphor screens for $1\,\mu$m resolution would require grain sizes of $0.3\,\mu$m. Since this is commercially not available, thin film scintillators are essential in high-resolution X-ray imaging. They show better lateral spatial resolution than powder screens and excellent adhesion to the substrate surface.

The strongest interaction of x-ray photons with the scintillator screen for energies below ≈ 120 keV is associated with the photoelectric effect. Fluorescence generated by the photoelectric absorption limits substantially the spatial resolution for scintillator screens. Above 120 keV the Compton scattering becomes stronger and the increased mean free path of the electrons (from $2.8\,\mu$m at 20 keV for a YAG crystal up to $44\,\mu$m at 100 keV) results in the loss of efficiency and resolution.

To solve the compromise between X-ray stopping power and spatial resolution, single-crystal or polycrystalline film are used. Opportunities for improving X-ray detectors in terms of spatial resolution are somewhat limited as they are already near the theoretical limit for visible light of $0.4\,\mu$m; the best performance measured is $0.5\,\mu$m FWHM obtained with a $1\,\mu$m LAG:Eu ($Lu_3Al_5O_{12}$:Eu) thick film and 0.95 numerical aperture. Just as the idea behind our work presented in this document was to consider both sides of the imaging resolution, the same is true for the detector design. The need for fast X-ray detectors and a short exposure time to reduce the radiation dose to the samples desires increase in absorption efficiency, luminescence efficiency, and optimizing the emission wavelength for detection by the CCD camera. For soft x-ray imaging some commercially available inorganic scintillators, $Y_3Al_5O_{12}$:Ce (YAG:Ce), $CdWO_4$ and $Lu_3Al_5O_{12}$:Eu (LAG:Eu), are used as the sensor material. For hard X-ray energies scintillator with higher stopping power are necessary; Lu_2SiO_5:Ce (LSO:Ce), YAG:Ce. For various reasons, YAG:Ce and LAG:Eu are less attractive: the light yield of LAG:Eu is low and the undoped YAG substrate of YAG:Ce and LAG:Eu layers emits undesired luminescence. This luminescence is not observed for $Gd_3Ga_5O_{12}$ (GGG) scintillators. The Eu doped Gadolinium screen has a doubled luminescence efficiency compared to LAG:Eu by the equivalent absorption efficiency. The YAG:Ce have low absorption of x-rays in the range $5 - 100$ keV, but the fast decay is an important consideration for fast imaging. For its 1.2 times higher conversion efficiency than that of YAG:Ce and relatively easy mechanical processing the LAG:Ce scintillator is an attractive material (http://www.crytur.cz)

In the digitalization process the image is treated as a band-limited function its Fourier transform (FT) being zero outside a bounded region in the frequency plane corresponding to the spatial bandwidth. Aliasing occurs if the sampling frequency is lower than twice the bandwidth. The maximum observable frequency by the sampling rate b without aliasing is called the Nyquist frequency $f_N = 1/2b$, and all the frequencies above this value will be present in the sampled data and influence the spectrum between zero and f_N. The discrete sampling has three implications. The first is replications of the FT in frequency space, due to the finite sum used in the transform. The second is the overlapping of the replicated FT segments resulting from aliasing and the third is the so called "leakage" or distortion of the spectrum by the finite field of view. The replication does not have any detrimental effect on the image, but aliasing might have and has to be avoided by band-limiting the system so that no image content exists above the Nyquist frequency. Leakage can be minimized by multiplying the waveform by a window, that minimizes the transition edges of the truncated waveforms (tapers the amplitudes at each end of the full space sample).

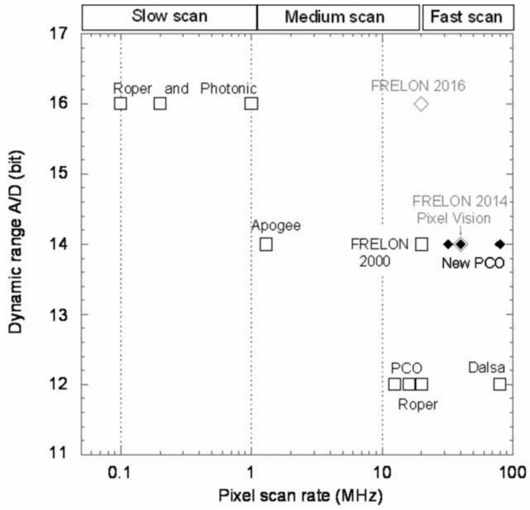

FIGURE 6. The present status of camera technology on high-resolution detectors, as function of speed vs. dynamic range. In the figure, the ESRF inhouse developped FReLoN camera is in the region of 'compromise' between frame rate and dynamic range. The cameras used only for fast tomography are typically 12 bit fast cameras, represented in the figure by the DALSA camera.

The graph in figure 6 shows that the CCD based FreLoN 2k14 detector, developed at the ESRF has a good position to suit fast scan requirements (as discussed in more detail in chapter 3 and at the meantime offers high quality images (14 bits).

5. Principles of tomography

Tomographic techniques are nowadays employed using several complementary probes including x-rays. The first ever tomographic images were obtained in 1957 by Bartolomew and Casagrande (Bartholomew and Casagrande, 1957). Cormack and Hounsfield (Hounsfield, 1972) got a Nobel price in medicine in 1979 for their work with computed axial tomography. We can say that the utilization of x-rays was in the 20th century the most important trigger of the developments in tomography. This fact is due to the property of x-rays to go through the studied sample without being completely absorbed or scattered. It allows to obtain an image of the cross section of a sample from projection data. The projections consist in this case of line integrals of the complex refractive index $n(x, y, z)$.

In 1917 Johann Radon (Radon, 1917) showed how the reconstruction from projections was possible. Cormack with his two papers in 1963 and 1964 introduced the Fourier transforms into the reconstruction algorithms (Cormack, 1963, 1964) . A simple illustration of the Fourier slice theorem, which is the bearing pillar of tomography, is highlighted in figure 7.

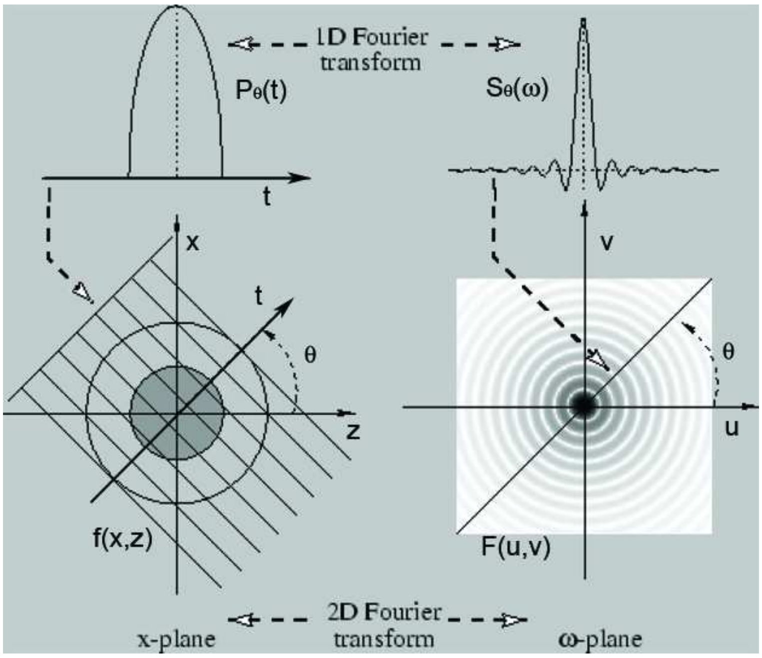

FIGURE 7. The Fourier slice theorem.

We will consider the situation of parallel projections as it is the simpler case, but in the principles not different from the fan beam case. If a slice of an object is given by the function $f(x, z)$ then the two-dimensional Fourier transform of the object function is

$$F(u,v) = \int_{-\infty}^{\infty}\int_{-\infty}^{\infty} f(x,z)e^{-i2\pi(ux+vz)}dxdz \tag{25}$$

Now we limit ourselves to one line defined in the frequency domain by $v = 0$ to split the integral into two parts

$$F(u,0) = \int_{-\infty}^{\infty}\left[\int_{-\infty}^{\infty} f(x,z)dz\right] e^{-i2\pi ux}dx \tag{26}$$

If we define a projection at an angle θ as $P_\theta(t)$ and its Fourier transform

$$S_\theta(w) = \int_{-\infty}^{\infty} P_\theta(t)e^{-i2\pi wt}dt \tag{27}$$

then the term in brackets in equation 26 can be identified as the expression for a projection along lines of constant x

$$P_{\theta=0}(x) = \int_{-\infty}^{\infty} f(x,z)dz \tag{28}$$

Substituting this formula into expression 26 we find the relationship between the 2-D transform of the object function and the vertical projection

$$F(u,0) = \int_{-\infty}^{\infty} P_{\theta=0}(x)e^{-i2\pi ux}dx. \tag{29}$$

Although derived for angle $\theta = 0$ the result is independent of the orientation between the object and the coordinate system. A projection in any arbitrary direction can be regarded as a rotation of the coordinate system by an angle θ and so the generalized result is that the Fourier transform of the projection defined by 28, is equal to the two-dimensional Fourier transform of the object along a line rotated by θ. This is the **Fourier slice theorem** (Kak and Slaney, 1987) that can be expressed also as

$$S_\theta(w) = F(w,\theta) = F(wcos\theta, wsin\theta) \tag{30}$$

if the rotation of the (x,z) coordinate system is given by the matrix

$$T_{rot} = \begin{bmatrix} \cos\theta & \sin\theta \\ -\sin\theta & \cos\theta \end{bmatrix}, \quad \begin{bmatrix} t \\ s \end{bmatrix} = T_{rot}\begin{bmatrix} x \\ z \end{bmatrix} = \begin{bmatrix} x\cos\theta + z\sin\theta \\ -x\sin\theta + z\cos\theta \end{bmatrix} \tag{31}$$

So by taking the projections at angles $\theta_1, ...\theta_n$ and Fourier transforming each of these, we can determine the values of $F(u,v)$ on radial lines (figure 9). If an infinite number of projections are taken, then $F(u,v)$ would be known at all points in the uv-plane.

Performing the integration of the inverse Fourier transform in polar coordinates gives a reconstruction formula for $f(x, z)$

$$f(x,z) = \int_0^{\pi} \left[\int_{-\infty}^{\infty} S_\theta(w)\, |w|\, e^{i2\pi wt} dw \right] d\theta \tag{32}$$

where the frequency response of the filter is given by $|w|$, which is the determinant of the Jacobian of the change of variables from rectangular to polar coordinates. Expression 32 is the basis of the **filtered backprojection** algorithm first proposed by (Bracewell and Riddle, 1967) and later extended for different beam geometries as summarized in (Herman, 1980). It analytically relates the object function $f(x, z)$, that we want to reconstruct, to the Fourier transform of the projection $S_\theta(w)$ that are obtained from the measurement by simply transforming the measured projection $P_\theta(t)$.

For better visual understanding one can refer to equation 32 in such a way that a projection $P_\theta(t)$ for a chosen θ and t (see fig.7) contributes equally to all points (x, z) which correspond to the same value t. We can say that the projection is smeared back, or backprojected over the image plane. If only one projection is taken as shown in figure 8(a), then the reconstruction in 2D will result in a rectangular form of the same width as that of the object at the selected angle.

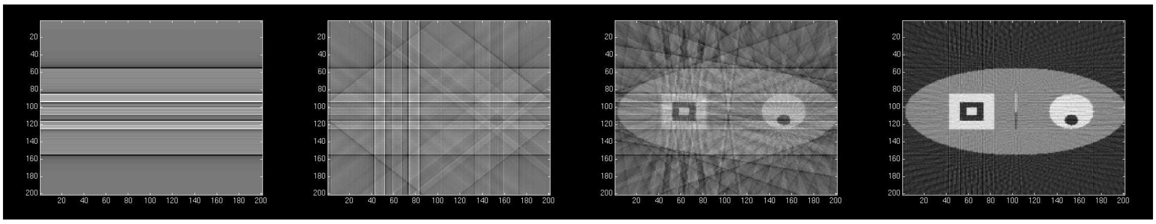

(a) (b) (c) (d)

FIGURE 8. Effect of projection angle sampling simulated by an elliptic phantom. The term 'smearing back' of a projection can also be understood from this sequence of 4 images. The first (a) is the backprojection of one single filtered projection, (b) is from 4 projections, (c) 15 and (d) 60 projections.

Since the number of projections is not infinite, the inverse Fourier transform of the functions $F(u, v)$ by means of which we aim to recover the object function $f(x, z)$ is only known along a finite number of radial lines such as in Fig. 9. One must then interpolate from this radial points to the points on a square grid that samples the (u, v) space. The density of the (measured) radial points becomes sparser as one gets further away from the center and the interpolation error to the square grid also becomes larger having the direct consequence in loosing some precision in the high frequency components in the image. This can be one source of high frequency noise in the reconstructed images.

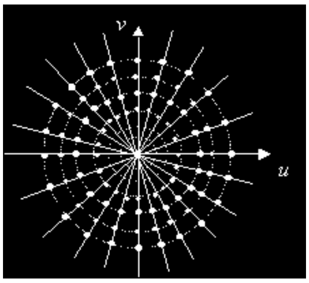

FIGURE 9. The points in (u, v) space where the Fourier components of the object are sampled from the projected data.

Staying with the idea of the Fourier slice theorem, we can consider each projection to give its contribution to the 2-D Fourier transform of the object quasi-independently. Two projections at different angle have only the DC term in common and each gives the value of the Fourier transform along a single line implying the fast inversion. If one sums all the backprojections, due to the discretization we would find a result that requires further optimization for the effect of finite angle intervals. This compensation is performed by means of a filter that is applied on the projections (or incorporated into equation 32) before they are backprojected (or smeared back to the image plane). This filter represents then the width of each wedge which of course depends on the number of projections. If multiplying the $S_\theta(w)$ function in the Fourier space by the ramp filter $|w|$, it enhances the high spatial frequencies. Many authors have proposed variations on the filter function of the filtered backprojection algorithm (Kenue and Greenleaf, 1979).

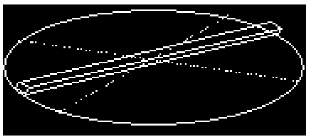

FIGURE 10. This pie-graph shows what is measured in a tomographic experiment, whereas the information that would be ideally needed is marked by the dashed line.

The algebraic reconstruction methods approach the problem from another point of view. As illustrated in figure 11, a two dimensional object plane is discretized into cells $f_1, f_2, ..., f_{n^2}$,using a single index. A cell has size $\Delta x \times \Delta z$ corresponding to the resolution of the reconstruction. Each projection line is represented by a finite width line in the figure as $P_1, P_2, ..., P_i, P_j, P_k, ..., P_M$. The width of the projection line can be interpreted in our case as the transverse resolution of the probe formed by the optics. We denote the intersection between a projection line (P_j) and cell (f_m) as w_{jm}. With this setup a discrete version of the projection integral p_j can be formulated by summing up the values of all the cells weighted by the intersection areas. In matrix form this gives

$$Wf = p \tag{33}$$

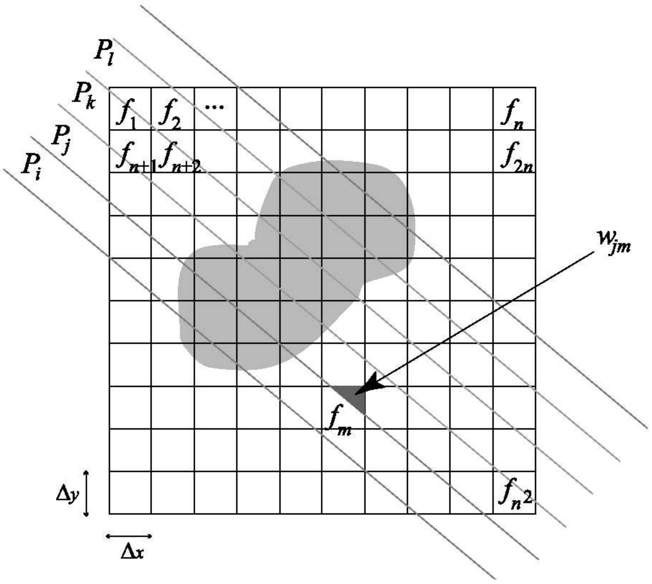

FIGURE 11. An illustration of the algebraic reconstruction technique. A ray in this case is a finite width line (resolution of the projection data) and an object is discretized into finite size cells. The projection integral of a ray can then be calculated by summing the volumes of the cells weighted by their intersection area.

For a small number of pixels one can simply find the inverse of W and reconstruct the object f from the projection p by

$$f = W^{-1}p \tag{34}$$

For a large number of pixels the inversion would be computationally not practical and iterative implemetations are an alternative.

All the above can be directly applied to reconstruct an absorption image when the incident beam is parallel as it is easy to obtain projections of $\mu(x,z)$ from absorption data. It becomes more complicated when the phase modulation is to be recovered from the experimental images and we will deal with this problem in chapters 2 and 6. The second restriction being the parallelicity of the beam is not a principal problem as the presented theory can be easily extended to fan beam geometries.

5.1. From parallel to fan beams

. The transition from parallel- to fan-beam geometry may be regarded as a weighted backprojection instead of simple backprojection as explained above for the parallel case. The reconstruction algorithms for fan-beam were derived in function of the detector geometry. The two cases are the uniform or non-uniform detector spacing. To find the expression for the projection we first need to write the relation between parallel-beam and fan-beam coordinates.

$$t = s\sin\gamma \quad and \quad \theta = \beta + \gamma \tag{35}$$

s stands for source to rotation center distance, β for angle between the central beam and the y axis connected with the sample and γ represents the angular location of a ray. We assume that β is sampled uniformly. If we stay with the notation $P_\theta(t)$ for a parallel projection taken at angle θ and $R_\beta(\gamma)$ a fan-beam projection at angle β using 35 we have

$$R_\beta(\gamma) = P_{\beta+\gamma}(s \sin\gamma) \tag{36}$$

If each projection is sampled with sampling interval α then in polar coordinates we calculate the fan-beam projections $R'_{\beta_i}(\gamma)$

$$R'_{\beta_i}(k\alpha) = R_{\beta_i}(k\alpha).s.cosn\alpha \tag{37}$$

for $k = 0, 1...N$, ($k = 0$ corresponds to the central ray). We then convolve this with the filter (a function of $n\alpha$) followed by performing the weighted backprojection where the weighting factor is determined by the position of a given pixel in polar coordinates and the projection angle β.

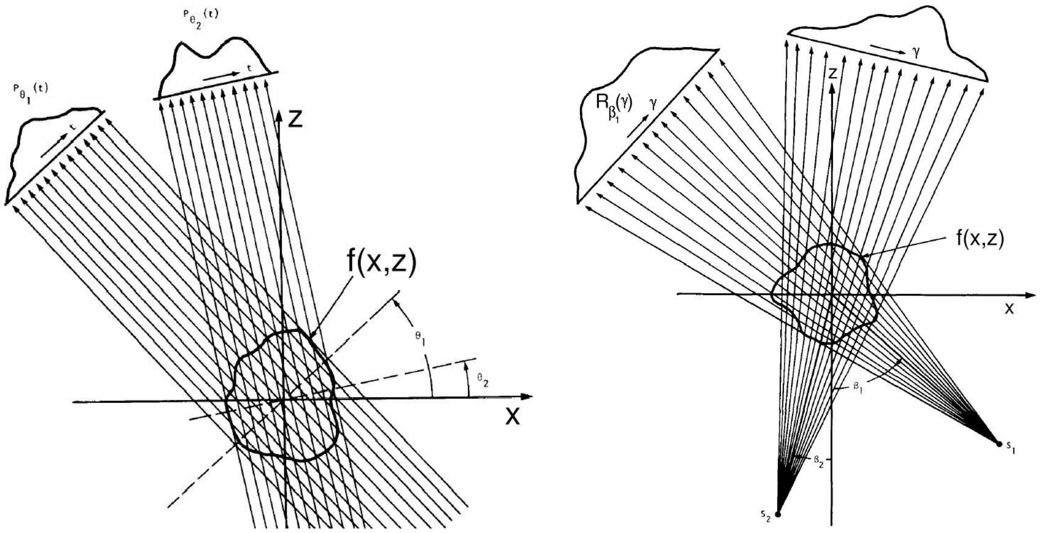

(a) (b)

FIGURE 12. Parallel (a) and fan beam (b) geometries

One last particularity of the fan-beam geometry compared to the parallel one is readily derived by considering that we have to fill the whole Radon space which is made up by ray integrals represented as points in the polar coordinate system (t, θ). For this, in the case of parallel beam, we need to measure projections from 0 to 180°, for fan-beam we have to extend this range by adding the twofold value of the maximum fan angle, γ_{max}.

In 3D cone beam geometry, an approximate reconstruction of the sample is possible by using a 2D detector, as it has been described by Feldkamp (Feldkamp *et al.*, 1984).

CHAPTER 2

Coherence and phase retrieval

1. Partial coherence and its evaluation using the Talbot effect.

Perhaps the most spectacular difference in imaging performed with a synchrotron beam compared to laboratory sources is the interference effects resulting from the spatial coherence properties of the x-ray radiation. Coherent radiation comes from a point source, which is not the case in practice, since the dimension of the source is not infinitely small. We say therefore that the radiation is partially coherent. Applications like for instance coherent scattering, require to know precisely the transverse coherence properties of the beam in order to limit the beam size impinging on the object to a coherent part.

Consider a shift-invariant imaging system with the coherent transfer function $P(x)$ and an object transmission function $T(x)$. In the case of an oblique plane incident wave (angle of incidence α) the amplitude at point x in the image plane is given by the convolution integral

$$U_\alpha(x) = \int e^{i\frac{2\pi}{\lambda}\alpha\eta} T(\eta) P(x-\eta) d\eta \tag{38}$$

In the case of an incoherent infinitely distant source, with angular profile $S(\alpha)$, the image intensity can be expressed as the sum over α

$$I(x) = \int S(\alpha) d\alpha \left| \int e^{i\frac{2\pi}{\lambda}\alpha\eta} T(\eta) P(x-\eta) d\eta \right|^2 \tag{39}$$

Performing first the integration over α we obtain the general formula for intensity in the case of partially coherent radiation in the form

$$I(x) = \int\int \rho(\eta, \eta^{'}) P(x-\eta) P^*(x-\eta^{'}) d\eta d\eta^{'} \tag{40}$$

where the complex function $\rho(\eta,\eta^{'}) = T(\eta)T^*(\eta)\tilde{S}(\frac{\eta-\eta^{'}}{\lambda})$ is the *mutual intensity* in the exit object plane. Note that $\rho(\eta,\eta)$ is equal to the usual intensity $I(\eta)$. It is also obvious that in the entrance object plane (the term T is absent) the mutual intensity is equal to the Fourier transform of the source angular distribution function, $\rho(\eta,\eta^{'}) = \tilde{S}(\frac{\eta-\eta^{'}}{\lambda})$ in agreement with the *Zernike - Van Cittert theorem* (Born and Wolf, 1990). The complex degree of coherence between two points of coordinates η and $\eta^{'}$ is the defined as

$$\gamma(\eta,\eta^{'}) = \frac{\rho(\eta,\eta^{'})}{\sqrt{I(\eta)I(\eta^{'})}} \tag{41}$$

The partial coherence defined this way is taken into account throughout this work in the interpretation of x-ray images. The profile of γ has to be determined for the given radiation source.

One elegant way of its measurement is the use of the fractional Talbot effect (Guigay *et al.*, 2004).

The *Talbot effect* (Talbot, 1836) is the self-imaging of a periodic object at distances multiple of $\frac{2a^2}{\lambda}$, a being the object period. Images at intermediate distances ($D = m\frac{2a^2}{\lambda}$, m is a rational number) have interesting properties as well and are related to the *Fractional Talbot effect*s. Appendix, is a common article where the details on the use of these phenomena to measure the spatial coherence of the x-ray beam are presented. The experimental part of the work had been planned and performed earlier and therefore my personal contribution included the refinement of the simulations and the processing of the experimental data.

2. Image formation and the inverse problem

2.1. Free space propagation

. Now that we have quantitative information about the coherence of the x-ray beam we can discuss the usage of this rather unique property of synchrotron beams. In the beginning it was often referred to as an artifact when phase contrast due to propagation was present in the images (tomographic scans). This was related to the fact that no method allowed to retrieve the phase information from the image. Now that this information can be retrieved, it brings new possibilities into x-ray imaging and ceases being just an artifact. Several methods have been proposed to reconstruct the phase and they are based on various assumptions. These assumptions can apply to the properties of the object itself but also the setup of the imaging apparatus. If the diffraction pattern is in the Fraunhofer regime, the iterative methods are the most performant, as reviewed in (Robinson and Miao, 2004). The relevant parameter to determine the region of Fraunhofer or Fresnel diffraction is the radius of the first Fresnel zone $r_F = \sqrt{\lambda D}$, D being the sample-to-detector distance in the case of plane wave illumination. If the size a of the object relates to the Fresnel zone as $a \ll r_F$ the recorded image looses resemblance to the object and the diffraction pattern is related to the square modulus of the Fourier transform of the transmitted wave and may be described by the Fraunhofer approximation. As for large distance D (and in the focal plane if the beam is focused), it is the Fourier transform that relates the object plane with the image plane, for smaller D ($a \simeq r_F$) the more general Fresnel transform should be considered

$$FRT_\kappa \left[u(x)\right] = \sqrt{-i\kappa} \int u(\xi) e^{i\pi\kappa(x-\xi)^2} d\xi \tag{42}$$

For every integrable function $u(x)$ there exists only one Fourier transform, but an infinite number of Fresnel transforms depending on the choice of the parameter κ which as we will see later has in coherent imaging the physical meaning of the inverse of defocus distance multiplied by the wavelength, $\kappa = \frac{1}{\lambda D}$.

The precise condition for the validity of the Fresnel approximation of the Fresnel-Kirchhoff diffraction integral is derived in (Born and Wolf, 1990), and relates to the paraxial approximation (small angles). If the imaging system is designed to record the Fresnel diffraction pattern on the detector, then there are various approaches to approximate the forward problem in order to be able to retrieve the phase. They are generally either be based on the *Transport of intensity equation* (Gureyev *et al.*, 2004) or the *Contrast transfer function* (Cloetens *et al.*, 1999). The approach based on the contrast transfer function will be discussed more in detail. Several solutions to the problem can be distinguished depending on the assumptions imposed on the imaged object. The different methods have been tested and adapted to the specific setup of the magnifying imaging system.

Using the Fresnel formula (42) as a starting point, it is convenient to introduce the propagator based on the property of the Fourier transform which allows to use a simple operator of multiplication between two functions whenever in the direct space these two functions are to be convolved, $FT\{T \otimes R\} = FT\{T\}.FT\{R\}$. Equation 42 may be expressed as a convolution of the object function $T(x, y)$ and the so-called *Fresnel propagator* $P_D(x, y)$

$$FRT_D\{T(x, y)\} = U_D(x, y) = P_D(x, y) \otimes T(x, y) \tag{43}$$

with the propagator in the form

$$P_D(x, y) = \frac{1}{i\lambda D} e^{i\pi \frac{x^2+y^2}{\lambda D}} \tag{44}$$

In a coherent beam case, if two images are recorded at two defocusing distances D_1 and D_2 we may shuttle between these two planes by using the above expression and if transferred to Fourier space equation 43 becomes simply

$$\tilde{U}_D(f, g) = \tilde{P}_D(f, g).\tilde{T}(f, g) \tag{45}$$

with the propagator in the Fourier domain given by

$$\tilde{P}_D(f, g) = e^{-i\pi\lambda D(f^2+g^2)} \tag{46}$$

The notation is such that the variables in the Fourier space are marked with a wave symbol above.

It is to note that the Fresnel propagator $P_D(f, g)$ is a type of coherent transfer function as derived in section 1.3 under the notation $P(f, g)$.

The quantity of interest in imaging is the intensity as this is what can be directly measured. If for the sake of simplicity the effect of detector and the partial coherence of the beam is omitted, then having an object function $T(\mathbf{x})$ we can write for the Fourier transform of the measured intensity

$$\tilde{I}_D(\mathbf{f}) = \int\int e^{-2\pi i\mathbf{f}.\mathbf{x}} \frac{1}{(\lambda D)^2} \int\int d\xi e^{i\frac{\pi}{\lambda D}(\mathbf{x}-\xi)^2} T(\xi) \int\int d\xi' e^{-i\frac{\pi}{\lambda D}(\mathbf{x}-\xi')^2} T^*(\xi') \tag{47}$$

where we used the vector notation $\mathbf{x} = (x, y)$, $\mathbf{f} = (f, g)$ and $\xi = (\xi, \eta)$. We find here the delta functions $\lambda D.\delta_{\mathrm{D}}(\xi' - \xi - \lambda D\mathbf{f})$ resulting when integrating expressions of $e^{2\pi i\mathbf{x}(-\mathbf{f}-\xi/\lambda D-\xi'/\lambda D)}$ type and the integral after rearrangement becomes

$$\tilde{I}_D(\mathbf{f}) = e^{-i\pi\lambda D\mathbf{f}^2} \int\int d\mathbf{x} e^{-i2\pi\mathbf{f}.\mathbf{x}} T(\mathbf{x}) T^*(\mathbf{x} + \lambda D\mathbf{f}) \tag{48}$$

This will be the fundamental expression for deriving the various approximations that will allow to solve the inverse problem; i.e. to find the object function from measured intensities. To write expression 48 in its more usual form it is now sufficient to substitute the spectrum of the object $\tilde{T}(\mathbf{f})$ and we immediately have

(49) $$\tilde{I}_D(\mathbf{f}) = \exp(-i\pi\lambda D\mathbf{f}^2)\int e^{-i2\pi\lambda D\nu.\mathbf{f}}\tilde{T}(\nu+\mathbf{f})\tilde{T}^{*}(\nu)d\nu$$

or

(50) $$\tilde{I}_D(\mathbf{f}) = \int \tilde{T}(\nu+\mathbf{f})\tilde{T}^{*}(\nu).\tilde{P}_D(\nu+\mathbf{f})\tilde{P}_D^{*}(\nu)d\nu$$

In a special case of small defocus distances D one can do the following manipulation. By substitution of $\mathbf{x}-\frac{\lambda D\mathbf{f}}{2}$ fort the argument of equation 48 it may be rewritten in a symmetric form

(51) $$\tilde{I}_D(\mathbf{f}) = \int\int d\mathbf{x}e^{-i2\pi\mathbf{f}.\mathbf{x}}T(\mathbf{x}-\frac{\lambda D f}{2})T^{*}(\mathbf{x}+\frac{\lambda D\mathbf{f}}{2})$$

defining $T(\mathbf{x}) = a(\mathbf{x}).e^{i\varphi(\mathbf{x})}$ and a Taylor expansion of T till first order we may write

(52) $$\tilde{I}_D(\mathbf{f}) = \int\int d\mathbf{x}e^{-i2\pi\mathbf{f}.\mathbf{x}}\left[a^2(\mathbf{x}) - \lambda D\mathbf{f}.a^2(\mathbf{x})\nabla\varphi(\mathbf{x})\right]$$

the first term is recognized as the Fourier transform of $a^2(\mathbf{x}) = I_0(\mathbf{x})$, the second as the Fourier transform of $\frac{\lambda D}{2\pi}\nabla\left\{a^2(\mathbf{x})\nabla\varphi(\mathbf{x})\right\}$ hence resulting in

(53) $$I_D(\mathbf{x}) = I_0(\mathbf{x}) - \frac{\lambda D}{2\pi}\nabla.\left\{I_o(\mathbf{x})\nabla\varphi'(\mathbf{x})\right\}$$

Expression 53 relates the change in intensity by propagation over a distance D to the derivative of the phase and is known as the Transport of intensity equation first derived twenty years ago by Teague (Teague, 1983) showing that the phase may be determined by measuring only the propagating intensity.

Approaching the image formation from the point of view of an a priori knowledge about the object it is possible to classify the different ways leading to the simplification of the expression for the intensity spectrum. Table 1 helps to simply define these approaches based on the linearization of expression 48 with respect to the selected parameter.

The first approximation applies to pure phase objects. In this case the object function is $T(\mathbf{x}) = e^{i\varphi(\mathbf{x})}$. With the condition of **slowly varying phase**

(54) $$|\varphi(\mathbf{x}) - \varphi(\mathbf{x}+\lambda D\mathbf{f})| \ll 1 \quad \forall\mathbf{x}$$

as derived in (Guigay, 1977) it is easily derived from equation 48 that the intensity spectrum takes up the form

(55) $$\tilde{I}(\mathbf{f}) = \delta_{\mathrm{D}}(\mathbf{f}) + 2sin(\pi\lambda D\mathbf{f}^2)\tilde{\varphi}(\mathbf{f})$$

method/restrictions for the object	terms appearing in the object function
pure phase object	$\varphi(\mathbf{x}), B(\mathbf{x}) = constant$
weak object	$\varphi(\mathbf{x}), B(\mathbf{x}) \ll 1$
paraboloid	$T(\mathbf{x})$ as a complex object
homogeneous object	$\beta/\delta = const.$

TABLE 1. Classification of the direct methods as a function of the object character . The second column represents the criteria imposed on the object function $T(\mathbf{x}) = e^{-B(\mathbf{x})}e^{i\varphi(\mathbf{x})}$. $B(\mathbf{x}) = \frac{2\pi}{\lambda}\int \beta dz$ stands for the absorption part and $\varphi(\mathbf{x}) = -\frac{2\pi}{\lambda}\int \delta dz$ for the phase part of the object function.

The 2D Dirac function represents for $\mathbf{f} = 0$ the mean intensity. The sinus term is called the *contrast factor* or *phase contrast transfer function*. The solid line in figure 1 shows that this term is zero for all distances $\lambda D\mathbf{f^2} = p \quad p \in \mathrm{Z}$ where the image shows no contrast.

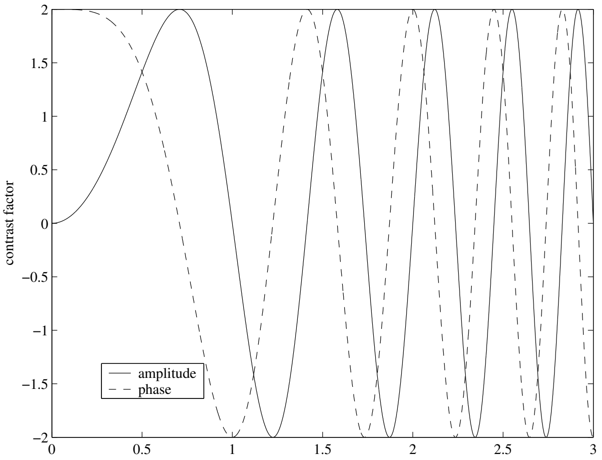

FIGURE 1. The phase and amplitude contrast factors as a function of the normalized spatial frequency $\frac{|f|}{\sqrt{\lambda D}}$ for the case of the weak object.

Next we add to the object the absorption term $B(\mathbf{x})$, but with the restriction $B(\mathbf{x}) \ll 1 \ \forall \mathbf{x}$ of a **weak object**. The object function is now $T(\mathbf{x}) = e^{-B(\mathbf{x})}e^{i\varphi(\mathbf{x})}$. In the term $T(\mathbf{x})T^*(\mathbf{x} + \lambda D\mathbf{f})$ the second order terms in $B(\mathbf{x})$ after Taylor expansion are neglected and the intensity spectrum is linearized with respect to $\tilde{\varphi}$ and $\tilde{B}$ to give (Zabler *et al.*, 2005)

$$\tilde{I}(\mathbf{f}) = \delta(\mathbf{f}) + 2sin(\pi\lambda D\mathbf{f}^2)\tilde{\varphi}(\mathbf{f}) - 2cos(\pi\lambda D\mathbf{f}^2)\tilde{B}(\mathbf{f}) \tag{56}$$

Here the cosinus term appears as multiplicative factor for the amplitude spectrum of the object, therefore it is referred to as the amplitude contrast factor. The dashed line in figure 1 shows its shape as a function of $\frac{|f|}{\sqrt{\lambda D}}$.

In a special case when the studied structure in the object is represented by only one material it is possible to couple the absorption and phase of the object and consider this variable as the term with respect to which formula 48 is linearized. For such a **homogeneous object** one has $\chi = \frac{B(x)}{\varphi(x)} = -\frac{\beta}{\delta} = constant$, where δ and β are the real and imaginary parts of the difference between the refractive index $n_1 = 1 - \delta_1 + i\beta_1$ of the material from which the object is composed and the refractive index n_2 of the material of the surrounding medium of constant thickness. The complex transmission function of the object is then

$$T(x) = e^{(i+\beta/\delta)\varphi(x)} = e^{(i-\chi)\varphi(x)} \tag{57}$$

and the intensity spectrum becomes (Turner *et al.*, 2004)

$$\tilde{I}(\mathbf{f}) = \delta_{\mathrm{D}}(\mathbf{f}) + 2\left[sin(\pi\lambda D\mathbf{f}^2) - \chi.cos(\pi\lambda D\mathbf{f}^2)\right].\tilde{\varphi}(\mathbf{f}) \tag{58}$$

As we shall see in chapter 6, there is a strong interest to impose this ratio in the reconstruction of certain samples (alloys) which we have tested.

Apart of weak scattering no special requirements have to be met for the object when calling the **Paraboloid method** (Op de Beeck *et al.*, 1996). The object transmission function $T(x)$ is decomposed into an average of the transmission function κ and it's variation $\Phi(x)$ with zero mean $T(\mathbf{x}) = \kappa + \Phi(\mathbf{x})$. Substituting the Fourier transform of the object $\tilde{T}(\mathbf{f}) = \kappa\delta_{\mathrm{D}}(\mathbf{f}) + \tilde{\Phi}(\mathbf{f})$ into equation 49 yields for Fourier transform of the intensity the following formula:

(59)

$$\tilde{I}(\mathbf{f}) = |\kappa|^2\,\delta_{\mathrm{D}}(\mathbf{f}) + \kappa^* e^{-i\pi\lambda D\mathbf{f}^2}\tilde{\Phi}(\mathbf{f}) + \kappa e^{i\pi\lambda D\mathbf{f}^2}\tilde{\Phi}^*(-\mathbf{f}) + e^{-i\pi\lambda D f^2}\int \tilde{\Phi}(\nu+f)\tilde{\Phi}^*(\nu)e^{-2i\pi\lambda D\nu f}d\nu$$

where only the last term is non-linear in $\tilde{\Phi}$, due to interference between diffracted beams; hence in the decomposition of the object we consider $\tilde{\Phi}$ as the diffracted beam component and κ as the direct, unaffected beam. The second and the third terms are linear, but they contain $\tilde{\Phi}(f)$ and $\tilde{\Phi}^*(-f) = FT[\Phi^*(x)]$ respectively, the latter being the Fourier transform of the complex conjugate of the object and results in the *twin-image problem* where both the object and its complex conjugate contribute to the calculated intensity. To solve such a problem, finite support constrains have been proposed to iteratively eliminate the twin-image contribution (Koren *et al.*, 1993).

The forward problem is well defined, and consists in computing the intensity (the Fresnel diffraction pattern) at a given image plane provided the knowledge of the object function. In principle this can be useful for the purpose of predicting the results of an experiment or to compare the recorded features with the theoretical ones. The usefulness of these calculations is in more detail shown in (Cloetens, 1999) and will also be presented in section 2.3 with the purpose to understand the behavior of the iterative approach in phase retrieval.

2.2. The holographic reconstruction by direct methods

. The inverse problem in phase contrast imaging consists in finding the phase and the amplitude of the object from the available information which is the measured intensity. This is not a trivial problem. Several solutions are to be reviewed here highlighting their applicability to the phase images recorded with the KB system. The reference will again be Table 1.

The most general case that results in analytic reconstruction of the object function is the Paraboloid method. Originating from electron microscopy (Kirkland, 1984; Op de Beeck *et al.*, 1996), and adapted to phase contrast imaging in (Cloetens, 1999), it consists of a Wiener filter approach in order to extract the linear part of image intensities. Multiplying equation 59 by the inverse propagator which is the complex conjugate of the propagator, the formula for the 'backpropagated' intensity becomes

$$(60)\quad e^{i\pi\lambda D_m f^2}\tilde{I}_m(f) = |\kappa|^2 + \kappa^*\tilde{\Phi}(f) + \kappa e^{i2\pi\lambda D_m f^2}\tilde{\Phi}^*(-f) + \int \tilde{\Phi}(\nu+f)\tilde{\Phi}^*(\nu)e^{-2i\pi\lambda D_m \nu f}d\nu$$

We introduced D_m instead of D meaning multiple defocus distances. The decomposition 60 will help to separate the two contributions which would result in the twin image problem. It takes advantage of the different dependencies of $\tilde{\Phi}$ and $\tilde{\Phi}^*$ on the defocus distance D_m. Hence this method is based on multiple intensity measurements. Already by recording two images we have two linear equations for two unknowns if the non-linear term is neglected. The latter step is justified if multiple images are taken since the non-linear and the twin-image contribution tend to cancel. Assuming that we record N images at distances D_m, $m = 1...N$, the summation of equation 60 over all distances and neglecting the non-linear terms will result in a relation between $\kappa^*\tilde{\Phi}(f)$ and the intensity $\tilde{I}_m^{exp}(f)$ in the recorded images (Cloetens, 1999)

$$(61)\qquad \kappa^*\tilde{\Phi}(f) = \frac{1}{N}\sum W_m^{Par}(f)\tilde{I}_m^{exp}(f)$$

In this expression the W_m stands for the filter that has in this particular case the form

$$(62)\qquad W_m^{Par} = \frac{e^{i\pi\lambda D_m f^2} - \frac{1}{N}\sum_q e^{i2\pi\lambda D_q f^2}e^{-i\pi\lambda D_m f^2}}{1 - \left|\frac{1}{N}\sum e^{i2\pi\lambda D_m f^2}\right|^2}$$

When the denominator of the filter can be close to zero, a small constant is added in the practical implementation of formula 62. To complete the solution of the complex object, one must determine the object average κ that is the multiplicative factor in expression 61. Its modulus is determined from the average image intensity by summing equation 60 in $\mathbf{f} = 0$ over the N recorded images and finding the solution of the equation quadratic in $|\kappa|^2$. Note that the determination of the phase still requires the solution of a non-trivial phase unwrapping problem.

The situation becomes simpler considering the slowly varying phase approximation. Reconsidering equation 55 and assuming different distances, the formula for the phase is obtained by minimizing the difference between the observed and calculated intensity distributions in a least square sense. The solution may be written in a similar form as 62

$$(63)\qquad \tilde{\varphi}(f) = \frac{1}{N}\sum W_m^{Par}(f)\tilde{I}_m^{exp}(f)$$

with the filter function

$$(64)\qquad W_m^{Slph} = \frac{sin(\pi\lambda D_m f^2)}{\frac{1}{N}\sum 2sin^2(\pi\lambda D_m f^2)}$$

As for the Paraboloid method it is required to record multiple images to avoid loosing certain spatial frequencies for which the intensity spectrum is blind at a given distance.

Similar formulas for separating the absorption $B(x)$ and the phase $\varphi(x)$ are obtained in the case of the weak object approximation. They are slightly longer and can be found in (Zabler *et al.*, 2005). The expression for the phase for the homogeneous object is then just the reduction of these two equations as has been shown in (Cloetens, 1999; Turner *et al.*, 2004).

By this the overview of the contrast transfer function based direct methods is rather complete. It is left to mention the solution of the Transport of intensity equation. The general form of the retrieved phase may be written, according to (Paganin and Nugent, 1997), in the form

$$\varphi(\mathbf{x}) = -\frac{2\pi}{\lambda}\nabla^{-2}\left[\nabla \bullet \left[\frac{1}{I(\mathbf{x})}\nabla\nabla^{-2}\left\{\frac{\partial I(\mathbf{x})}{\partial z}\right\}\right]\right]. \tag{65}$$

where ∇^{-2} is the inverse Laplacian operator calculated by whatever appropriate method. In the limit of a pure phase object (imparts only a phase shift to the incident wave) illuminated by a uniform plane wave with an intensity I_0 then using $FT[\nabla^2\Phi(\mathbf{x})] = -4\pi^2 f^2\tilde{\Phi}(\mathbf{x})$ the solution for the phase is rather simple and has the form

$$\Phi(\mathbf{x}) = \frac{2\pi}{\lambda}\frac{1}{I_0}FT^{-1}\left[\frac{1}{4\pi^2 f^2}FT\left\{\frac{\partial I(\mathbf{x})}{\partial z}\right\}\right]. \tag{66}$$

Using the TIE we can find the unique solution for coherent wavefields provided that the intensity has no zeros. The homogeneous approach has been implemented into the transfer of intensity approach by (Paganin *et al.*, 2002).

If necessary the object estimation obtained from the above described direct methods can be further iteratively optimized through a non-linear least squares procedure (Kirkland, 1984; Cloetens, 1999).

2.3. A new implementation of the Gerchberg-Saxton iterative method

. Already in Fienup (1982), the iterative methods (error reduction) for phase retrieval from intensity data were compared to the gradient search methods and other iterative methods such as the input-output method. Their convergence has been demonstrated on examples for single and two intensity measurements. In the case of the KB system we typically record scans/radiographs for 3-5 different defocus distances, hence the idea is to use as much information out of them as possible without redundancy. We also have an additional input in the form of the incident wavefield at each sample plane. The Gerchberg-Saxton algorithm (see figure2) was principally meant to be used to reconstruct the phase from two intensity measurements (Gerchberg and Saxton, 1972). The convergence of this scheme was improved by Fienup who implemented the hybrid input-output approach which speeds up the convergence of the error reduction method, for which the mean square error decreases rapidly for the first few iterations but then stagnates for later iterations. Together with the oversampling (i.e. introducing a large known support in real space) this method is frequently used in the interpretation of data in coherent diffraction imaging (Robinson *et al.*, 2001). We propose a modified scheme for Fresnel diffraction and multiple intensity measurement as shown on figure 3.

Each iteration consists of the following steps (the superscript stands for the number of the iteration, the subscript for the given image plane):

(1) An initial guess of the object function T^0 is multiplied by the incident wave u_k^0 ($k = 1$ for plane 1) (the incident wave is measured at each image plane with the grid). Their product u_1^0 is propagated by P_1(in Fourier space) to image plane 1.

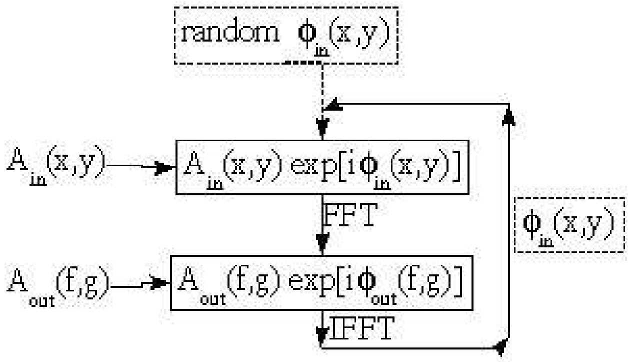

FIGURE 2. The conventional Gerchberg-Saxton algorithm for which the two intensity measurements are in the object plane and the focal plane of the imaging system.

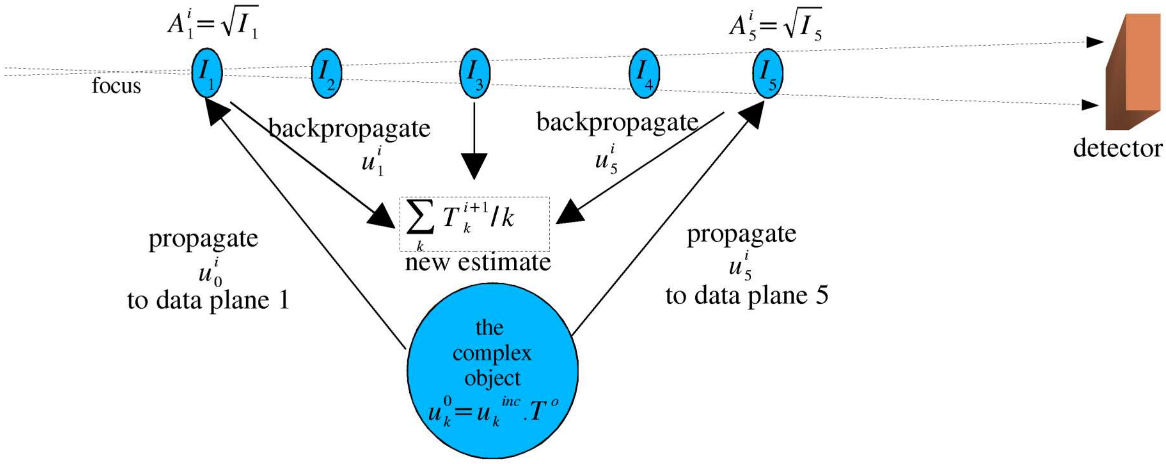

FIGURE 3. Multiple plane iterative method for Fresnel diffraction and distorted incident wavefronts

(2) At this plane we keep the new phase φ and the amplitude we substitute by $\sqrt{I_1}$, where I_1 is experimental value of the intensity in plane 1.

(3) The Fourier transform of the result is multiplied by the inverse propagator P_1^{-1} - back-propagated into the object plane and its inverse Fourier transform is divided by the wavefront function u_1^0 to obtain a new estimate of the object function T_1^i.

(4) Steps 1-3 are repeated for each image plane

(5) The new global estimate of the object function T^i is the average of the calculated object functions $T_k^i,\ k = 1, ..., N$ after the i-th iteration, N is the number of image planes

(6) A cycle of steps 1-5 is performed until the error function E^i reaches the desired value.

The proposed method shows similarities with the curved wavefront method suggested by Nugent et al. (Nugent *et al.*, 2003).

We have tested this approach on simulated one-dimensional data, where it proved to be successful, The extension to two dimensions seems therefor promising.

The direct phase retrieval methods based on the Contrast transfer function as described in this chapter will be used in the chapters on magnified tomography as a crucial step before tomographic reconstruction.

CHAPTER 3

Improving The Temporal Resolution in Tomography

1. Introduction

One possible way to look at the current trends in x-ray imaging with synchrotron radiation is to say that the development is carried out in two distinct directions which necessarily meet once in a while, but still both require a separate research. The two directions can be identified as the improvement of temporal and spatial resolution. The efforts made towards faster data acquisition will be looked upon in detail in this first part while the enhancement of spatial resolution is the subject of the second part (Chapters 5 and 6). A hot topic today in this respect is the speed of the detector and the radiation flux which is used for the imaging. Beside and between these two elements there is the third factor, namely the interface between the elements involved in the image capturing. This chapter describes the work performed with the ultimate goal to optimize the ID19 beamline in a sense that the speed of the tomographic scan is limited truly only by the combination of x-ray flux and detector efficiency and speed. It involves the following three main tasks:

- Rather than sequentially, to perform as much as possible in parallel the different events in the tomographic acquisition chain
- to opt for the adequate acquisition procedure ("step by step" or continuous) and optimize the remaining parameters such as the exposure time, number of projections etc.
- to compare on experimental data the performance of the three CCD detectors available at the ESRF (the inhouse developped FreLoN 2000 and 2k14 series and the commercially available DALSA camera)

2. The beamline dispositive for performing tomography

The tomographic setup of ID19 for parallel beam acquisition with a rough scheme of the involved elements and their communication is depicted in figure 1(a) while the sample stage composition is discussed in more detail is in 1(b). Note that this is the initial status before introducing a dedicated solution consisting of a new device server (a piece of software responsible for one or multiple devices such a motors or detectors) which will be described in the next section. The motors of the sample stage that are active during a tomographic scan are two continuous motors (as pointed out in figure 1(b)) from NEWPORT driven by a PM500 controller. The communication between the controller and the outside world goes over a GPIB interface. GPIB commands can be sent directly in the beamline control software SPEC (www.certif.com) using the TACO[1] interface. During the scan the rotation stage PMO ensures the rotation of the sample typically over $180°$. The PMY is a translation in the direction perpendicular to the beam and serves during the scan for acquiring reference images without sample. The third crucial instrument that has to be considered in this study is the x-ray detector, in our case the CCD based detector. The latter triggers through a TTL signal the opening and closing of the x-ray shutter. The flow of the usual tomographic scan can also be followed on the diagram in figure 2. SPEC transmits the command to the PM500 controller to move the motor to a given position and waits till the new position is reached. Then a SPEC command is sent to the counter card that triggers the exposure of the camera. A typically $8 - 30$ ms interval is reserved before and after camera exposure for the movement of the shutter. When the exposure is finished the pixels of the CCD are read out (vertical transfer of pixel values) and transferred to the PC and saved. When this transfer is completed the camera device server sends a signal to SPEC which can successfully terminate the polling that was going on while waiting for the above events to finish. The whole process is repeated starting by moving the motor to the next position.

The drawback of this scheme is that there is no possibility of independent acquisition and mainly that all happens sequentially which is the slowest possible situation. Certain optimizations were already completed before introducing the new 'fasttomo' device server. These included to save image $n-1$ during the exposure of image n and to start to move the motor already during the readout of the CCD. Nevertheless these still do represent the sequential approach because even though in a usual sense of the word they occur in a parallel way, but synchronization is mainly only software based, and the commands for each action occur in a sequence.

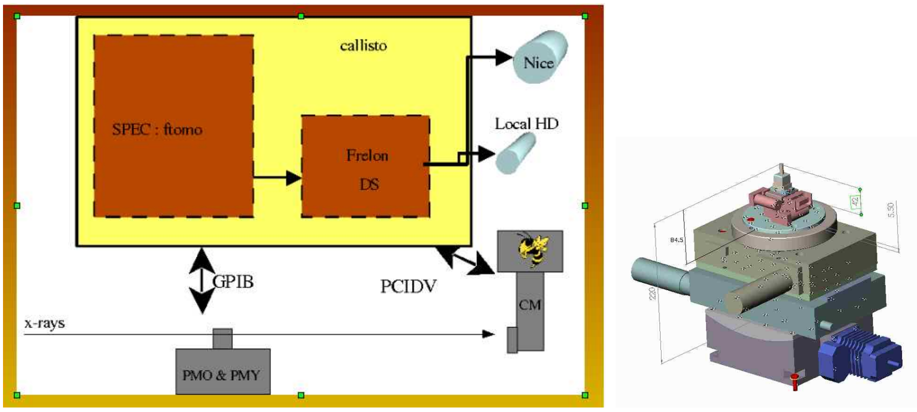

(a) (b)

FIGURE 1. In (a) is the sample stage the detector and their peripherals. (b) the sample stage description is from top to bottom as follows: ± 2.5 mm X and Y translations for sample alignment, PMO - the high precision continuous rotation stage PMY - ± 75 mm Y translation for rotation axis positioning and reference image acquisition.

---

[1] TACO is an object oriented control system where every control element is treated as an object on which commands can be executed. The objects are called devices created and stored in device servers. The commands which can be executed on a device are implemented in the device class.

3. The effective way of communication

To perform the individual tasks of the scanning process in parallel first the four following steps are merged to occur at the same instant: The (i) readout of the image, (ii) transfer of image $n-1$ to the PC, (iii) saving a precedent image (may be behind the scan thanks to the buffer) would form a parallel process with the (iv) motor movement. In special modes of the CCD the readout of image $n-1$ can in addition occur approximately at the same moment as the exposure of image n. Finally for short exposure times a scanning mode will be introduced where the exposure occurs parallel with the motor movement. These are the main ideas behind the optimization action undertaken as a part of this project.

Reducing the exposure time is important since it has to be multiplied for each scan by a large number of views corresponding to the angular sampling. This logic equally applies to the time lost in the communication between the rotation stage, the SPEC interface and the counter card that triggers the camera. Some modifications to enhance the speed of the acquisition chain have already been mentioned above, as well as their 'software-synchronized' nature which in consequence introduces unavoidable dead times corresponding mainly to the polling of SPEC between the end of an event and the start of the next one. The analysis of the TTL signals during tomography revealed an approximately10 ms polling time (t_b and t_e in the diagram on figure 2) in the beginning and at the end of each image capture procedure that consists of exposing the CCD and reading it out afterwards. Similar overheads are associated to verifying the status of the camera, image saving etc.

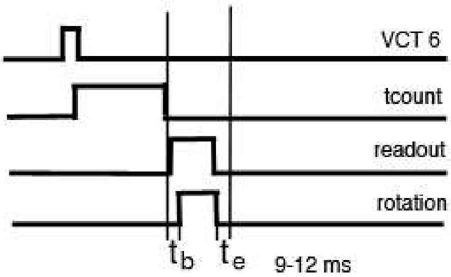

FIGURE 2. The time delays t_b and t_e in a representation of TTL signals in the chain of image acquisition during tomography. The delays add to the total scan time and therefore should be avoided by employing rather hardware synchronization and parallelization as possible with the Fasttomo device server.

One explanation is that SPEC communicates with the rotation stage leaving the mentioned 10 ms for verifying the status of the rotation. The solution for suppressing the dead times and doing as much as possible in parallel is based on distributing the tasks to "intelligent" units (camera, rotation stage, shutter) that are synchronized as far as possible by (fast) hardware signals. Also one will *acquire a series of N angles rather than performing N times the same acquisition*. In practice this is realized by device servers and the control software SPEC essentially configures the device servers but does not interfere during the fast scan itself. A first device server is associated to the camera and is developed by the software group BLISS from the ESRF. The second one, the *Fasttomo device server (FastDS)* is associated with the rotation and translation stages and was written by C. Medrano and I. Plaza from Zaragoza University. The work I present here includes the design of the device server which is adapted to the needs of the beamline and its refinement by testing during the development, as well as the final commissioning before it has been fully implemented. This iterative process resulted in a software package that by now has overtaken the well defined part of SPEC responsibilities during all tomographic experiments.

The *Fasttomo device server (FastDS)* is a C program using TACO libraries. It accesses GPIB devices via the C library from National Instruments and controls thus the two active motors during the scan, the rotation and translation of the sample. (SPEC then only distributes the parameters to the FastDS.) The new configuration of the scanning setup is in figure 3 (compare to the scheme in figure 1). The Fasttomo device server also talks to the VCT6 counter card through the device server of the VCT6. Therefore this timer/counter card allows the efficient synchronization of the events. It triggers the CCD exposure time but also detects when the camera is ready to acquire a new image. Two counters of the VCT6 card are used. The FastDS transmits to the first counter the value for the exposure time (t_{exp}). Together with this counter the second, auxiliar one is started as well. The latter stays 'high' until the short End Of Read (EOR) pulse from the camera arrives. This is fed to the stop input of the second counter and puts it to 'low' indicating to the FastDS that the camera has finished reading out the CCD and the next image can be acquired.

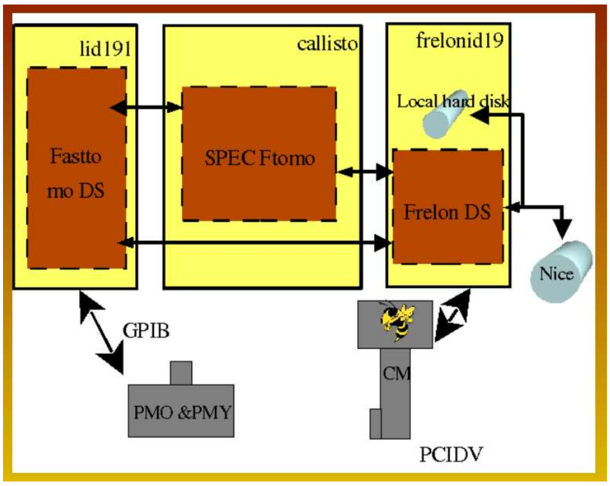

FIGURE 3. The communication channels with the FastDS. Note that the sample stage and the camera communicate with their own device servers and the control software SPEC only controls the initial and the final state and does not interfere during the scan.

The three principal types of scaning implemented in the FastDS together with the original sequential scan can be seen on a sequence diagram in figure 4:

- **regular (step by step) scan:** Set by command (DevFastTomo *FastDS <argin>, DevVoid*). This mode branches into two submodes depending on the input argument.

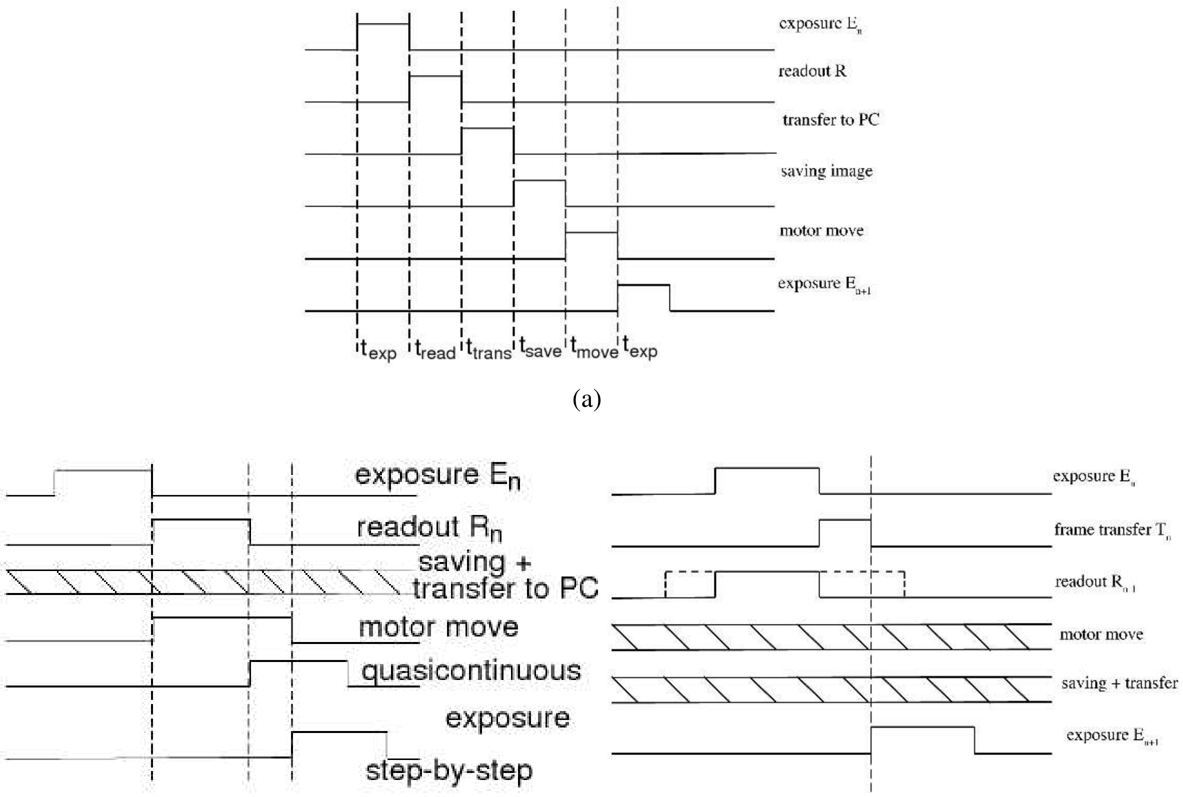

(a)

(b) (c)

FIGURE 4. The TTL sequence diagram of the original completely sequential scanning mode (a), the step by step mode of the Fasttomo device server (b) as well as the continuous scan mode with frame transfer to the buffer (c).

If *argin*=7 (111 in binary), the acquisition is as follows: exposes the CCD and waits till end of exposure, then moves the motor to a new position waiting to complete this movement, waits for for the shutter (shutter closing time set by DevSetParam) and finally for the EOR signal from the camera. If *argin* is set to 6, the sequence is similar with a modification such that the scan doesn't wait for the motor to finish its movement, hence it can be regarded as a **quasicontinuous** scan when the FastDS sends through the GPIB the position of the next angle while the PMO can still be in movement. In both cases the rotation stage receives the command to move immediately after the camera has started the readout. This way, processes (i)-(iv) as listed above all occur in a parallel manner. There is an option to chose not to wait for the EOR signal from the camera, but that can be dangerous because of the mixing up of images.

- **timescan:** (DevTimeScan <*FastDS*> <*argin*>, *DevVarDoubleArray*) takes images without moving the motor as follows: exposes the CCD, waits end of exposure, waits shutter and waits EOR. Respects the settings of the scan in the sense of the shutter closing time and waiting or not for the EOR signal.
- **continuous scan:** (DevContScan <*FastDS*> <*argin*>, *DevVarDoubleArray*) moves the motor at constant speed v and takes images at regular intervals the same way as in

> timescan. The speed is calculated as a function of the camera readout by performing DevCalibration. The user may also provide the value of the CCD readout time in *argin*. If provided, it will then be used for the speed determination. Given the readout time, for a known initial and final position of the rotation stage and a given number of projections the speed can be calculated as $v = \frac{\theta_{end} - \theta_{init}}{N*(t_{exp} + t_{readout})}$. The rotation stage is set into movement at an initial position $\theta_{init} - \Delta)$, where the parameterΔ is the angle decrement before the rotation stage accelerates from zero to v. It is determined from the previously calculated speed v and acceleration (this is set by the user) of the rotation stage . A constant speed v is thus assured when the PMO crosses the zero angle θ_{init} at which point image acquisition starts. We performed measurements of the initial and final angle of tomographic scans as a function of the imposed speed. We found that the value of the speed calculated by the above expression does not meet the requirement $\theta_{final} - \theta_{init} = \pi$. Therefore we corrected empirically the value of v and hard coded in the program. The empirically determined speed decrement was positive meaning that in reality the uncorrected value of the speed is higher than the actual speed of the PMO. A more accurate synchronization could be obtained with an accessible encoder signal. The present solution is still satisfactory as the behavior of the rotation stage turned out to be reproducible.

Using the FreLoN 2k14 camera, the DALSA camera and a solid foam sample (lava from the Reunion island) the various scan modes have been tested in order to observe their influence on image quality, but also to fine tune the parameters of the FastDS. The optics used in the tests has a Gadox scintilator and gives a pixel size of 7.46 μm. This optics is identical to the one used in the experiment on liquid foams which is presented in Chapter 4. Table 1 presents three independent measurements of image quality for the three scanning modes and for all the three

scan mode	proj. x t_{exp}	SNR	σ_r	σ_t	remarks
step by step	500x0.05 s	11.58	3.2	3.66	DALSA
quasicontinuous	500x0.05 s	10.2	3.31	3.35	DALSA
step by step	300x0.01 s	10.1	4.1	-4.5	DALSA, binning
quasicontinuous	300x0.01 s	8.8	5.2	-4.5	DALSA, binning
continuous	300x0.01 s	12.1	5	-4.8	DALSA, binning
quasicont.	900x0.35 s	19.2	2.9	2.9	FReLoN, FFM
continuous	900x0.35 s	19	2.9	2.9	FReLoN, FFM
quasicont.	500x0.1	14.6	3.37	3.12	FReLoN, FTM, 16 bunch
continuous	500x0.1	17.9*	3.27	3.7	FReLoN, FTM, 16 bunch

TABLE 1. Measurement of image quality in 'step by step' (before each exposure the position of the rotation stage verified), 'quasicontinuous' and 'continuous' scanning mode. Unless noted by "16 bunch" the beam delivery was in uniform mode. The significantly higher value marked with * may be explained also as due to the fact that the electron beam current was 77 mA compared to 67 mA for the previous raw.

cameras. The SNR was calculated using the formula

$$SNR = \frac{\langle I_2 \rangle - \langle I_1 \rangle}{\sqrt{\sigma_1^2 + \sigma_2^2}} \tag{67}$$

with $\langle I_1 \rangle$, $\langle I_2 \rangle$ being the average pixel value in regions 1 and 2 as defined on figure 5 and σ_1, σ_2 the corresponding standard deviation of the pixel value. To estimate the resolution for the scans, two perpendicular edges of a feature in the slice are selected. The final tangential and radial resolution, σ_t and σ_r are the mean of five edge profile measurements. The choice is based on the expectation that if the continuous mode of scanning affects the spatial resolution, its influence will be more severe on the tangential resolution. The values for the DALSA camera measurements are simply the average maxima or minima of the derivatives of the edge profiles as illustrated in figure 5(b). For the FReLoN camera the spatial resolution in the scans is determined with the aid of a complementary error function (erfc) fitting five selected edges and evaluating the mean of the fit. The $erfc$-function is defined in the usual way as $erfc(x) = 1 - erf(x) = \frac{2}{\sqrt{\pi}} \int_x^{\infty} e^{-t^2} dt$ and its analytical derivative gives the resolution in units of pixels. From the point of view of comparing the influence of scan method on image quality, this inconsistency due to different processing has little or no effect.

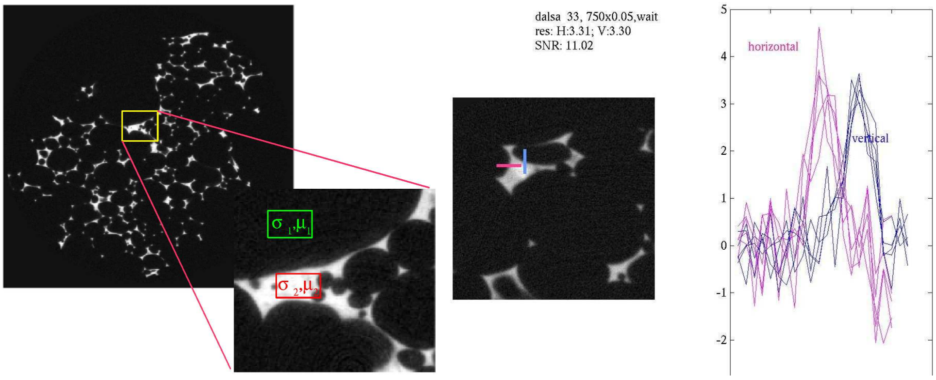

(a) (b)

FIGURE 5. The graphical definition of figures of merits for image quality determination. (a) shows a scan with the FreLoN 2048 camera at 750 views and 0.05 s exposure time. The region with signal and another with background is selected to measure the SNR in the scans. For the resolution estimation in the case of the DALSA camera, the absolute values of the derivatives of five edge profiles are plotted (b). After averaging them their maxima gives an estimate of the resolution spatial resolution.

The analysis shows that for short exposure times (<0.5s) the fact of not waiting for the rotation stage at each exposure does not reduce the image quality, but may even enhanced it. This has been observed with a solid sample and is even more true for liquid samples that can be affected by the acceleration of the sample stage movements.

4. The detector race: DALSA vs. FRELON

Two cameras have been tested with the newly installed FastDS. (A third camera - the older version FreLoN has been also compared for the scans with higher number of projections and longer exposure time and no significant difference in image quality has been found as compared to the new FreLoN 2k14, therefore in the following we only compare the new FReLoN to the DALSA) The aim of this comparison is to select the best setup for imaging fast evolving systems. Some selected technical specifications of the DALSA and FreLoN cameras are listed in table 2. The DALSA image array is in reality 1024×2048 pixels divided into two identical arrays of 1024×1024 (figure 6a). The light-sensitive photodiode register collects incoming photons projected onto the CCD surface by the lenses. After image data has been collected

characteristics	FreLoN 2K14	DALSA
sensor type	ATMEL TH7899M	ATMEL THX7887A
number of pixels	2048x2048	1024x1024
pixel size	14x14 μm	14x14μm
dark current	1 e/pixel/s @ 253 K	452 e/pixel/s @ 298 K
A/D converter	14 bit @ 4 x 10 Mhz	12 bit @ 4 x20 Mhz
gain	20 e/ADU	50 e/ADU
saturation	16383	4095
full well capacity	320 000 e	204 750 e
readout noise	1.3 ADU	0.96 ADU
QE	0.24	0.1
readout mode	FTM, FFM	FTM
speed in FFM	8/15(binning 2x2) fps	
speed in FTM	15/27(binning 2x2) fps	60 fps

TABLE 2. Technical data for the FReLoN and DALSA cameras. FTM stands for frame transfer mode, FFM for full frame mode.

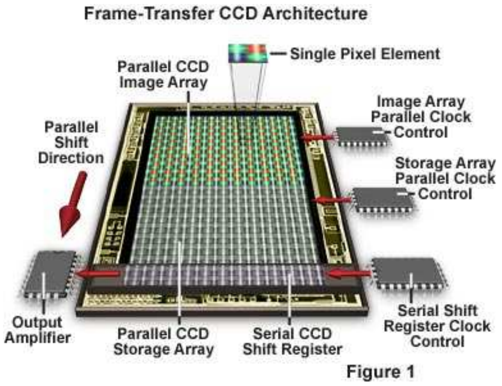

FIGURE 6. The principle of the detector operation in frame transfer mode. The design is that of the DALSA camera. The charge from the green colored - active array is, after each exposure, transferred to the gray - storage array from where it can be read out while the green array is newly exposed. In the case of frame transfer mode operation of the FReLoN 2k14 the storage array is defined as two 512×2048 ribs on the two sides of the active CCD array.

and converted into electrical potential by the image array, the data is then quickly shifted in a parallel transfer to the storage array for readout by the serial shift register. Transfer time from the image-integrating array to the shielded storage array is dependent upon the pixel array sizes, in the case of the DALSA camera here tested, it was $t_{trans} = 2.8$ ms and for the FReLoN $t_{trans} = 6$ ms. The storage array of the DALSA is not light sensitive like it is in most frame-transfer CCD designs. The default mode of operation of the FReloN 2k14 camera is FFM, i.e. readout occurs in sequence after the exposure and the whole 2048×2048 CCD is read out. Nevertheless the FTM was recently implemented putting this camera back into competition for fast imaging. Detectors based on CCD arrays not equiped with integral shielding like for the DALSA camera, are capable of being operated in either *full-frame mode (FFM)* or *frame-transfer modes (FTM)*. With the use of a mechanical shutter, a frame-transfer CCD can be used to quickly capture two images in sequence. During the period in which the parallel storage array is being read, the image array is busy integrating charge for the next image frame. A major advantage of this architecture is the ability of the frame-transfer device to operate without a shutter or synchronized strobe, allowing for an increase in device speed and faster frame rates. As can be seen in figure 4(c), between to consecutive exposures the time delay is purely the time for the frame transfer instead of the whole readout time which is generally $1 - 2$ orders of magnitude longer. Frame-transfer CCDs suffer from several drawbacks including image "smear" (see figure 7), which occurs because integration and dump to the storage array happen simultaneously. Smear artifacts are limited to the time necessary for transfer of image integration data to the storage array.

Figure 7 illustrates the smearing effect due to the absence of shutter in frame transfer mode. During one exposure - frame transfer - readout cycle each pixel receives a contribution of the whole image in the corresponding column to give the ultimate intensity at each pixel $I_n^{FTM} = I_n + \alpha \langle I_n \rangle$ with $\alpha = t_{transfer}/t_{exposure}$ being the smearing parameter. One could think about reducing the effect by introducing a very fast shutter or post-processing the scans using the formula with the smearing parameter. In the meantime the beamline possesses a fast shutter with 8×8 mm^2 field of view and 9 ms of shutter closing time that goes up to 30 ms for a 15×15 mm^2 shutter. There is no x-ray shutter available covering the field of view usually of order of 1 cm and being fast enough to still benefit from the FTM. On the other hand, as shown in figure 7, smearing only affects the first image of the scan, because we start the acquisition from an empty CCD. Therefore its contribution to the entire scan is small enough to neglect as verified by measuring the signal to noise ratio and the tangential and radial resolution (σ_t and σ_r) in the reconstruction of one projection (see figure 7 or table 3). On the SNR the more important influence has the change of 10 ms in exposure time as can be seen from the first row in table 3.

A rather general conclusion would be that the DALSA is faster compared to the FReLoN, but has certain drawbacks including the rather delicate setup on the beamline. The smaller dynamic range of the DALSA would generally not effect the data quality in the fast regime, but the crucial term is the higher quantum efficiency of the FreLoN detector. The detector quantum

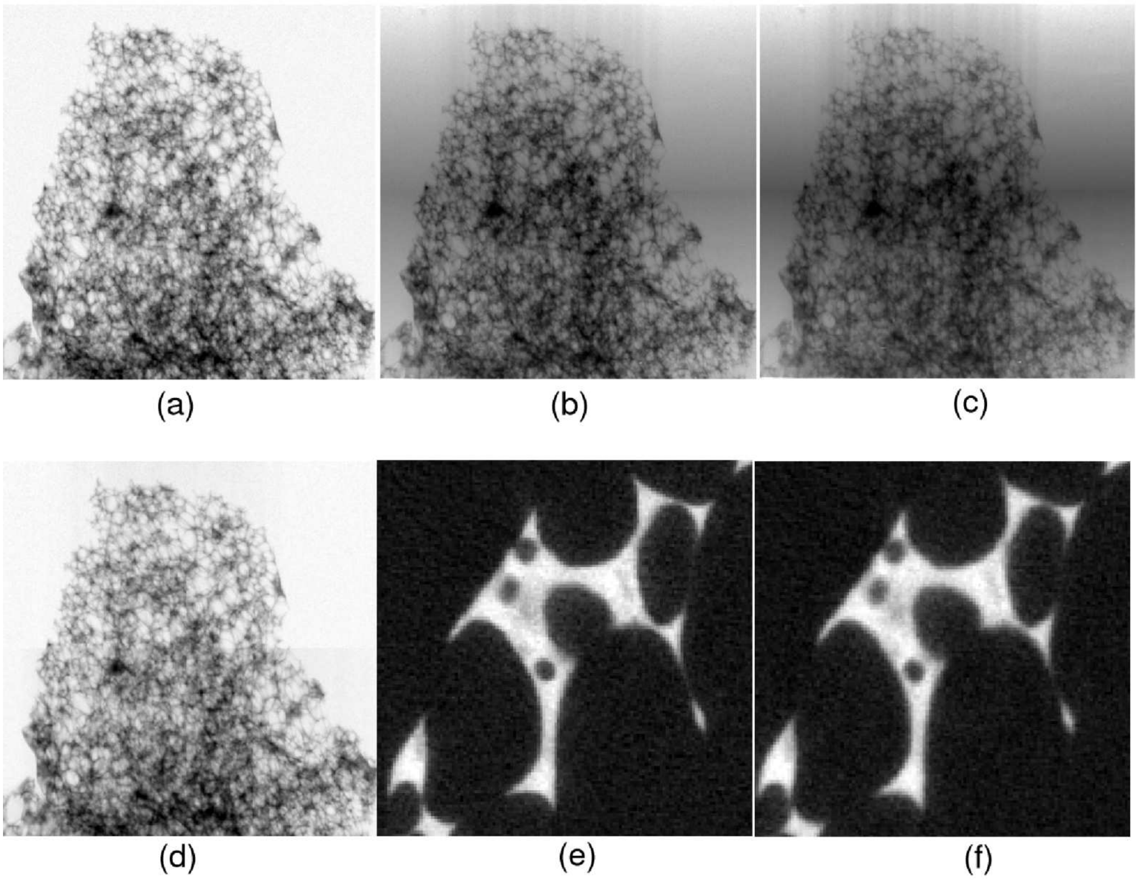

FIGURE 7. smearing of the image when in FTM mode. The first projections of the scans in FFM with $t_{exp} = 0.05$ s (a), FTM with $t_{exp} = 0.06$ s (b) and the first and second projection in FTM with $t_{exp} = 0.032$ s (c) and (d)(this is the limit for the FReLoN camera in binning). (e) and (f) are zoomed areas of the tomographic slices corresponding to (a) and (b) respectively. The influence of the frame transfer starts to be important only for very short exposure times.

camera & beam mode	N_{tomo} x t_{exp}	SNR	σ_r	σ_t	scan mode
FFM, uniform	500x**0.05** s	15.3	3.2	2.8	continuous.
FTM, uniform	500x**0.06** s	16.4	2.85	3.2	continuous
FFM, 16 bunch	500x0.1 s	16.47	3.55	2.8	quasicont.
FTM, 16 bunch	500x0.1 s	14.64	3.37	3.12	quasicont.
FFM, 16 bunch	500x0.25 s	23.72	3.42	3.53	continuous
FTM, 16 bunch	500x0.25 s	24.3	3.55	3.5	continuous

TABLE 3. Data to compare the FTM and FFM mode for the FReLoN 2k14 camera. All images are 1024×1024 pixels. The eventual influence of the camera operation mode is probably below the precision of the determination of the listed quantifiers.

efficiency is given by

$$DQE = \frac{SNR_{out}^2}{SNR_{in}^2} \tag{68}$$

For an ideal detector the SNR at the output has the same value as at the input. The ratio of DQE for the two cameras $DQE_{FreLoN}/DQE_{DALSA} \approx 2.4$ (see table 2). When combining this value with the gain ratio of ≈ 2.7 the resulting ratio of the gain in number of ADU's approaches 5 in favor of the FReLoN. To quantitatively compare the two cameras, scans taken at exactly the same conditions with both the DALSA and the FReLoN 2k14 indicate the strength of the latter. For a slice reconstructed from 750 projections at $t_{exp} = 0.05$ s exposure time with the FReLoN 2k14 and the same with the DALSA (the tomographic slice of this scan is in figure 5) results in a $\Delta SNR \approx 3.4$ in favor of the FReLoN 2k14. This number even increases with longer exposure times, so that for the double $t_{exp} = 0.1$ s we have $\Delta SNR \approx 7.6$. For many applications the field of view is an important consideration. It is definitely true in the case of imaging of foams where the statistics plays an important role. The DALSA offers a CCD area of 1024×1024 pixels while in FTM the FReLoN active pixel area is 2048×1024. It is therefore prefered to use the FReLoN camera for the foams.

5. Determination of the impact of speed enhancing factors on image quality

Next we shall address some other parameters of a tomographic scan like the exposure time and the number of views. They constitute an important part of the optimization process. The effect of the number of views on the scan quality is presented in table 4, and graph 10(a). The number of views N_{tomo} required for the optimal reconstruction of a tomographic scan is related to the number of pixels N_{pix} in the direction perpendicular to the rotation axis as

$$N_{tomo} = \frac{\pi}{2} N_{pix} \tag{69}$$

As a rough estimate it is usually taken that $N_{tomo} \simeq N_{pix}$, but when we follow in table 4 the decrease in scan quality, we can estimate that at $N_{tomo} \simeq N_{pix}/4$ the image quality is still usable. Figure 8 demonstrates the decrease in resolution as a function of distance from the center of rotation in accordance with the theory given in section 1.5. Far from the rotation axis, the coarse information in the high spatial frequencies causes the noise to increase as can be seen in figure 8 and rigorously followed on the graphs in figure 9(a) and (b).

Another important factor in the optimization process is the influence of the exposure time on the scan quality. This is in big extend determined by the scintillator efficiency and the photon flux of the source. In frame transfer mode the absolute low limit of the exposure time is set by the detector readout time. For the FReLoN 2k14 in FTM this value is $64\,ms$ for the readout of a 2048×1024 image array, and $32\,ms$ in binning mode. The measurements are summarized in table 5.

Figure 11 shows the tomographic slice of the fastest scan acquired with the introduced new setup. The 300 projections taken with the DALSA camera in binning mode in approximately 3 seconds give a scan with reasonably good quality.

Using all the above tests one can select the parameters best matching the needs for a particular application. This study had to precede the experiments described in the next chapter. It has been understood from the collected data that the number of views is not a crucial factor until a

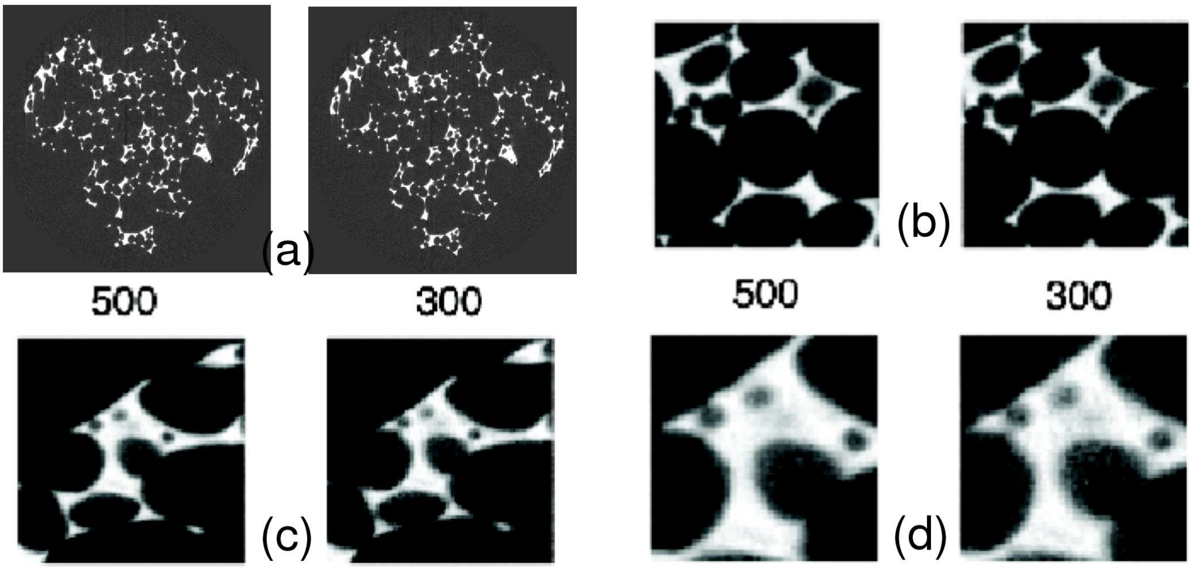

FIGURE 8. The effect of reduced number of projections, N_{tomo} can be best viewed if two regions are selected in a pair of tomographic slices acquired with two different N_{tomo} (a). The number of projections is given in the figure for each column, respectively 500 and 300. The other parameters of the scan are identical for the two images (FReLoN 2k14 in FTM continuous mode with exposure time of 0.06 s, field of view 1024 pixels). A zoom of a region near the rotation axis is in the image pair (b). No difference between the two images is visible in this case. The second pair of images (c) is a zoom of a feature at the periphery of the tomogram. (d) is the same feature at higher magnification. The corresponding data is in figure 9 and also in rows 3 and 4 of table 4.

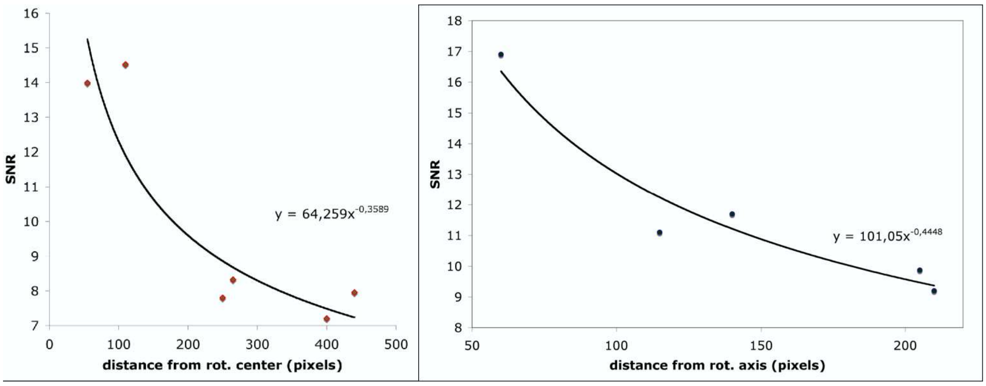

(a) (b)

FIGURE 9. Plots of the SNR as function of the position (in pixels) from the center of rotation of the reconstructed slice. (a) corresponds to an image with $N_{tomo} = 300$ and $t_{exp} = 0.06$ s, (b) to $N_{tomo} = 300$,$t_{exp} = 0.032$ s both in FTM and the latter in binning.

low limit is reached around $N_{pix}/4$. The further decrease of N_{tomo} below this value, has more severe effect on the scan quality than the exposure time. We see from graph 10(b) that if the exposure time decreases by a factor of 5, the SNR only reduced by approximately 35 %

ring fill mode	N_{tomo} x t_{exp}	SNR	σ_c	σ_t	scanning time
uniform	1500(100)x0.35 s	19	2.92	2.8	15x52 s
uniform	900(100)x0.35 s	19.2	2.9	2.9	9x52 s
uniform	500x0.06 s	16.4	2.7	3.2	34 s
uniform	300x0.06 s	13	2.3	3.2	21 s
uniform	300x0.032 s	13.4*	2*	2.4*	11.7 s
uniform	200x0.032 s	10.5*	1.7*	2.7*	8 s
16 bunch	700x0.06 s	13.7	3.7	3.2	47 s
16bunch	500x0.06 s	14.1	3.2	3.7	34 s
16 bunch	300x0.06 s	7.9	4	3.6	21 s

TABLE 4. Scans taken with various number of projections to estimate the impact on the image quality. All scans are with a field of view of 1024×1024 pixels. The Fasttomo device server for all scans apart the first two was in continuous mode and the camera in FTM. The first two values are for quasicontinuous and FFM mode. The number in brackets behind the N_{tomo} means that reference images are taken after each 100 projections. Otherwise 20 reference images are taken before and after the scan only. The * marked values are for binning mode of the camera. The shortest scan is 8 s for 200 projections. Its reconstruction gives still images of reasonable quality.

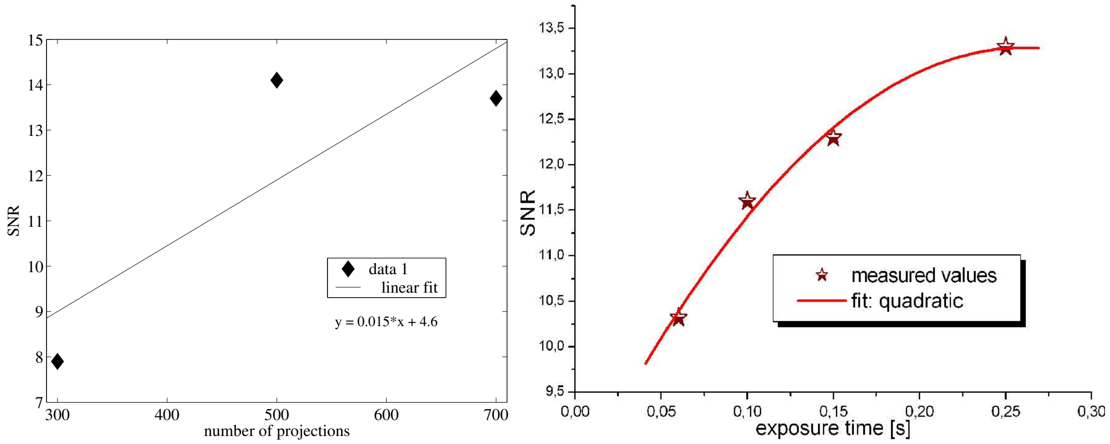

(a) (b)

FIGURE 10. Graphical representation of dependencies of the scan quality on the number of views (a) and the exposure time (b).

Finally the ultimate conclusion on the optimization process for fast data acquisition is that it is desired to keep the exposure time at its minimum (64 ms) and adjusting the number of views to the number of pixels, not going much below $N_{pix}/4$. All under the general frame of the camera in FTM mode, continuous scanning type and no shutter. To allow high data collection efficiency at this speed the choice is the FreLoN 2k14 series camera. Such a configuration allows to access the dynamical properties of three-dimensional liquid foams by x-ray tomographic imaging.

ring fill mode @ e^- current, scan mode	N_{tomo} x t_{exp}	SNR	σ_c	σ_t	scanning time
uniform, FFM,	500x0.1	17.3	3	3.02	2 min 12 s
uniform, FFM	500x0.05	15.3	3.2	2.8	1 min 48 s
uniform, FTM, bin	300x0.1	13.2	1.27	1.47	32 s
uniform, FTM, bin	300x0.06	14.1	2.1	2.22	21 s
uniform, FTM, bin	300x0.032	13.4	2.1	2.4	11.7 s
16 bunch @ 73, FFM, step	500(100)x0.26	19.2	3.6	2.9	
16 bunch @ 74, FFM, step	500(100)x0.1	16.6	3.6	2.7	
16 bunch @ 72, FFM, step	500x0.26	18.9	3.6	2.8	
16 bunch @ 72, FFM, step	500x0.1	16.5	3.6	2.8	
16 bunch @ 79 , FTM,	500x0.25	23.7	3.5	3.5	
16 bunch @ 63, FTM,	500x0.15	16.9	3.8	3.5	
16 bunch @ 77, FTM,	500x0.1	20.1	3.3	3.7	
16 bunch @ 66, FTM,	500x0.06	11.5	3.3	3.7	

TABLE 5. Scans to compare the effect of exposure time. The image size is 1024×1024 pixels. Unless the "step" comment is added, the scans are acquired in continuous mode. The "step" comment stands for the quasicontinuous mode. The storage ring electron current in mA is added in the setup description in the first column, as it has an important influence on the quantifiers especially in 16 bunch mode where the relative current change is bigger than in uniform storage ring fill mode.

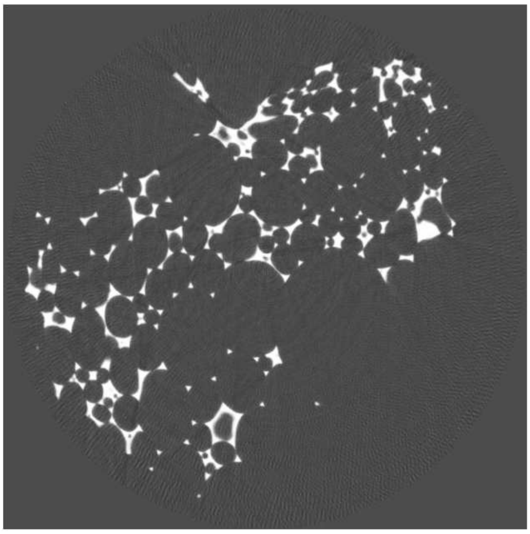

FIGURE 11. The fastest tomographic scan with reasonable quality obtained with the new acquisition scheme in continuous and parallel mode. The image shown is obtained with the DALSA camera in binning mode (515x512 pixels field of view) with 10 ms exposure time. The actual scanning time (without reference images) is 3 s.

CHAPTER 4

An application requiring fast data acquisition: liquid foams

1. The physics of cellular patterns

1.1. Introduction to foams and their application

. If one would like to build a network of roads connecting two and more towns provided that there aren't any obstacles like important geological and hydrological features, then the optimal solution in terms of the lengths of the roads can be found for instance by dipping into a washing-up liquid diluted in water a 2D pattern modeling the layout of the towns (imagine two plexiglass plates separated by a 1-2 cm gap, connected only by rods that would represent the towns). When pulling the maquette out, between the points there will be a network of soap films formed meeting the condition for shortest distance network. At first sight this experiment might have not much to do with foams except of the liquid used, but then each film can be regarded as belonging to two neighboring bubbles in a dry foam. Although this isn't the usual way of projecting transportation channels in a country, therefore not the best example to demonstrate the usefulness of foams, this example reveals one of the basic physical properties of foams, which would account for certain statical and dynamical processes studied in the later chapters. We can point out then already at this place that each bubble in a foam will take such a form as to minimize it's surface and energy with respect to it's neighbors.

Scientists know a great deal about the individual bubbles in foams and how they "talk" to one another through simple friction. But when many bubbles clump together to form a foam, the resulting material exhibits a host of unexpected properties and behaviors. Liquid foams, for instance, are composed of roughly 95 percent gas and 5 percent liquid, yet they tend to be far more rigid than their components. This is due to a phenomenon called jamming. Because the bubbles are so tightly packed, when a foam is pressed down, the bubbles can't hop around one another. The more the bubbles are jammed together, the greater the pressure inside them grows and, consequently, the more they take on the characteristics of a solid.

The biggest challenge facing scientists is to create predictive models of foam rheology, or just simply coarsening that is, the way it flows or evolves over time. As foams age, gravity drains their liquid downward, and smaller bubbles are absorbed by larger ones, a process called coarsening. But until quite recently our understanding of this process has been limited to 2D foams by the inherent difficulties of studying such an ephemeral material in three dimensions.

It is this wide range of unique mechanical properties- from elastic solid to viscous fluid- that makes foams so useful for everyday applications. Most recently, a new anti-terrorism foam was used to decontaminate congressional office buildings and mail rooms in Washington, D.C. Developed at Sandia National Laboratories, the foam neutralizes toxic chemical and biological agents such as anthrax and sarin nerve gas within minutes. The foam, sprayed from handheld canisters, expands to about 100 times its liquid volume as air is drawn into the spray. It fills crevices and other elusive hiding places, then collapses back to its compact liquid state a few hours later. This behavior is widely used as part of chemical factories security systems. As practical as foams can be, their true appeal to physicists lies in their unique behavior. Ultimately, foam research may help explain the structure of plant cells and the way in which biological systems emerge and evolve - subjects as complex as foam itself.

1.2. Static properties of foams

. Several terms were already mentioned which require definition. First the foam itself from the chemical point of view is in the simplest case a *liquid with a surfactant* (foaming agent). When the foam is formed and if it is a closed foam then the surfaces between individual bubbles are called films. Their thickness in liquid foams can vary from nanometers up to a few micrometers and their curvature will be a consequence of the pressure in individual bubbles, the geometrical configuration of the system and eventually other parameters like shear and stress but those are out of the scope of this short introduction. Places where 3 bubbles meet are referred to as Plateau borders. The name comes after Plateau who's three equilibrium laws represent the fundamental rules for any foam. His formulations are as follows (see also figure 1):

1. Three films meet at each edge forming an angle of 120° .
2. In 3D four Plateau borders meet at each node and the angles are all equal 109.5°.
3. The transition between Plateau border and an adjacent film is smooth.

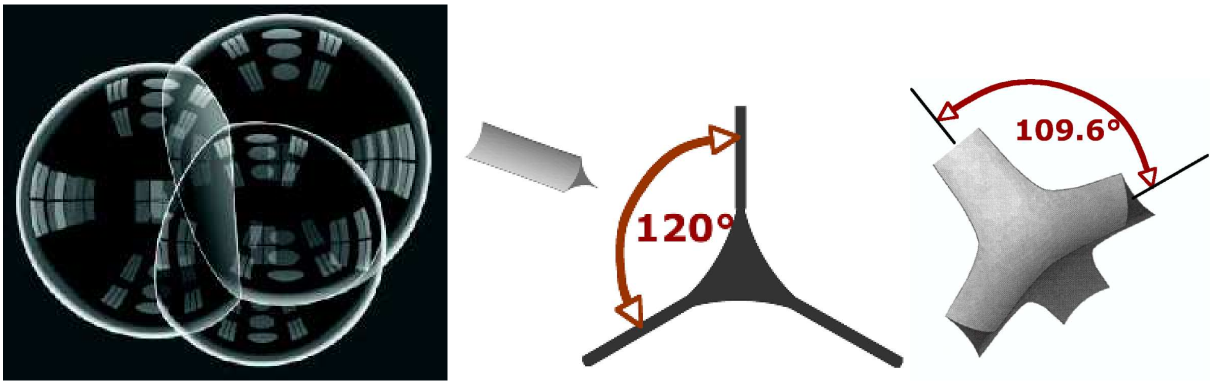

(a) (b) (c)

FIGURE 1. This triple (a) bubble exhibits the Plateau singularities: smooth surfaces (films) meet along in triple-junction curves at 120° angles - Plateau borders (b), and these junctions come together at tetrahedral points - nodes (c).

We will refer to these rules later when a brief description of processes leading to the equilibrium in foams will be given.

Taylor showed, using geometric measure theory, that Plateau's rules are a consequence of the fact that soap films are minimal surfaces (Taylor, 1976). The minimal surface in 3D is one that has a mean curvature

$$H = \frac{1}{2}\left(\frac{1}{R_1} + \frac{1}{R_2}\right) \tag{70}$$

equal to zero. The radii R_1 and R_2 are defined in figure 2. The Gaussian curvature is then introduced as $K = \frac{1}{R_1 R_2}$.

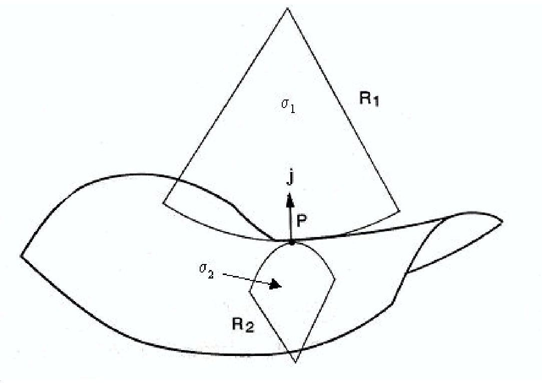

FIGURE 2. For a soap film in three dimensions two principal radii of curvature, R_1 and R_2 may be defined locally for each small element of the soap film.

Having defined some basic topological quantities we can now describe the formation of the foam. For this we have to go to a lower scale as illustrated in figure 3

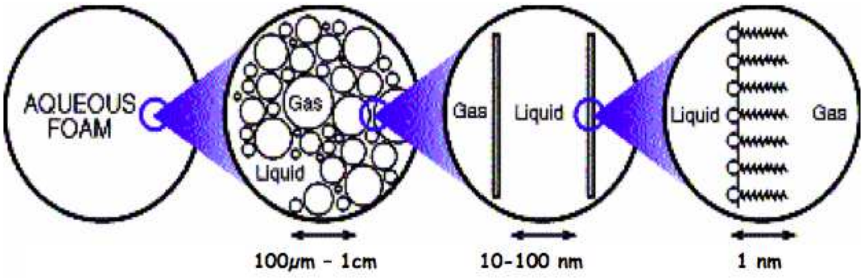

FIGURE 3. The range of length-scales at which foams are studied. At each length-scale a different aspect of the foam is studied; for example at the nanometric level the foam formation may be studied.

The surfactant is a substance composed of surface active molecules that spontaneously adsorb and decrease the surface tension of the solution. The composition can be schematically described as consisting of molecules with hydrophilic head and hydrophobic tail ensuring this way the typical organization at the water-air surface as highlighted on figure 4. Films between indiviadual bubbles are created this way and the foam is formed. The surfactant affects all properties of foams and can be used to control foam behavior. The classification of foaming agents is rather extensive, but can be summarized into three main categories: (i) solid particles, (ii) polymeric and (iii) surfactants with low molecular mass that are further divided into (a) ionic and (b) non-ionic. One way to approach quantitatively the surface tension is to think about it as an excess energy of the system. In 3D each molecule in a solution has six neighbors except of

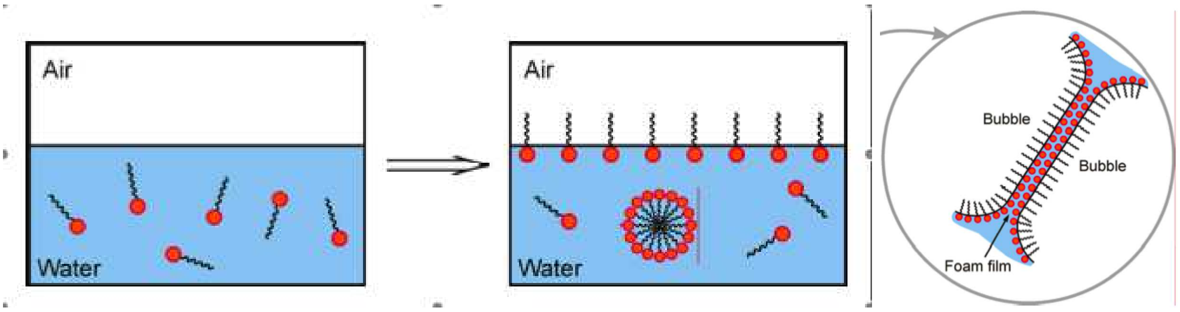

(a) (b)

FIGURE 4. Surfactant in water. The hydrophobic tails of the surfactant at the surface are oriented towards the air (a) and form in this way the films (b) separating the bubbles.

those in the surface layer that have only five neighbors. From here if we write the total energy of the system, we have:

$$E_{tot} = N_B(\mu_0 - 6u_0) + N_S(\mu_0 - 5u_0) = N_{tot}(\mu_0 - 6u_0) + N_S u_0 \tag{71}$$

and the surface energy which is the last term on the right hand side is $E_S = \sigma A$. It follows for the surface tension σ that

$$\sigma \approx \frac{N_S u_0}{A} \tag{72}$$

where A is the area of the surface, N_B and N_S are the number of bulk and surface molecules respectively, μ_0 is the viscosity and u_0 the intermolecular energy.

Since the behavior and properties of foams as a complex system can differ considerably from their individual components the statistical characterization of the system is very useful and often the only way to follow the evolution in time and space of a foam consisting of a large number of bubbles. Generally there are two principal statistical indicators extensively used by the foam community. For two dimensional foams it is the average area of a bubble $\langle a \rangle$ and average number of sides per bubble $\langle n \rangle$. In three dimensions the equivalent parameters are the average volume $\langle V \rangle$ and average number of faces $\langle f \rangle$. It can bring an additional valuable information to calculate the moments of all the listed indicators, so for the number of faces for instance one has for the m-th order moment $\mu_m = \langle (f - \langle f \rangle)^m \rangle$.

If we now step back to the length-scale of individual bubbles and investigate their arrangement in a foam it is useful to recall the Euler's rules for convex polyhedra that relates the number of faces (f), edges (e) and vertexes (v) of these geometrical features such that $v - e + f = 2$. In two dimensions, knowing that the Plateau borders are three folded, we can easily get the average number of sides $\langle n \rangle = 6$, that justifies the observation that the best tiling of 2D space in terms of minimal surface is the honeycomb arrangement 5(a). This is just another view of the von Neumann's law (von Neumann, 1952). The original form of von Neumann's law states that the rate of the area change of bubbles scales linearly with the number of sides of the bubbles, the proportionality factor $\kappa' = \pi\kappa\sigma/3$ being the product of the surface tension σ and the diffusion constant κ. Using this we have for the rate of the area change of each bubble

$$\frac{da_i}{dt} = \kappa'(n-6) \tag{73}$$

Practically it means that in a two dimensional soap froth only the six-sided bubbles are stable, those with less sides will shrink and with more than six sides will grow. This was experimentally verified by Glazier and Stavans (Glazier and Stavans, 1989). The growth rate is affected by the viscosity and gas solubility of the liquid and the pressure difference between bubbles. In two-dimensions the growth-rate of a bubble depends upon bubble topology only, irrespective of the precise geometry. This is not the case for bubbles in three-dimensional foams, however if the dispersion about such a law is small, the average growth-rate of f faced bubbles is usually expressed as a function of f only.

In three dimensions there is an extra degree of freedom, so the equation for the number of faces per bubble are under-determined. In three dimensions if the average number of faces per bubble is $\langle f\rangle$ and the average number of sides per face is $\langle n_f\rangle = 2e/f$ then for an infinite forth these quantities are related as

$$\langle f\rangle = \frac{12}{6-\langle n_f\rangle} \tag{74}$$

The rate of transfer of volume across the boundary is proportional to the face area times the pressure difference, so a general form of the growth rate in three dimensions may be written in terms of a vector $\vec{H}$ normal to the surface with magnitude of the mean curvature H and the effective diffusion constant κ as

$$\frac{dV}{dt} = \kappa \oint_{surface} \vec{H} \bullet ds \tag{75}$$

By definition, $H > 0$ on convex faces, which favor bubble shrinkage. Unlike in two dimensions, in the three-dimensional growth rate equation it does not appear explicitly what is the critical number of bubble faces which would distinguish the growing from the shrinking bubble. In two dimensions the number of sides for bubbles with zero growth rate can be related to the two dimensional minimal space filling with six sided honeycomb cells. In three dimensions there also exist suggestions for an ideal shape in terms of minimal surface. The best portitioning of space into equal-volume cells, using the least interface area was considered already by Lord Kelvin (Thomson (Lord Kelvin), 1887) who proposed a solution in the form of a truncated octahedron (tetrakaidekahedron). According to Weaire and Phelan (Weaire and Phelan, 1994) a foam with two different cell shapes uses 0.3% less space. In one translational unit cell there are two dodecahedra and six 14-hedra. This Weaire-Phelan foam in figure 5(b) has been verified by simulations, but not experimentally on larger volume foams.

1.3. Dynamical processes in foams

. Two processes will be of primary interest in this work: coarsening and drainage. For the understanding of them we shall first define the pressure in the bubbles. Referring to figure 2 it has been shown by Young and Laplace (1800) that the two curvatures R_1 and R_2 are related

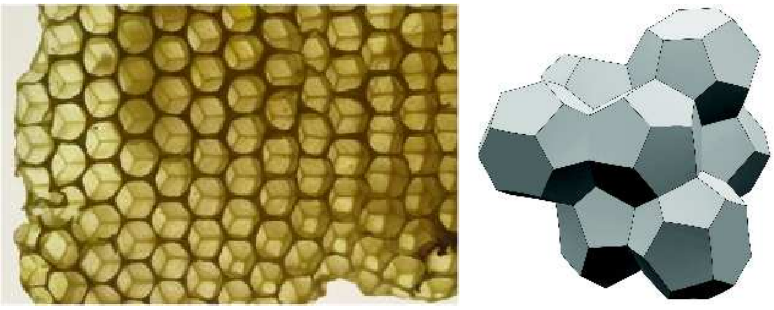

(a) (b)

FIGURE 5. Minimal interface tiling in 2D, the honeycomb cells (a) and in 3D the Weaire-Phelan construction of the foam (b)

to the pressure difference across the film and the surface tension σ (energy per area) of the continuous phase by the formula

$$\Delta P = \sigma \left(\frac{1}{R_1} + \frac{1}{R_2} \right), \tag{76}$$

If taking $\sigma = 1$ in equation 76 it is simply twice the mean curvature (expression 70). The Laplace pressure also describes the pressure inside the Plateau borders and reveals its dependency on the liquid fraction ε. The more liquid the foam contains, the rounder the bubbles are and hence bigger the radius of curvature of the film at the Plateau border. If considering then three equal bubbles as shown in figure 6, we have from equation 76 that if $\varepsilon_1 < \varepsilon_2$ then also $P_{liq1} < P_{liq2}$ which is the correspondence between the gradient of the liquid fraction and the pressure gradient.

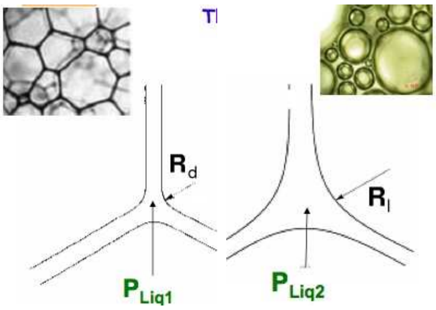

(a) (b)

FIGURE 6. The pressure in Plateau borders in dry (a) and in wet (b) foam

The liquid fraction of a foam may change in time and space as drainage occurs. Foam drainage is the flow of liquid through the interstitial spaces between the bubbles. The flow is driven by capillarity and (usually) gravity and is resisted by viscous damping. The drainage due to gravity is the naturally occurring phenomenon in liquid froth. Since the flow downwards due to gravity outweigths the capillary flow, the drainage by gravity is the dominant mechanism for freely draining foams. Its different regimes has been extensively studied in the literature (see for example (Saint-Jalmes and Langevin, 2002) where a discussion on different foam parameters influencing the drainage regime is presented). The correlation of drainage, coarsening and foam rheology is illustrated in figure 7. The change in liquid fraction accelerates growth because gas diffuses more rapidly between thinner bubble membranes and Plateau borders.

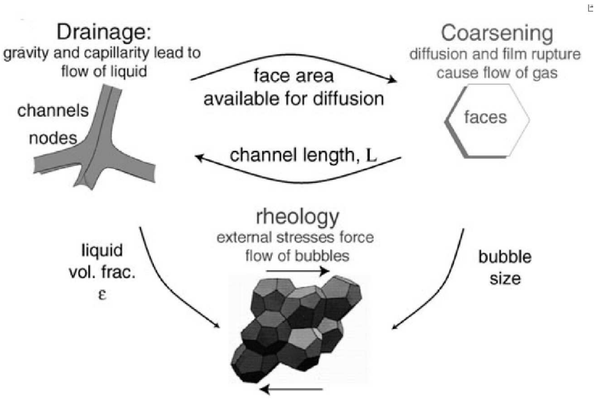

FIGURE 7. A very complex interaction between bubble topology, size and the dynamical processes related to drainage. This figure illustrates that coarsening and drainage goes hand in hand. By increasing bubble size the drainage rate increases and vice-versa as the foam drains the amount of liquid separating bubbles changes, which affects the rate of diffusion of gas.

Drainage hence influences foam coarsening. The latter happens by means of specific processes. In two dimensional foams there are two basic topological processes by which coarsening occurs. They are shown in figure 8. When two bubbles come together and push apart two other bubbles, we say that a T1 process occurred. The T1 process does not alter the number of bubbles in a given volume. The T2 process would decrease the total number of bubbles by one as a three sided bubble disappears. In addition one could consider the special case of wall breakage of an n-sided bubble as an elementary process as well. Plateau's rules which are the basis of most descriptions of foam structures, dictate that junction of more than four Plateau borders are always unstable. The T1 transformation for instance goes through a state with such a junction and this may explain that it happens at a very high speed and therefore is often referred to as an instantaneous process. In three dimensions there are two different T1 processes. The disappearance of a face or the disappearance of a Plateau border. The T2 is the disappearance of a tetrahedre.

If a foam does not break down too early it can enter a special state in which all the statistical distributions and correlation functions for all dimensionless quantities are constant in time. We call this regime the *scaling state*. One way to look at a given foam for two different instances t_1 and t_2, $t_1 \leq t_1$ in a scaling state is to consider the foam for t_2 a zoom-in of the foam at t_1. The scaling factor is a matter of discussion between foam physicists. In two dimensions the situation is rather simple and Von Neumann's law (73) predicts that the average area of bubbles scales with the square root of t, as the dimensional analysis also predicts.

To relate the growth rate to bubble topology one could argue that in equation 75 the vector $\vec{H}$ should be the same for bubbles of different sizes but the same shape. Therefore if divided by

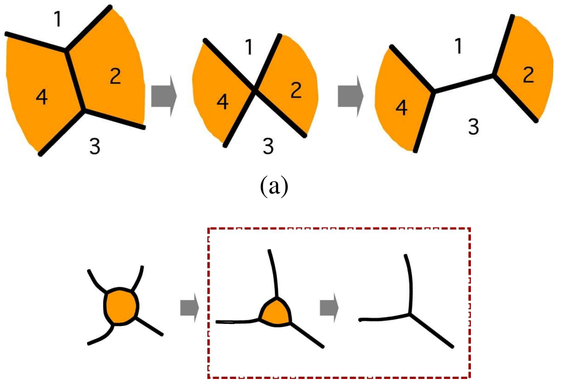

(a)

(b)

FIGURE 8. elementary topological processes in two dimensions. Side swapping - T1 (a) and disappearance of a three sided bubble - T2 (b)

$V^{1/3}$ the growth rate will depend only on bubble shape and not on bubble size. The growth law of the individual bubble volume in 3D can then be written in terms of the pressure difference Δp_i of two bubbles separated by a face with index i, and the area S_i, resp. their sum taken over each face (Glazier, 1993):

$$G = \frac{3}{2D_e}\frac{dV^{2/3}}{dt} = -\frac{1}{2}\sum_i \frac{\Delta p_i S_i}{\sigma V^{1/3}} \tag{77}$$

The effective diffusion coefficient D_e of the gas across the bubble walls, and the wall tension $\sigma = 2\sigma_{air-water}$, are assumed to be constant and only play the role of a multiplicative factor that can vary from one to another foaming solution. The growth of grains in crystals is similar to foam coarsening, but without the time-scale separation, so that grains do not equilibrate. It is thus easier to study grains than foams. Departing from the assumption that grains are regular and weakly curved, Mullins (Mullins, 1989) predicted analytically an expression for G as function of f only which changes sign at 13.3. With the same logic he showed that if the grains reached a scaling state, the grain size distribution $P(R)$ should obey $d\left\langle R^2\right\rangle/dt = const.$ Grain growth simulations suggested that such a scaling state does exists and Mullins expression was numerically confirmed by Wakai (Wakai *et al.*, 2000) using Surface Evolver(Brakke, 1992) to simulate a collection of one thousand grains.

The growth rate of bubbles is again more difficult to investigate. The only strictly exact 3D theoretical result is a necessary but not sufficient condition. If a scaling state exists, the average bubble size R, surface S, volume V must grow with time with exponents with the scaling factors $0.5,\ 1$ and 1.5 respectively. Mullins has deduced this in 1986 (Mullins, 1986) for both foams and grains from the scaling characteristics of V and from a statistical self similarity hypothesis according to which consecutive configurations of the system in the self-similar mode are geometrically similar in a statistical sense. Glazier later showed (Glazier and Prause, 2002) the short dimensional argument

$$\frac{dV_f^{2/3}}{dt} = \frac{1}{V_f^{1/3}}\frac{dV_f}{dt} = k(f - f_0) \tag{78}$$

from which the scaling factor values directly follow in the dry foam limit. It also suggests that the average volume rate of change for a group of bubbles with f greater than a threshold value f_0 will grow, while bubbles with a smaller f will shrink. For the relation between f and f_0 Weaire and Glazier (Weaire and Glazier, 1993) deduced that

$$f_0 = \langle f \rangle \left(1 + \frac{\mu_2}{\langle f \rangle^2}\right), \tag{79}$$

where $\mu_2 = \langle f^2 \rangle - \langle f \rangle^2$ measures the disorder of the foam. Equation 79 is exact provided that the average volume of a bubble with f faces scales as $\langle V_f \rangle \propto f^3$, as it followed from Glazier's Potts model simulations. For wet 2D and 3D foams we have the Lifschitz-Slyozov law: $\frac{dV_f}{dt} = k(\frac{1}{R} - \frac{1}{R_0})$.

To summarize and underline again our motivation, in 2D there is no controversy in the characterization of the scaling state, however in 3D this special state of liquid foams has not yet been experimentally followed. Only very recently, Potts model simulations (Thomas *et al.*, 2006) could give some insight into the scaling-state-like behavior of 3D foams and check if the theoretical prediction for the scaling factors are correct. And it is at this point where the advanced 3D imaging that was developed at ID19 finds it's unique application in that it helps to verify the existence and properties of a time independent scaling state-like behavior of 3D foams.

2. The imaging of foams

2.1. The observation methods

. The observation of the complex structure that liquid foams are (especially in 3D) has been very time demanding when bubbles had to be counted visually one by one. In addition the foam properties are intrinsically statistical which explains why only very recently certain important characteristics for these 3D systems have been observed. In 2D, as usually, the situation is simpler and an optical camera is enough to record the foam and eventually its dynamics. From simple projections it is required to go to tomography to observe the same in 3D. This step is not so simple for the liquid foams. The reasons are mainly twofold: (1) high light diffusivity and meanwhile little amount of matter involved and (2) often rapid evolution.

Trials have been performed with magnetic resonance imaging (Glazier and Prause, 2002; Gonatas *et al.*, 1995) and optical tomography (Monnereau and Vignes-Adler, 1998), but none of these techniques could provide data with high statistical weight. The first started with 200 bubbles and ended with 40, whereas the second reconstructed only 48 bubbles. Currently there is an outlook to eventually use also neutron coherent imaging for certain liquid foams, but no experimental data is available yet. This brings us to the conclusion that synchrotron x-ray tomography is the most promising technique for evolving liquid foam structure and dynamics determination with a sufficiently good statistical weight.

The technique will be described in this chapter, starting with the sample preparation in section 2.2, then image processing in sections 2.3, 2.4 and finishing with the interpretation of results in 2.5.

2.2. Foam preparation

. To match the possibilities of the imaging system it is important to master the fabrication of the foam. The principal requirements are:

(1) A foam evolution slow enough to obtain usable tomograms. One scan typically lasts 20 to 30 seconds, a time period within which the sample should not change its structure in order to record on all the radiographs the information about the same state of the foam
(2) A foam evolution fast enough to observe the dynamical processes within the time of the experiment that is of the order of 3 to 5 days.

In addition to these we must of course add the requirements posed by the physical interest in the results. Those include:

(1) The control of the liquid fraction.
(2) The choice of nominal bubble size as compared to the field of view of the imaging setup so that good statistics can be obtained.
(3) The control of the degree of polydispersity of the foam.

The ensemble of all the requirements determines the choice of the composition of the foaming solution and the method of fabrication which is strongly biased by the design of the containers in which the sample is imaged. The cells containing the foam during the x-ray experiment are hollow plexi-glass cylinders with thin walls ($\cong 0.5$ mm) and inner diameter of 15 mm equal to the field of view of a 2048×2048 pixels CCD detector mounted on an optics providing $7.46\ \mu$m pixel size. The bottom part of each cylinder houses one or two porous media as can be seen on the drawing in figure 9. If the porous medium is wetted by the foaming solution that resides on the top and gas is pushed from the bottom bubbles are created inside the cylinder. The pore size of the discs determines the initial bubble size. We have used two different pore sizes usually one at a time but also a combination of two in the same cell with the goal to produce a bi-disperse foam. The pore sizes used in the experiement were $10 - 16$ (P1) and $16 - 40\mu$m (P2). By appropriate gas-flow-regulation a bubble by bubble build-up of the foam can be achieved.

The other possible method of foam preparation is to use an external foam-producing instrument as for example a mighty whipper, which is basically a kitchen tool. It has been found to be excellent in producing polydisperse dry foams. Such an externally produced foam can easily be transfused into a cell. The porous media do have an important function in this approach as well. Through them the liquid fraction is regulated. The foam imprisoned between them and the top cover of the cell will experience forced drainage if depression is introduced by simply extracting the gas from the cell through the porous media which will not allow the foam itself

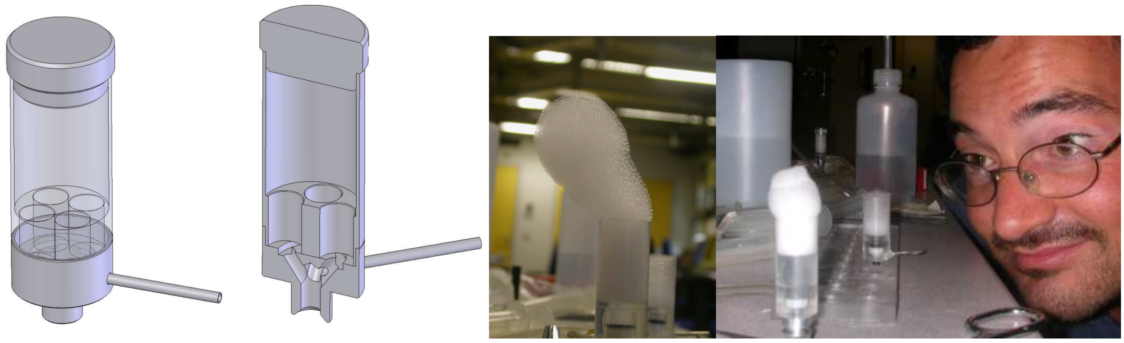

(a) (b) (c) (d)

FIGURE 9. Drawing of the plexi-glass cylinder (a) housing the foam during the experiment. In (b) the inner view shows the round structures where the porous media are placed. The channels from the bottom feed the foaming solution or the gas depending on the regime of foam preparation. (c) and (d) shows the foam during preparation by bubbling through the porous medium.

to escape the cell. The gas extraction can be performed using a syringe or just manipulating the height of the water column in a tube connected to the bottom of the cell. This process is reversible, that is to increase the liquid fraction it is enough to ’re-increase’ the pressure in the cell. This variation of the liquid fraction as a function of the height of the water column in the tube connected to the cell with the foam is visible in figure 10.

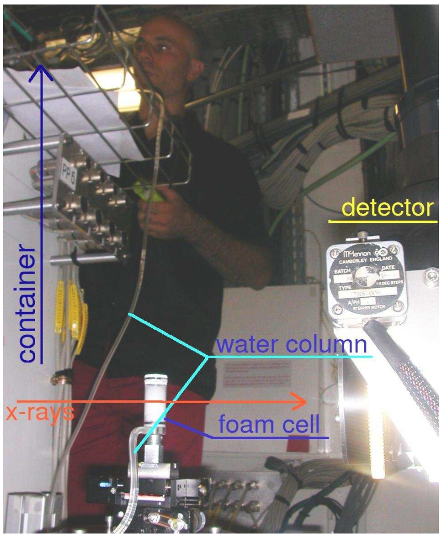

FIGURE 10. Liquid fraction variations by changing the height of the water column hence the hydrostatic pressure that determines the pressure in the cell as well. The cell with the foam on the sample stage connected via a tube to a container with the foaming solution. This container is placed at a selected height depending on the hydrostatic pressure one wants to get at the level of the cell.

Several types of foams have been investigated, those which occur in this work are listed in table 1 together with their principal characteristics. A more detailed overview including foams that have been scanned but still are in the process of analysis is given below. For each sample one tomographic slice is shown at the time of the first observation and another slice being the last tomogram acquired.

	evolution	ϵ	composition	dispersity
shaving foam	slow	0.034 "mid-dry"	shaving foam	poly-
bubbling 1	fast	0.02 dry	water+3.5 % Dreft	almost mono-
MWD	moderate	0.01 very dry	water+3.5 % Dreft+C_6F_{14}	poly-
MWW	slow	0.08 "mid-wet"	water+3.5 % Dreft+C_6F_{14}	poly-
MW	slow	$0.06 - 0.02$ dry	water+3.5 % Dreft+C_6F_{14}	poly-
bubbling 2	fast	0.02 dry	water+3.5 % Dreft	mono-

TABLE 1. Summary of the observed foams. The first two foams have undergone a correlation study during their evolution. The third foam is mentioned later in the text, the last three foams have not been analyzed yet.

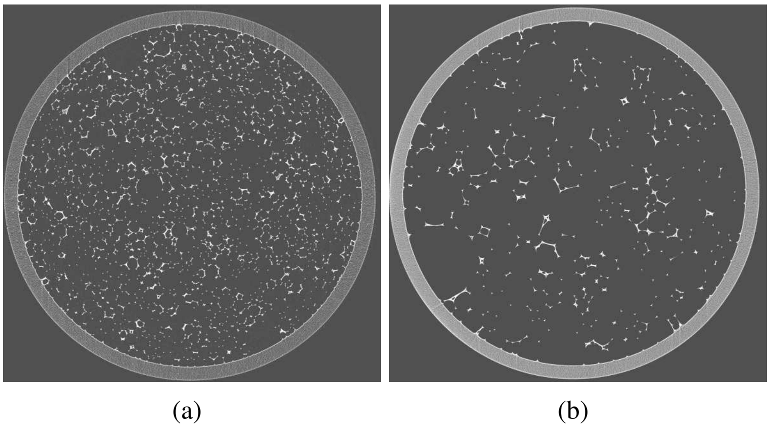

(a) (b)

FIGURE 11. The **shaving foam.**

composition:: shaving foam from a commercial container.
preparation:: from the container transferred directly to the cell. From the sealed cell, liquid has been removed by small depression and then the cell is closed again.
characteristics:: mid-dry foam, slowly evolving
lifetime:: $>$ 6 days, images acquired from age of 24 h to 110 h

2.3. Data acquisition

. The synchrotron source provides partially coherent x-ray beam, therefore phase contrast is present in the recorded images. Depending mostly on the liquid fraction, it is desirable to adjust the appropriate amount of observed phase contrast by changing the defocus distance. In the case of parallel beam imaging which has been applied on liquid foams, this is achieved by varying the sample to detector distance. The range for the variation of sample to detector distance at ID19 is 1 m. The propagation distance between the sample and the detector is equivalent to the defocus and will thus be varied in function of the amount liquid fraction of the studied foam. For most of the dry foams studied here this distance has been kept small and absorption was the principal process contributing to the contrast on the images. However for the driest samples we increased the defocus distance to allow more phase contrast as the little amount of material in

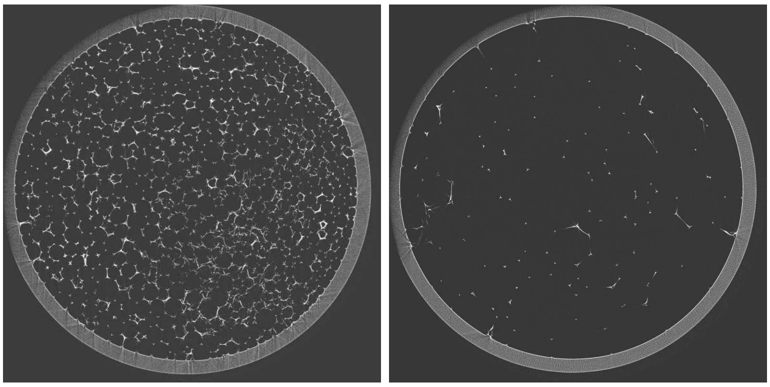

(a) (b)

FIGURE 12. The **fast bubbling foam**

composition:: Dreft washing up liquid (3.5 %) in water
preparation:: Bubbling through the $10 - 16\,\mu$m porous medium.
characteristics:: dry foam, rather monodisperse fast evolution
lifetime:: ≈ 1 hour, images acquired from age of 2 min to 65 min

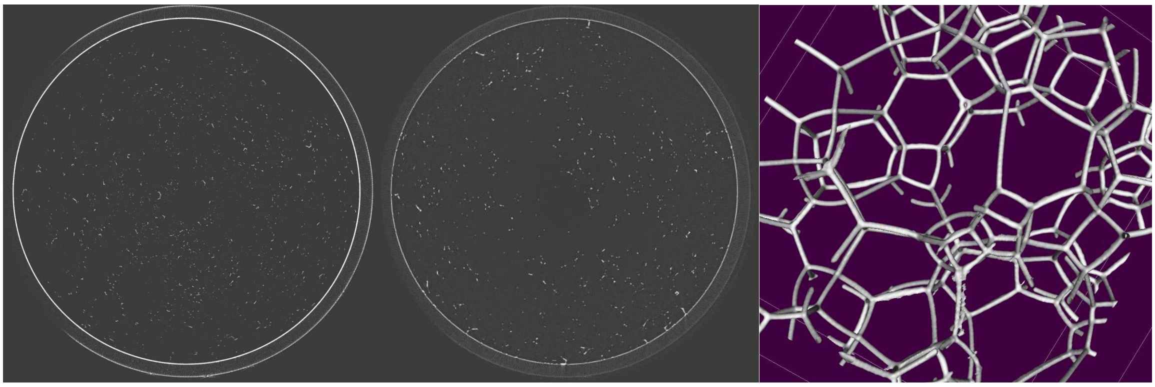

(a) (b) (c)

FIGURE 13. The very **dry Dreft foam - MWD.** The isosurface corresponding to the Plateau borders of a selected region is shown in (c).

composition:: Dreft washing up liquid (3.5 %) in water, several drops of stabilizer C_6F_{14}
preparation:: mighty whipper
characteristics:: very dry foam, slowly evolving, polydisperse
lifetime:: > 1 day, images acquired from age of 5 min to 24 h

very dry foams doe not produce enough contrast by absorption. Although the phase information is present, for the foam imaging it is not required to retrieve it when reconstructing the volumes. The reason is that we are interested only in the well defined interfaces between bubbles instead of exact quantitative information, that would require phase retrieval. Moreover the propagation technique, as described in Chapter 2, requires images at more defocus distances, but for evolving systems as foams are, there is a difficulty to record more scans with the same state of the sample. The filtered back-projection algorithm was thus used directly on the projections irrespective on the presence of phase contrast.

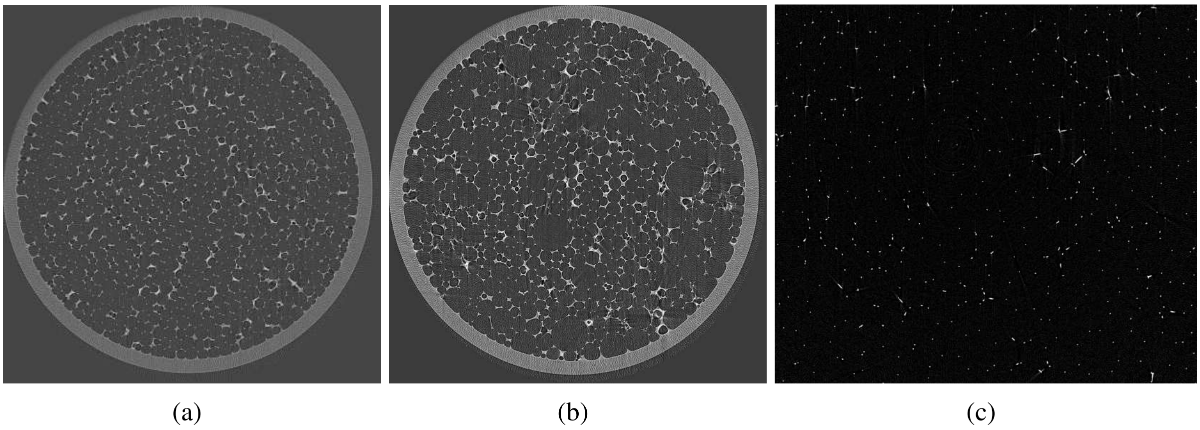

FIGURE 14. The **monodisperse foam(s).**

composition:: Dreft washing up liquid (3.5 %) in water
preparation:: Bubbling through the $10 - 16\,\mu$m porous medium.
characteristics:: dry (a) and (b), monodisperse foam, in (c) a different foam of the same composition, but very dry. Fast evolution for both
lifetime:: < 45 min, images acquired from age of 2 min to 40 min

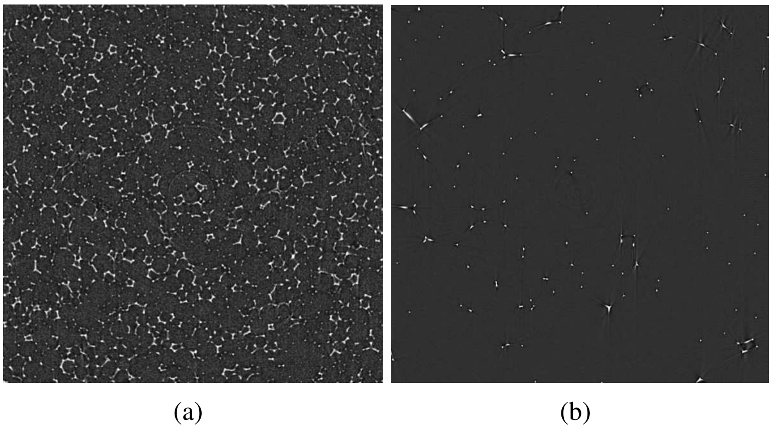

FIGURE 15. The dry Dreft foam - MW

composition:: Dreft washing up liquid (3.5 %) in water, many drops of stabilizer C_6F_{14}
preparation:: mighty whipper
characteristics:: mid-wet in the beginning, then drainage till it became a very dry foam at ≈ 12 h, very slow evolution, but significant drainage, polydisperse
lifetime:: > 1 day, images acquired from age of 5 min to 30 h

Several foams have been prepared, some in advance before the start of the experiment and some during the experiment. Five foams have been selected to follow their time evolution during a long period in time (typically more than one day), hence the tomography has been performed in parallel in the sense that different cells with foams have been alternated in the beam. Each foam has been placed in the beam to take a series of typically 10 scans with a time interval of the order of 5 to 10 minutes and then exchanged for the next foam. For the extraction of dynamical parameters it is sufficient to acquire short series separated by a longer

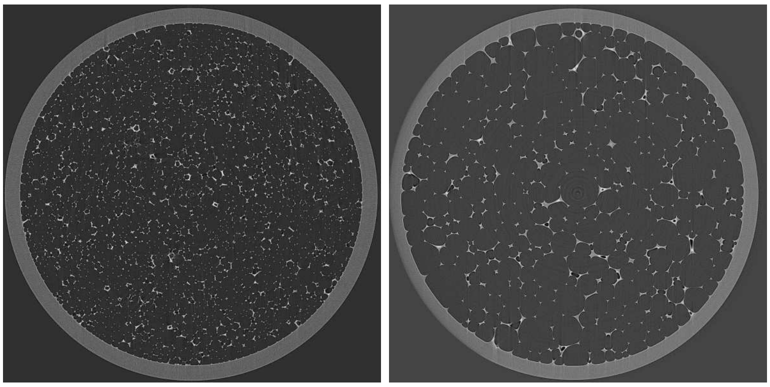
(a) (b)

FIGURE 16. The mid-wet Dreft foam - MWW

composition:: Dreft washing up liquid (3.5 %) in water, several drops of stabilizer C_6F_{14}

preparation:: mighty whipper and overpressure in the cell to assure higher liquid fraction

characteristics:: "mid-wet" foam, high liquid fraction gradient from the top to the bottom of the cell, polydisperse

lifetime:: > 1 day, images acquired from age of 5 min to 26 h

time. The only inconvenience of this approach may be the difficulty to follow individual bubbles throughout the whole series.

Particular attention has been paid to the shaving foam. Two runs of observation of the shaving foam include a series of scans at the age $t \approx 24 - 34$ h which is to record the initial parameters and more importantly the series at the age of $t \approx 89 - 132$ h which was expected to give distributions near scaling state regime. The FReLoN2k14 detector in FTM mode recorded 1200 projections per scan with exposure time $t_{exp} = 90$ ms, resulting in total scan time of ≈ 3 minutes including reference and dark images. This configuration was appropriate for the slowly evolving foam. The sample to camera distance has been set to 50 mm in order to have a moderate phase contrast contribution as is optimal for the contrast and resolution in the image. This foam contains sufficient amount of material (water) to have good contrast at small defocusing distances.

2.4. Extraction of key quantifiers from three-dimensional images of complex systems

. In this subsection we describe the data processing applied to various foam images. For each method we will give an example illustrating the performance of the procedure.

2.4.1. *Segmentation and liquid fraction*

. Among the most "straight-forward to obtain" foam characteristics extractable from the 3D x-ray tomograms of foams we count the liquid fraction. It gives access to the **distribution of fluid** in the sample. The forced variation was mentioned in the previous subsection, the gravity-induced drainage results in a liquid fraction variation from top to bottom of the container in which the foam is placed. Figure 17 qualitatively shows such a variation. For all the foams the straight-forward and robust calculation of the liquid fraction is performed by thresholding the image and performing an erosion-opening operation in order to suppress the alone standing pixels (considered to be due to noise). Afterwards the ratio of the white pixels representing the liquid and the total number of pixels gives the value of the liquid fraction. In general, there are cases when a slight variation in the threshold value in the image can significantly influence the result. To eliminate this effect, for all the scans presented here, three threshold values were simultaneously used for the liquid fraction measurement. No important variation was observed (see figure 19) thanks to the good quality of the images.

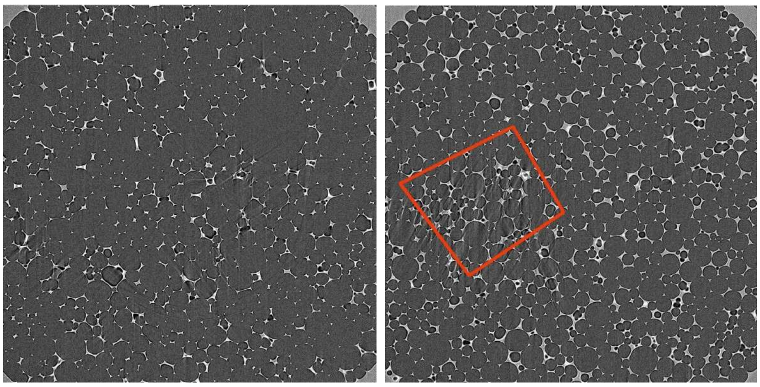

(a) (b)

FIGURE 17. Liquid fraction variation on a Dreft foam. A slice at the top of the cylinder (a) and a slice at the bottom (b), both separated by ≈ 7 mm, visualize the effect of displaying by gravity. The bubbles are seemingly rounder and smaller towards the bottom of the cylinder. Note also the red rectangle highlighting a zone where movement goes on during the scan.

The segmentation and liquid fraction determination can be done with the commercially available image processing tool 'Aphelion'. Before determining the threshold value, the image histogram is sharpened using a filter, which most often is a non-linear median filter with the $3 \times 3 \times 3$ core. The threshold value is set manually for each sample and kept constant for the entire series of scans of the same sample. The choice of the threshold value should ensure that after an erosion operation (i) there are no scattered white pixels corresponding to noise and that (ii) the value is high enough to avoid the appearance of white pixels due to ring artifacts that are present in some scans. Whenever these ring artifacts were occasionally present in the scans, the threshold value was increased for the complete series. It was however checked that the vertexes are preserved and that the higher threshold value does not hinder the labeling procedure of the bubbles. This robustness can be attributed to the high quality of the reconstructed volume.

One possible classification criterium of foams is the value of their liquid fraction. In this work we focus on the study of dry foams. The existing theories explaining foam behavior often assume the foam to be dry. The lack of their experimental verification explains our choice. Within the term “dry foam” we will address foams with liquid fraction $\varepsilon \simeq 0.005 - 0.05$ which may be considered as the complete range in which foams are said to be dry.

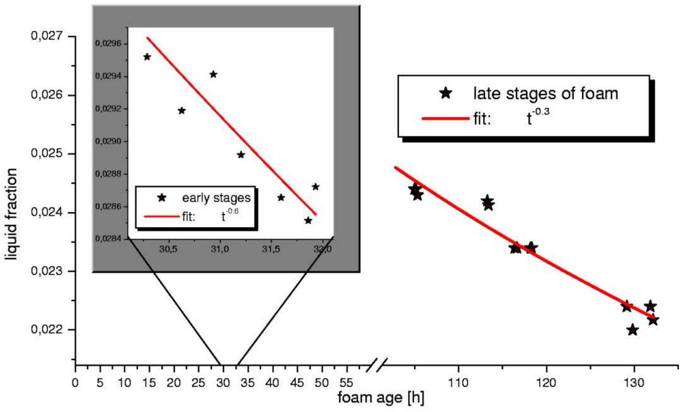

FIGURE 18. This figure shows the drainage in time for the shaving foam throughout the experiment. The 24 h break in the x axis corresponds to the separation between the two runs during which the foam was studied.

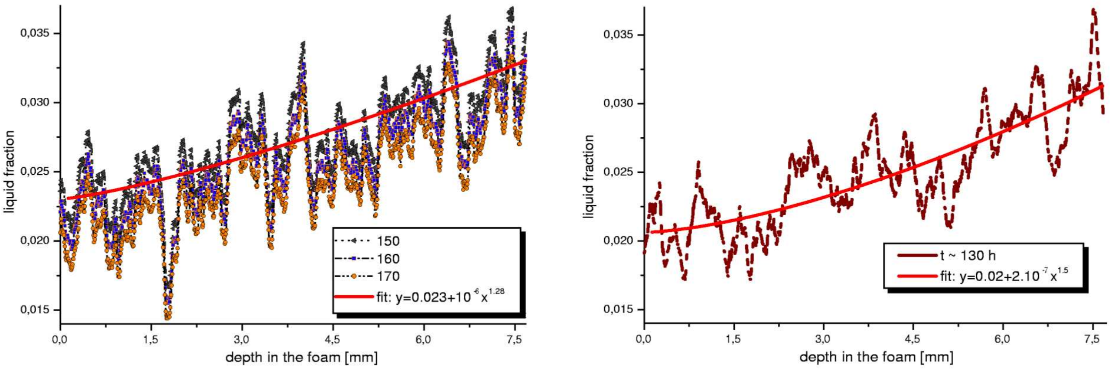

(a)

(b)

FIGURE 19. The liquid fraction variation in the volume of the shaving foam at the age of 80 (a) and 132 hours (b). The three different threshold values 150, 160 and 170 (out of the full gray-scale, 0 to 255) in (a) result in almost identic profiles. The mean value was $\varepsilon = 0.026$ for threshold 160. A power fit is also shown in the figure with exponent 1.28 (a) and 1.5 (b).

The shaving foam on which the analysis procedure will be illustrated falls into the middle of this interval. This foam has been followed during 5 days starting 24 hours after its preparation. Although this foam may not be a typical candidate for a liquid dry foam we have observed evolution of its structure during the whole experiment which confirmed that it can be considered as a liquid foam. The forthcoming analysis certifies our assumption. The preparation process included a short period of depression in the cell that has reduced the initial liquid fraction whose mean value at the beginning of the observation was $\varepsilon_i \approx 0.04$ and at the last observed image $\varepsilon_f \approx 0.02$. It is useful to track the rate at which the liquid volume fraction decreases with time. On the scale of single bubbles the flow is very complicated: liquid moves through channels from node to node where the flow merges, mixes and splits. Also the liquid-air interface flows in some

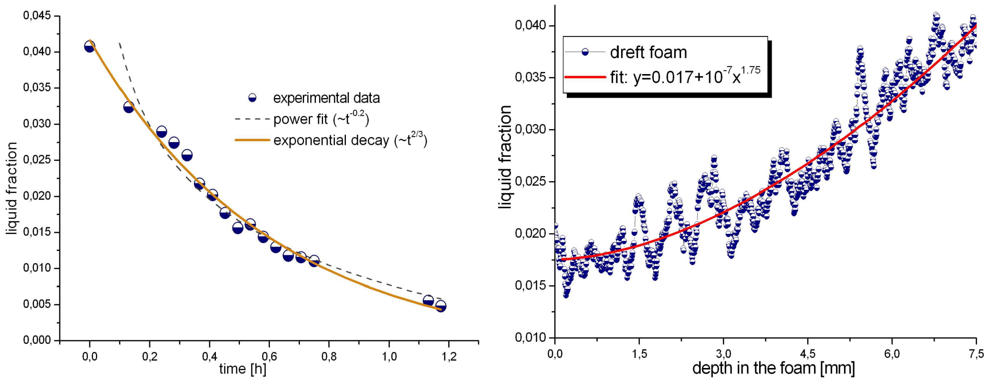

(a) (b)

FIGURE 20. The temporal (a) and spatial (b) variation of the liquid fraction for the fast evolving Dreft foam (see 12) prepared by the bubbling method.

complicated fashion along the channels. However on a macroscopic scale simple ordered flow is often observed and it is possible to successfully describe foam drainage using simple models. Simulations using the channel-dominated drainage equation applied to free drainage predict that $\varepsilon \sim t^{-2/3}$ (Koehler *et al.*, 1999) for points close to the top of the foam. Figure 18 presents a fit with the exponent $-2/3$ in the early stage and $-1/3$ in the late stages of the shaving foam.

As shown in figure 19 the spatial variation of liquid fraction is relatively small (as compared to other liquid foams in this study) with $\Delta\varepsilon \approx 0.01$ per cm of foam column height.

Different behavior has been observed for the Dreft foam 12 prepared by the bubbling method with the $10-16$ μm porous media. The solution was the Dreft washing up liquid diluted in water to a concentration of 3.5%. The resulting froth is a dry (medium to low end), fast evolving foam with low polydispersity degree. The initial mean liquid fraction was 1.9% going down to as low as 0.3% towards the end of its lifetime. The temporal and spatial variation of the liquid fraction can be seen on figure 20. The observed dependency is $\varepsilon \sim t^{-1/5}$, not corresponding to the predicted $t^{-2/3}$.

2.4.2. *The labeling of bubbles*

. For the extraction of other parameters it is needed to label the individual bubbles. Two distinct approaches can be used. The first of them is more suitable for foams towards the upper half of the dry foam liquid fraction scale ($\approx \varepsilon = 0.02 - 0.05$). The second approach works better in some selected cases when the foam is very dry ($\varepsilon < 0.02$) as will be illustrated on a Dreft foam. The first approach has been applied to the shaving foam. It is based on the knowledge of the property of a liquid foam that the bubbles are separated by films and each film is meeting with two other films in the Plateau borders. The thresholded image (figure 23(b)) of dry foams generally does not contain the films as their thickness rarely approaches a micrometer. The films are sometimes visible in the raw images but often fall below the resolution limit of the imaging system. Nevertheless it is possible to automate the separation of bubbles and to treat each bubble as an object with its proper label.

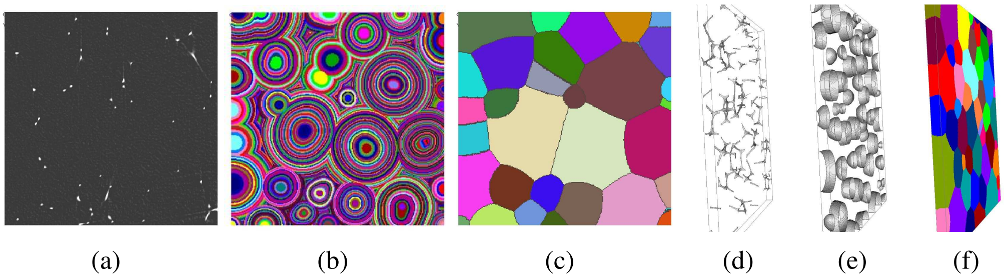
(a) (b) (c) (d) (e) (f)

FIGURE 21. The weighted distance method demonstrated on the dry Dreft foam in two and three dimensions. The first image (a) is the raw slice (enhanced by a low pass filter only) of a small section of the image. (b) is the distance map resulting from step 3 in the Weighted distance method description and (c) shows the labeled bubbles. The three-dimensional iso-surface representation of the raw sub-volume (d) enhanced by a low pass filter with core $3 \times 3 \times 3$ and its Euclidian distance map (e). The final result of labeled three dimensional foam is in (f)

Implementation and control of object splitting can be done by means of the morphological procedure called ClusterSplitConvex (CSC). A cluster is a set of connected voxel of the same value. If two parts of it are in contact via a bottleneck, an erosion procedure can separate the cluster into two parts. If the size of the bottleneck is small compared to the cluster parts being separated, the resulting separation is good but as already stated in (Lambert *et al.*, 2005) the respective Gaussian curvatures of two bubbles split this way are not recovered. To do this one would need to use a model such as Surface Evolver [1] (Brakke, 1992). At the position of the bottleneck the distance map of the voxels from the nearest liquid phase would show a local minimum of various depth depending on the width of the bottleneck. The power of separation can be tuned against the level above which a concavity creates a separation between two elements. The parameter enabling this is the 'strength' of the ClusterSplitConvex. Lower numbers correspond to higher splitting power. The value giving the best result has been chosen for each series individually by trial and error approach.

The entire volume of the foam was in this case divided into four horizontal sub-volumes of $1300 \times 1300 \times 256$ pixels in order to allow the use of the 3D procedures in Aphelion that are very memory hungry. Further down-scaling of each sub-volume by a factor of 2 is justified by the dimension of the smallest bubble after this operation. At time $t = 89$ h the volume of the smallest object in the entire volume was 270 voxels still providing sufficient resolution. For this particular foam the choice of a different optics in the experimental setup could bring more statistics as the field of view would have been increased. Some other samples presented here though required the $7.46\,\mu$m pixel size and therefore this compromise was made for practical reasons during the experiment.

---

[1] Surface Evolver is an interactive program for the modeling of liquid surfaces shaped by various forces and constraints. It takes into account the physical properties of the system and aims for maximal entropy. It available to free download at http://www.susqu.edu/brakke/evolver/

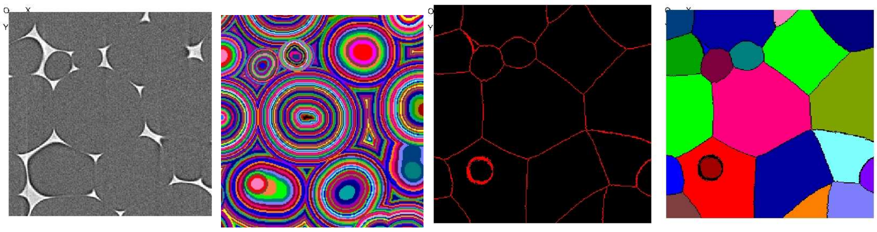

(a) (b) (c) (d)

FIGURE 22. Unsuccessful labeling using the Weighted Distance method. The example shows the processing of the shaving foam. (a) is the raw slice, (b) distance map, (c) watershed lines and (d) the labeled bubbles. Note the loss of the interface in the lower left corner which is a typical behavior of the Weighted Distance method. Due to the increased width of the liquid phase a small parasite bubble (bottom left corner of images) occurs as well.

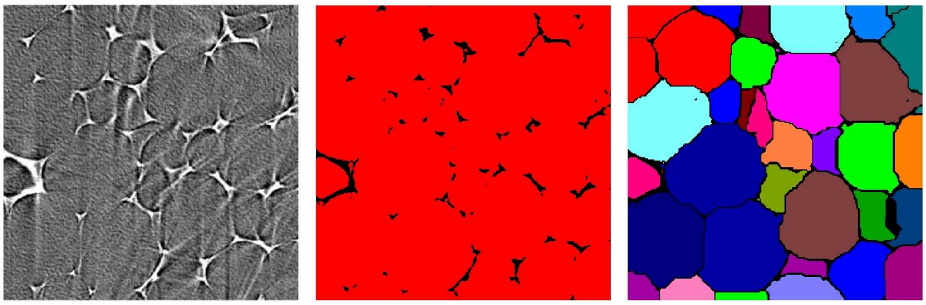

(a) (b) (c)

FIGURE 23. A raw slice (a) of the bubbling foam (12) at age of 4 min. Its thresholded (b) and binarized version eliminates the motion artifacts in the reconstruction due to structural changes during the acquisition. The labeling of bubbles (c) using the Cluster Split convex method as it was done for the first scans where the foam is more wet.

Bubbles that find themselves on the boundary of the sub-volumes are cut; they could often be merged again by knowing the relative coordinates of the sub-volumes and using the ObjectOverlap function.

Before proceeding to discuss the geometrical and topological parameters and their evolution , we describe the second approach for object recognition and labeling applied to a liquid froth. A very dry Dreft foam (see figure 13) can serve as the illustrative example. For this type of foam where mostly only the Plateau borders are visible the step following the segmentation differs from the ClusterSplitConvex method. Instead the *Weighted Distance* approach has been implemented. Using Aphelion functions the algorithm is the following:

(1) The Euclidian distance map of the thresholded image is calculated and extended regional maximas are extracted. These stand for the coordinate of the middle (the seed) of each bubble.
(2) Each of these points is attributed the value of their maximum Euclidean distance. The diameter $2R$ of bubbles are determined this way.

(3) In a cycle through all calculated $2R$ the distance map of each subset of bubbles (those with diameter $2R$) is 'weighted' by dividing it by $2R_{max}$.
(4) Finally a watershed transform is applied to the weighted distance map. The watershed transform consists in flooding a surface of a grey-scale image from its maximas and, if we prevent the merging of the waters coming from different sources, we partition the image into two different sets: the catchment basins and the watershed lines. If we apply this transformation to the image gradient, the catchment basins should theoretically correspond to the homogeneous grey level regions of this image. However, in practice, this transform produces an important over-segmentation due to noise or local irregularities in the gradient image. A major enhancement of the watershed transformation consists in flooding the topographic surface from a previously defined set of markers and with predetermined speed. Both are given in our case, the first by the positions of the bubble seeds, the second by the weighted distance map.

The sequence of the method is illustrated in figure 21.

In certain cases, especially for foams with slightly higher liquid fraction, artifacts may occur (figure 22) and the ClusterSplitConvex proves to be more adapted. The same holds in the case when the tomograms are affected by motion artifacts. The CSC is robust enough to approximate well the bubble shapes and number in partially degraded images (see figure 23). The WD even with the constrains put on extended local maxima determination, overestimates the number of bubbles by splitting those which are in reality one unique bubble or in contrary, and this occurs more often, small bubbles are not recognized. There are hence two tools for labeling of the bubbles and it is a matter of choice that depends on the foam which method is more appropriate.

2.4.3. *Accessing the foam geometry*

. Having the bubbles labeled, we can investigate the appropriate quantities for different types of foams. We will start with the shaving foam already introduced. Each scan represents the state of the foam at a given moment in time. By just exploring a single tomographic scan, several parameters can be attributed to each object or to the ensemble of objects in the studied volume. (An object is a labeled bubble).

With a statistical approach the **bubble geometry** can be quantitatively described in terms of relative dimensionless parameters such as the relative volume $\overline{V} = \frac{V}{\langle V \rangle}$, surface $\overline{S} = \frac{S}{\langle S \rangle}$ and bubble diameter $\overline{R} = \frac{R}{\langle R \rangle} = \frac{V^{1/3}}{\left\langle V^{1/3} \right\rangle}$.

The histogram of relative bubble volumes distribution at the beginning of observation $t = 89$ h are shown in figure 24. For the same instances the histogram for the relative surface and bubble diameter can be found in figure 25.

2.4.4. *Accessing the topology*

. The **bubble topology** and **geometry-topology correlations** will be addressed next. Many of the topological parameters may be considered as dependent only upon the number of faces. As the first of them we shall look at the distribution of the number of faces f itself by means of a

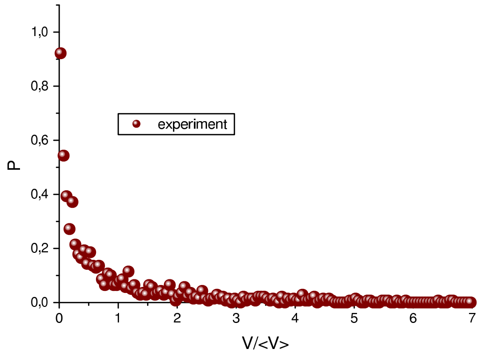

(a)

FIGURE 24. The frequency of bubbles as a function of their relative volume $\bar{V} = \frac{V}{<V>}$ at $t = 89$ hours from the shaving foam fabrication.

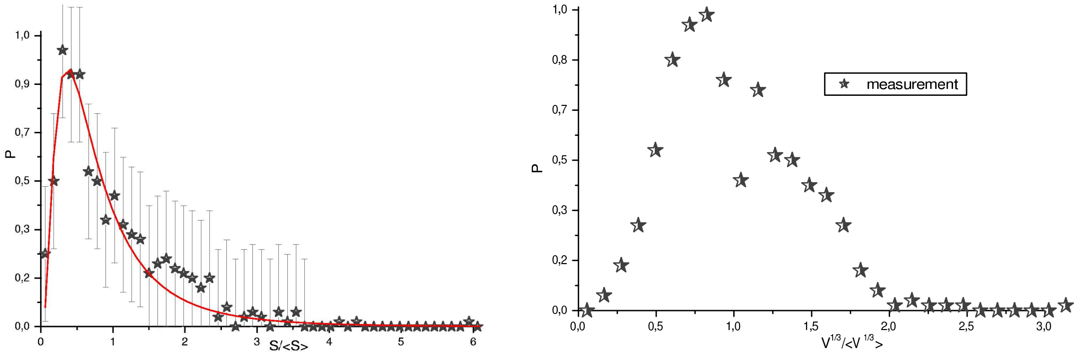

(a) (b)

FIGURE 25. The frequency of bubbles as a function of their relative surface $\bar{S} = \frac{S}{<S>}$ (a) together with a lognormal fit and relative diameter (b) $\bar{R} = \overline{V^{1/3}} = \frac{V^{1/3}}{<V^{1/3}>}$ at $t = 89$ hours.

histogram in figure 26. The plot is representing a relatively early stage of the foam. The distribution peaks at $f_{peak} \approx 9$. This distribution is calculated on the whole foam volume. Looking at each of the four sub-volumes (vertically slicing the whole volume) separately, one could also check the influence the vertical coordinate on the distributions. Unlike the liquid fraction the mean volume and surface does not show any dependency on the height in the approximation of the limited statistics available when addressing only individual sub-volumes.

The averaged volume $\frac{\langle V_f \rangle}{\langle V \rangle}$ distribution as function of the number of faces f is plotted in figure 27 for an early time, $t = 24$ h. Another f-dependent parameter is the surface averaged over the number of faces. In (Thomas *et al.*, 2006) the linearity of the distribution of the averaged surface as a function of the number of faces is the input parameter for the simulations. By the evaluation of the experiment it is of course not needed to make such assumptions and hence figure 28 may be regarded as a check provided that the studied foam is in the scaling state. To determine this latter statement first the necessary conditions must be fulfilled as defined above

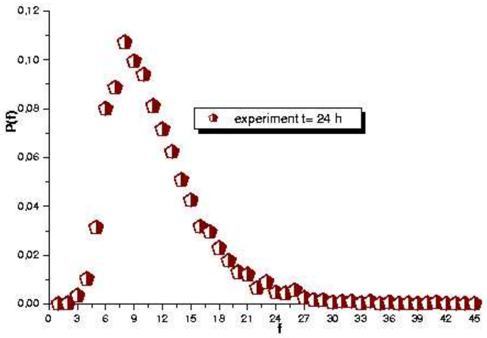

FIGURE 26. The populations in each bin representing the number of faces of the bubbles in the whole system. The experimental data points are an average of three successive scans of the shaving foam at the age of ≈ 24 hours.

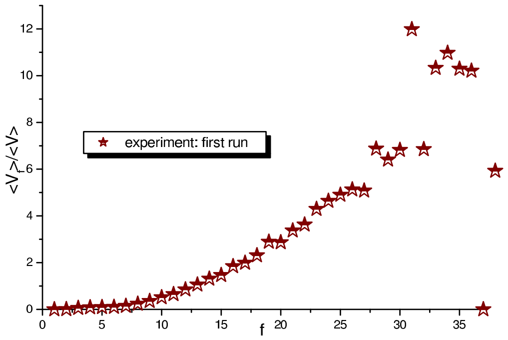

(a)

FIGURE 27. The averaged relative volume $\frac{\langle V_f\rangle}{\langle V\rangle}$ as function of the number of faces f. The stars are the experimental data at $t = 24$ h.

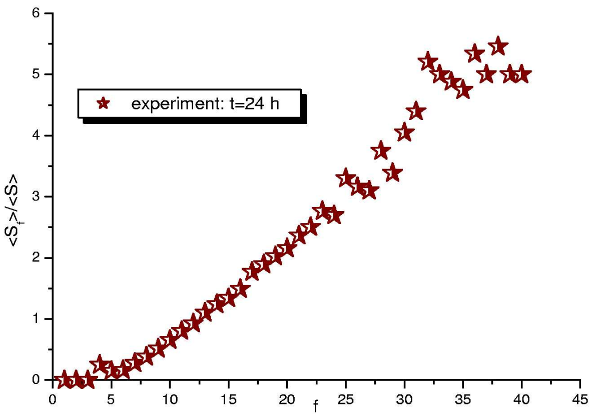

FIGURE 28. The averaged relative surface $\frac{\langle S_f\rangle}{\langle S\rangle}$ as a function of the number of faces f. The stars are the experimental data at $t = 24$ h.

for the scaling of $\bar{V}$, $\bar{R}$ and $\bar{S}$ with time. The time dependence of these and other characteristic parameters for the foam are studied in the next subsection.

2.5. Following the evolution in liquid foams far from and close to the scaling state

. The shaving foam for which the determination of geometrical and topological parameters obtainable from the tomographic images was presented, is an example of a polydisperse, dry (medium to high end) foam that evolves very slowly, staying alive for several days. Basically the contrary in many aspects has been observed for the "bubbling foam" (see figure 12 in the foam list). The crucial difference for the last froth in what concerns the adjustment of the imaging setup is the rapid coarsening. The foam started to break down already in less than 1 hour after preparation, hence the data had to be acquired in this short time interval. For this it was required to set the exposure time to its minimal value of 60 ms bringing us to a scan time of approximately 25 s if 400 projections per scan are acquired. The coarser angular step deteriorates the tomogram quality, but 400 steps for an image of 2048 horizontal pixels appears still as a reasonable compromise for a quickly evolving sample. The defocusing distance has been increased to 120 mm to allow for more phase contrast (less material in the foam therefore less contrast). The coarsening was quicker for the first minutes after preparation, but as can be seen in figure 23 the images are still usable.

The reason to start the section on foam dynamics with this example is twofold. Firstly, it is to demonstrate the feasibility of accessing the structure of a fast evolving system. Secondly, such a foam is expected to have properties that vary differently as what is believed to happen in a scaling state regime. In such a way the comparison with a foam near the scaling state can be made more demonstrative.

First of all an important starting point is to know what is the statistics based on, since it is going to be crucial for certain quantifiers. The sub-volume of the bubbling foam processed in this case contains $N_0 = 1046$ bubbles (excluding the bubbles that are cut on the borders) at the beginning, and 126 bubbles in the last scan. This evolution is shown in figure 29.

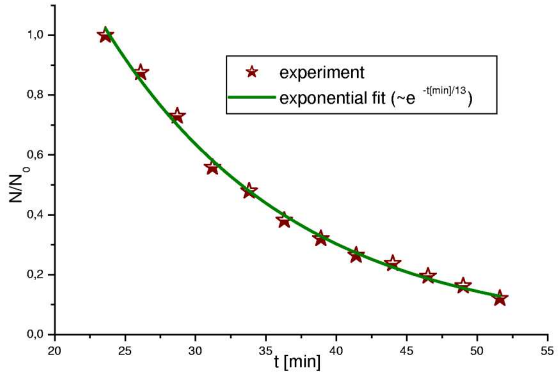

FIGURE 29. The relative number of bubbles N/N_0 as a function of time for the bubbling foam. The fit is an exponential decay with decay time $t_{dec} = 13$ min.

Next, the parameters important from the evolution point of view and in the same time accessible in real experiments, can be sorted into three categories. The first category groups those parameters that are robust and represent the necessity condition for a foam to be in the scaling state. They are hence used to validate the possibility that the foam is in an assumed state. This category comprises $\frac{\langle V_f\rangle}{\langle V\rangle}$, $\frac{\langle S_f\rangle}{\langle S\rangle}$, $\langle V\rangle(t)$, $\langle S\rangle(t)$ and $\langle R\rangle(t) = \left\langle V^{1/3}\right\rangle(t)$. The second category comprising the distribution of the number of faces, $P(f)$ and the geometrical descriptors $\frac{V}{<V>}$, $\frac{S}{<S>}$ and $\frac{V^{1/3}}{<V^{1/3}>}$ can be referred as the parameters that prove that the studied system is in the scaling state. Finally into the third category the complementary parameters have been put. These are the characteristics of foams which can give valuable information on it's state, but are generally very sensitive to any circumstances of the experiment or even simulations. Therefore these has to be considered while keeping in mind the limited confidence. We can name here the growth rate $G(f)$, the average number of faces $< f >$ and its second moment μ_2. Eventually the measures of volume polydispersity defined as

$$\frac{\sigma_R}{R} = \frac{\sqrt{\left\langle (R - \langle R\rangle)^2 \right\rangle}}{\langle R\rangle} = \frac{\sqrt{\left\langle \left(V^{1/3} - \langle V^{2/3}\rangle\right)^2 \right\rangle}}{\langle V^{1/3}\rangle} \tag{80}$$

and topological polydispersity $\frac{\mu_2}{\langle f\rangle^2}$ may be followed in time.

For the bubbling foam the average volume and surface of bubbles as a function of their number of faces shows a dispersion in time as can be deduced from the plots in figure 30(a) and (b).

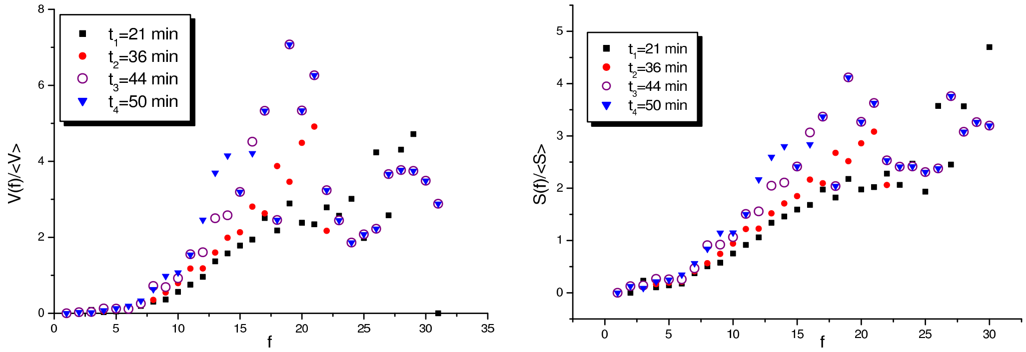

(a) (b)

FIGURE 30. $\frac{\langle V_f\rangle}{\langle V\rangle}$ (a) and $\frac{\langle S_f\rangle}{\langle S\rangle}$ (b) for the fast evolving bubbling foam at times $t_1 = 21$ min, to $t_4 = 50$ min. The dispersion of the curves is very significant.

The time evolution of the average volume and bubble diameter show again very irregular shape (figure 31).

The peak of the distribution of bubbles in bins with different number of faces shifts towards the smaller number when approaching the end of the lifetime of this foam. Furthermore it is easy to see from figure 32 that this distribution changes its shape significantly between the initial and final state.

Finally the growth rate curve shown in figure 33 crosses zero at around 14.5 but the statistics of less than 1000 bubbles give limited confidence in the exact value. It can be concluded that the necessary conditions for scaling state are not fulfilled for this foam and therefore, as expected,

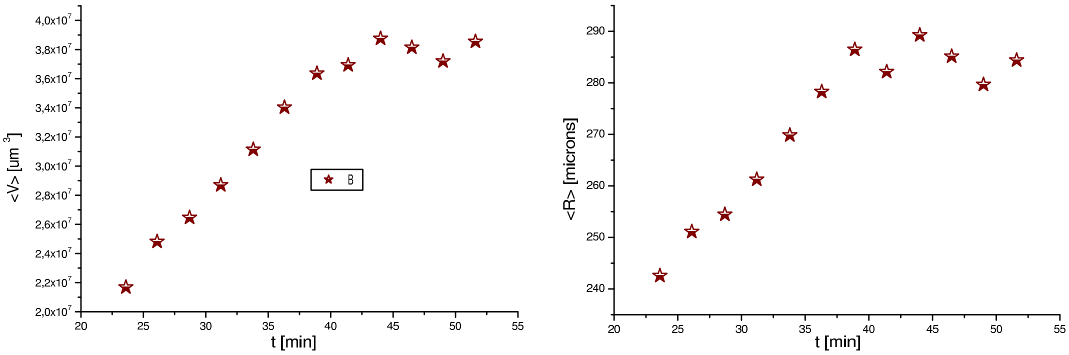

(a) (b)

FIGURE 31. Time evolution of average volume (a) and particle size (b). Both curves are dependent on the definition of the particle size; They have similar shapes which shows two different regimes separating at around 40 minutes of foam age.

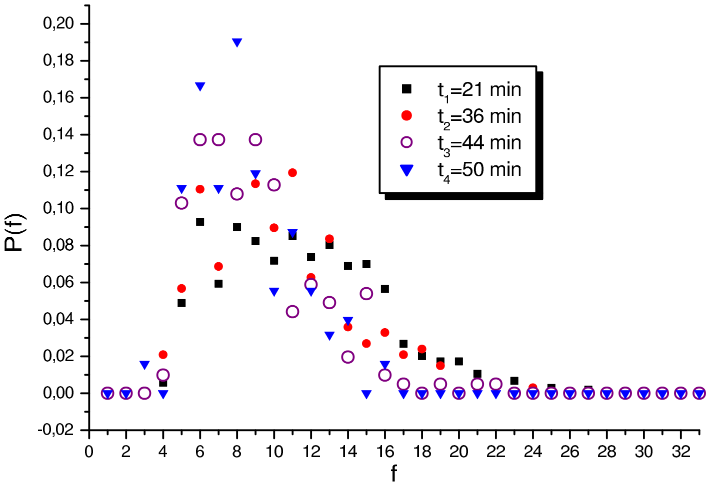

FIGURE 32. The distribution $P(f)$ of bubbles with respect to their number of faces, shown for four different times. Note the change in shape. In spite of the bad statistics it is obvious that at later times the FWHM becomes smaller as the curves get thinner and shift towards smaller f.

this foam is not in scaling state. The foam was relatively monodisperse at the beginning (see figure 12(a)) which also means that there would be a long transition time before the scaling state.

We shall now return to the shaving foam sample. Careful planning for the shaving foam sample preceded the experiment in order to approach as closely as possible the scaling state. As mentioned there have been two runs of scanning, therefore a time break is present in some graphs that follow. The initial and final state of this foam is shown in figure 11.

The relative number of bubbles, $\frac{N(t)}{N_0}$ evolves in the way shown in figure 34. Note that though N_0 is here referred to as the initial bubble count, it is not entirely true. The foam was

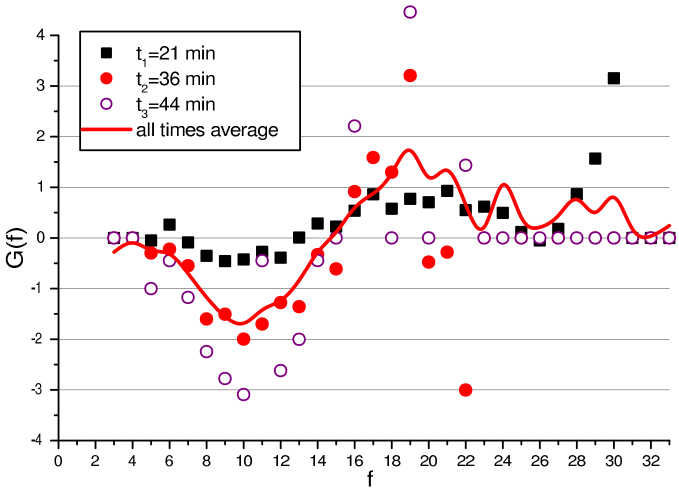

FIGURE 33. The average growth rate as function of number of faces. The zero intercept is at $f_0 = 14.5$. The red solid line is the average over the times $t = 36$ to 50 min. The position of f_0 does not change significantly for those late times of the foam life.

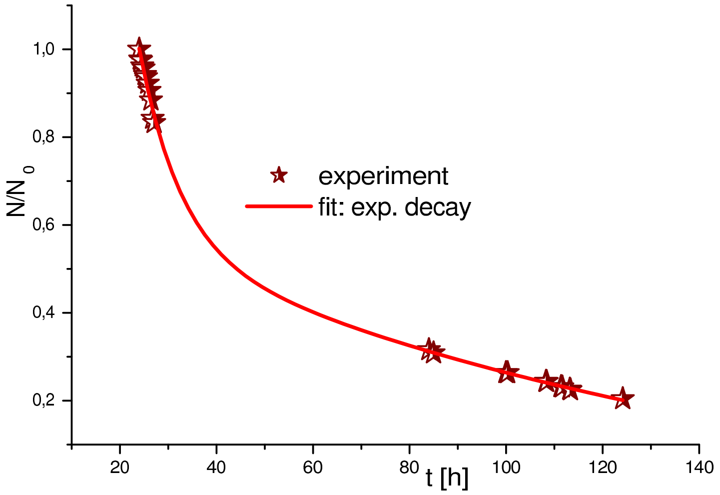

FIGURE 34. Relative number of bubbles N/N_0 for the earlier and later series of the shaving foam. The initial number of bubbles was 3400. Fitted with a second order exponential decay function with the two decay times 8.4 and 137 hours for the first and second run respectively.

aged ≈ 24 h when the first tomographic scan has been acquired and because the bubbles have not been counted at the moment of the shaving foam preparation, the actual initial conditions are unknown. Moreover the region of observation of the foam in the first run and the second has different dimensions, therefore the number of bubbles in the second run was normalized to the volume of the first run which was smaller. This allows to plot them in the same chart. The relative volume and surface as function of the number of faces were already presented for a given moment in time. The stability of these parameters is now demonstrated in figure 35. The Potts model simulation data for a 3D foam in the scaling state regime is also presented

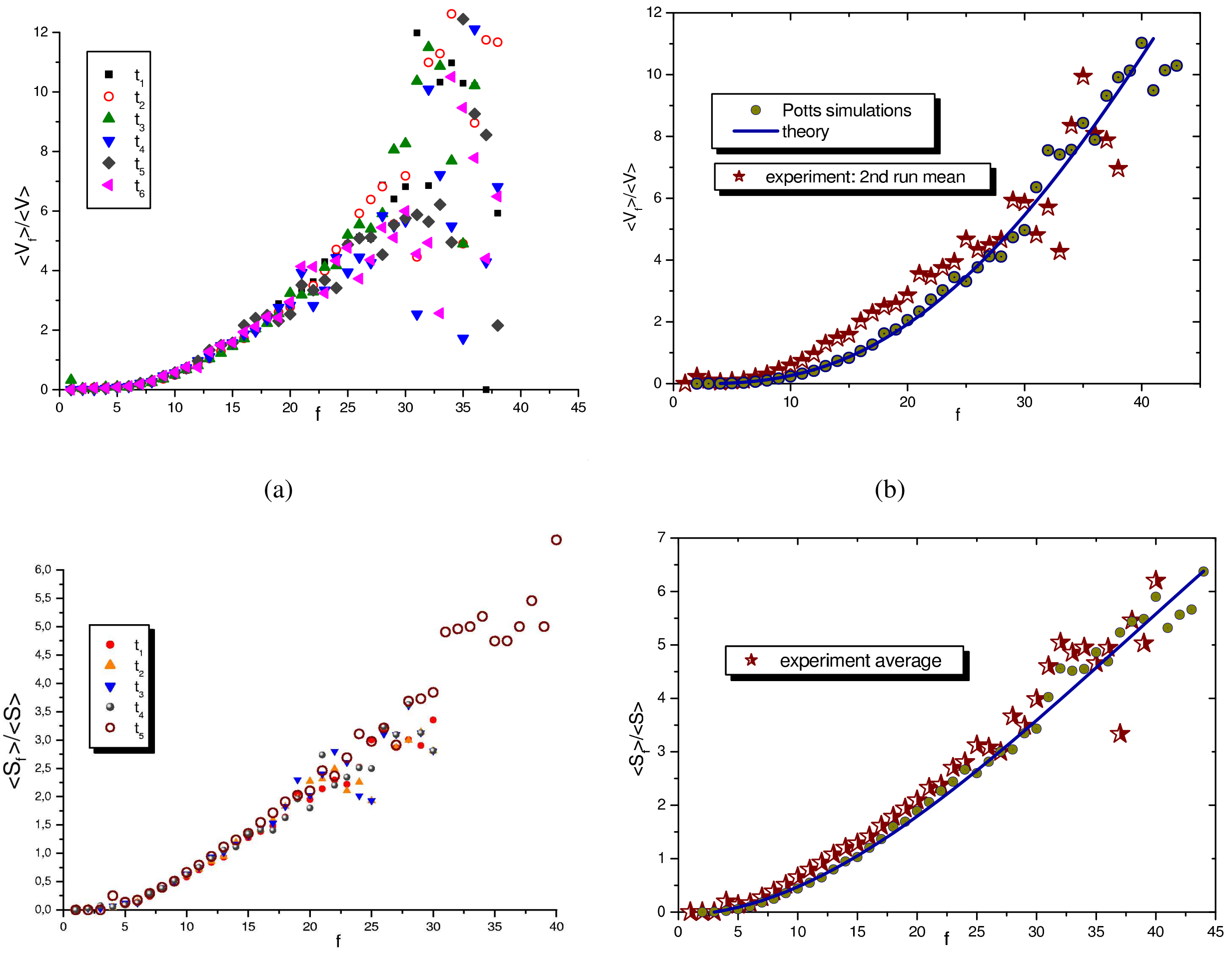

(a) (b)

(c) (d)

FIGURE 35. $\frac{\langle V_f\rangle}{\langle V\rangle}$ (a, b) and $\frac{\langle S_f\rangle}{\langle S\rangle}$ (c, d) for the shaving foam at times $t_1 = 24$ h , $t_2 = 25$ h, $t_3 = 27$ h, $t_4 = 89$ h, $t_5 = 100$ h and $t_6 = 130$ h (t_6 only for $V(f)$). (b) and (d) show the average of the second run of the experimental values together with the Potts model simulations and the theoretical values represented by the solid line. In Thomas et al. the assumption that the $\frac{\langle S_f\rangle}{\langle S\rangle}$ is a linear function of f was the input parameter for the simulation. (d) could be considered as the experimental verification of this assunmtion.

on this figure. The results of the simulations were provided by the authors of (Thomas *et al.*, 2006). These are the only extensive simulations for 3D foams and was an inspiration for the layout of this document in terms of the selection of parameters. The simulations start at an initial population of approximately 2.25×10^6 bubbles for three initial foam configurations: normal, lognormal and bidisperse. At late times the distributions of all parameters for the three types converge to the same values. Experimentally we typically observe $10^3 - 10^4$ bubbles at the birth of the foam. For the shaving foam there were 3400 bubbles at time $t = 24$ h when the first image has been taken. The question was if the experimental data-point will approach the simulation. Indeed, as demonstrated in this chapter, they are closer closer to the simulation results than to the theory that has also been developed in (Thomas *et al.*, 2006). The plots show that these distributions are very stable in time and that the averaged relative surface $\frac{\langle S_f \rangle}{\langle S \rangle}$ is in very good agreement with the simulations, while the averaged relative volume $\frac{\langle V_f \rangle}{\langle V \rangle}$ exhibits a slightly flatter shape.

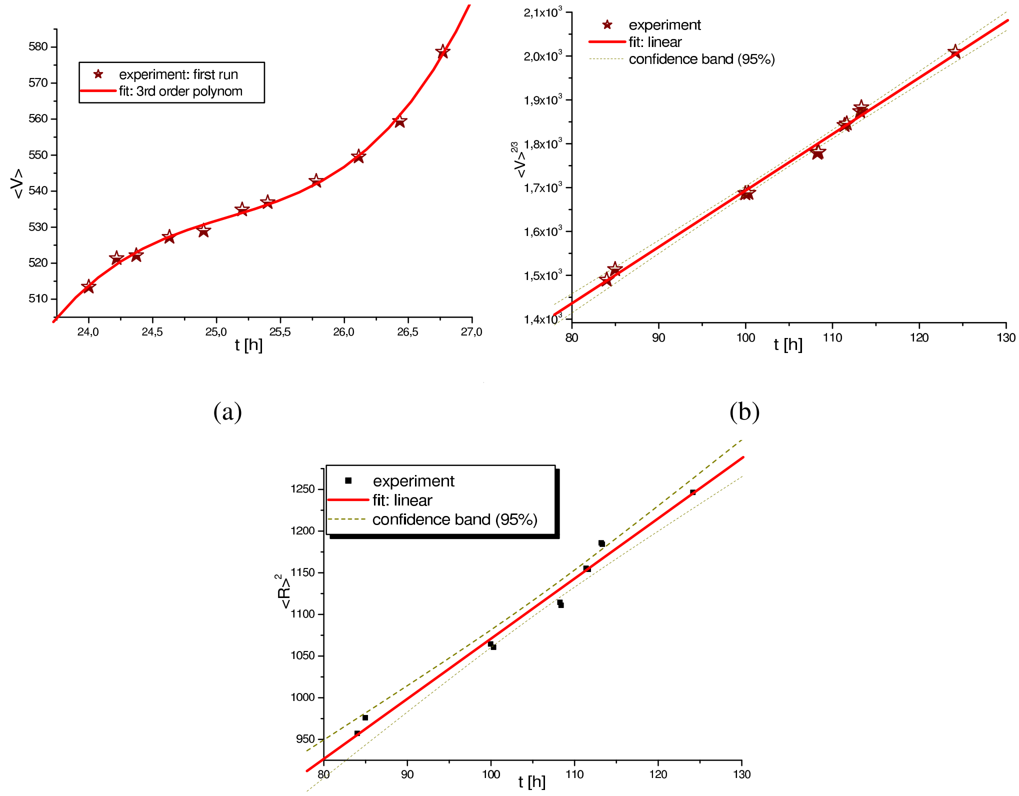

(a) (b)

(c)

FIGURE 36. The time evolution of the averaged geometrical parameters: $< V >$ (a) for the first run and for the second run $\langle V \rangle^{2/3}$ (b) and $\langle R \rangle^2$ (c) in the case of the shaving foam.

The other necessary conditions for the scaling state can be investigated by plotting $\langle V \rangle^{2/3}$, $\langle S \rangle$ and $\langle R \rangle^2$ as a function of time. Figure 36 shows these quantities for the second run hence for the old foam. The linear behavior is satisfactory to proceed to the next step of the foam status determination. It will consist of the investigation of the behavior of relative size, surface area and volume distribution functions. Given for two distinct times these parameters are again stable as can be seen in figure 37. The last quantity from the second group of parameters is the distribution function of the number of faces (see figure 38).

Finally the complementary parameters may be addressed, such as the average growth rate $G(f)$ as a function of the number of faces. The parameter f_0 separating in the topological space the bubbles that grow from those who shrink was attributed various values in 3D depending on the particular model or experiment as reported by several authors. For simulations these values range from 13.3 (Mullins, 1989) and 13.4 (Fortes, 1986) for symmetrical bubble theories,

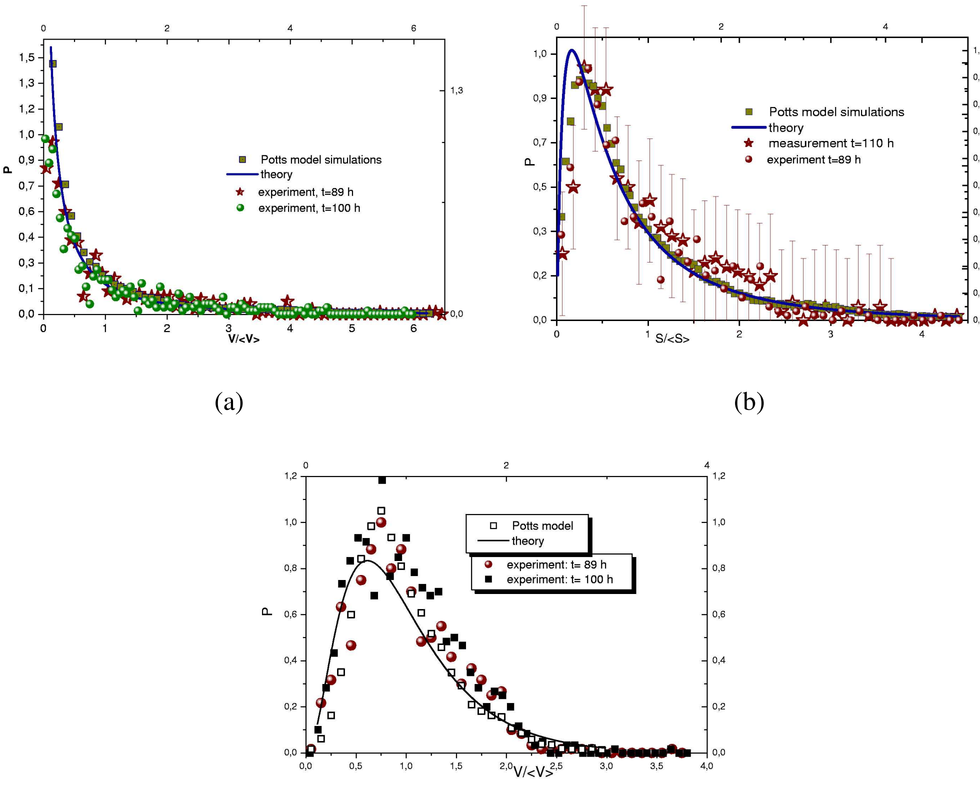

(a)

(b)

(c)

FIGURE 37. The distribution functions for relative volume $\frac{V}{<V>}$, surface $\frac{S}{<S>}$ and size $\frac{V^{1/3}}{<V^{1/3}>}$ at two different times during the second run. The Potts model simulations in the scaling state and the solid line for the theoretical prediction are shown in the graphs to compare the experimental values. The experimental data fit better to the simulations than to the theory.

to 13.8 or 14.8 (Wakai *et al.*, 2000) for surface evolver simulations and even 15 for vertex models and 15.8 for the simulations of Glazier (Glazier, 1993). The latter will serve as one of the references in the figures. From optical tomography a value of 13.3 ± 0.1 (Monnereau and Vignes-Adler, 1998) was deduced,while from magnetic resonance measurements 12 ± 2 was obtained (Burkhard *et al.*, 1999). We aim to add another experimental data point to this scattered chart, doing so by means of figure 39. It is based on the first experimental data with good statistics. From the figure it is apparent that the shape of the experimental curve differs from the simulations mainly in the region of small number of faces f. This may be an artifact resulting from the experimental data. However if we focus on the region near the zero intercept, there the experimental points match better the simulations of Glazier than those of the Potts model. The value of the zero intercept is much higher than the $< f >$ as has been noted in earlier works as well. We measure $f_0 = 14.7$. If we refer to formula 79 suggested by Glazier, and substitute the measured mean values of μ_2 and $< f >$, the result is encouraging sine we obtain a value of 14.62, which is close to the f_0 from figure 39.

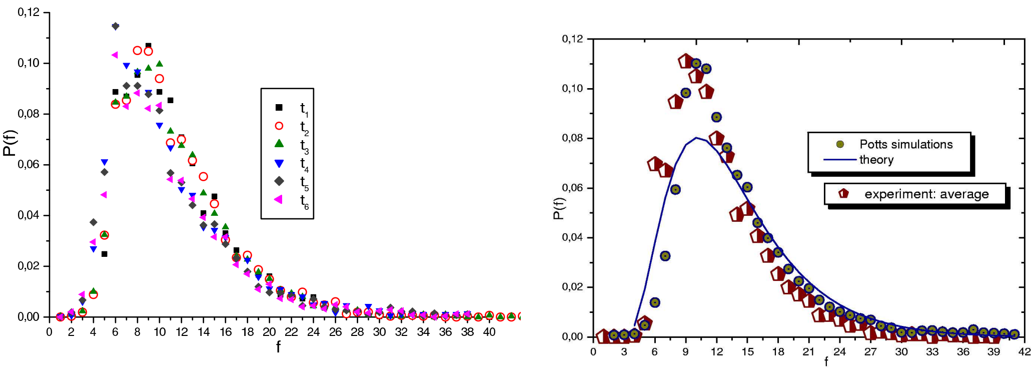

(a) (b)

FIGURE 38. The distribution of the number of faces for bubbles in the shaving foam (a) at times $t_1 = 24$ h , $t_2 = 25$ h, $t_3 = 27$ h, $t_4 = 89$ h, $t_5 = 100$ h and $t_6 = 130$ h. (b) shows the average over the second run as compared to the Potts model simulations and the theoretical curve.

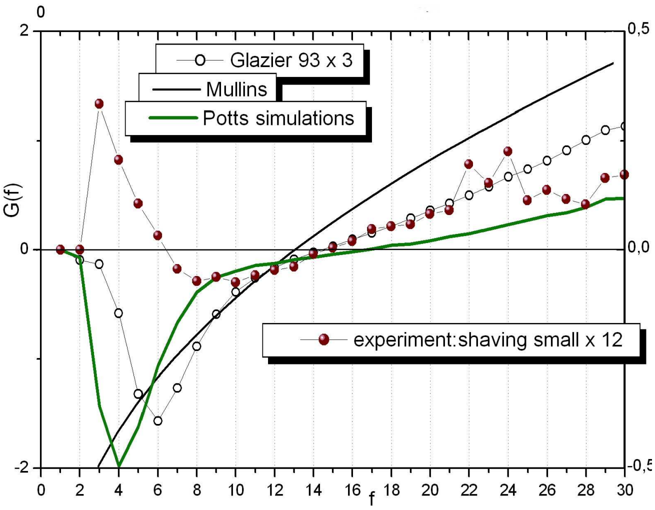

FIGURE 39. The growth rate for the shaving foam as function of the number of faces of bubbles in the foam. The experimental data with a pre-factor of 4 is plotted by filled spheres. The solid lines are the Potts model simulations and the circles are the simulations of Glazier (Glazier, 1993).

Several physical parameters to characterize the disorder or dispersion of the system may be addressed as well. The average number of faces and its second moments are according to the theory in (Thomas *et al.*, 2006) expected to stabilize if in scaling state; $\langle f \rangle$ at the value of 13.7 in accordance with the simulations and μ_2 at ≈ 37. Graph 40 shows the experimental values of these quantifiers. The mean number of faces is lower than in the simulations and varies slightly more. The second order moment is a parameter very sensitive to the statistics and therefore is difficult to determine precisely. This may be the reason for the small discrepancy in the shape of the Potts model simulations, where the circles in (d) represent small simulations. Figure 40(d) may also be an indicator of how to find the relative matching regions in time of the simulations and the experiment, in other words to estimate the state of the shaving foam in correlation

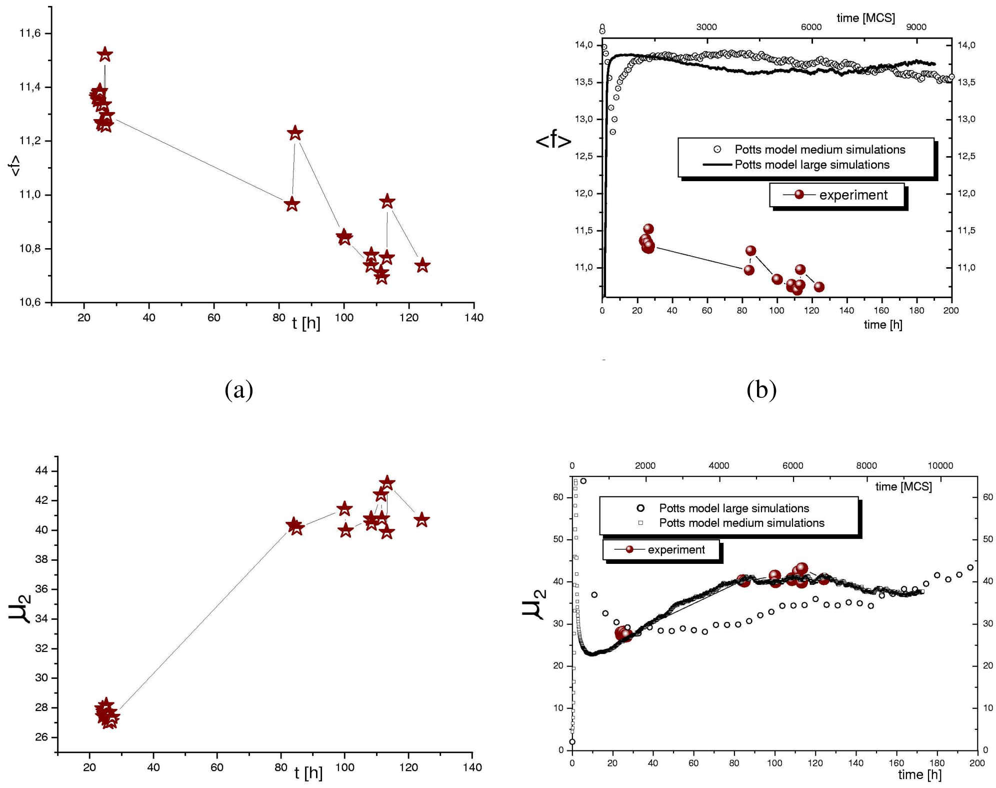

(a) (b)

(c) (d)

FIGURE 40. Evolution in time of the average number of faces (a) and its second order moment (c). In (b) and (d) for comparison the results of the Potts model simulations. The average number of faces is somewhat lower from the experiment, but the second moment $\mu_2 = \left\langle (f - \langle f \rangle)^2 \right\rangle$ may be fitted very well to the simulation.

with the scaling state simulations. Both, the experimental data and the simulation datasets are apriori represented in different timescales. These were adjusted so that the best agreement of the simulation and the second run data is achieved. The same time-scales are then applied in figure 40(b).

The mean number of faces can be approached from a slightly different perspective when plotted as a function of its second moments. Figure 41(a) captures the experimental datapoints for both runs in the case of the shaving foam. In 41(c) the same dataset is placed into the graphical representation of the trajectories for the Potts model simulations. The low average number of faces is again the most striking difference between the two datasets. The experimental values of the volume polydispersity in the $(\frac{\sigma_R}{R}, \mu_2)$ space is hown in figure 41(b). The time evolution of the topological polydispersity is represented in the last figure (42) of this chapter in which we addressed the evolution of two types of three-dimensional foams.

2.6. Discussion and outlook

. On the example of the rapidly evolving Dreft foam we could demonstrate the new possibilities

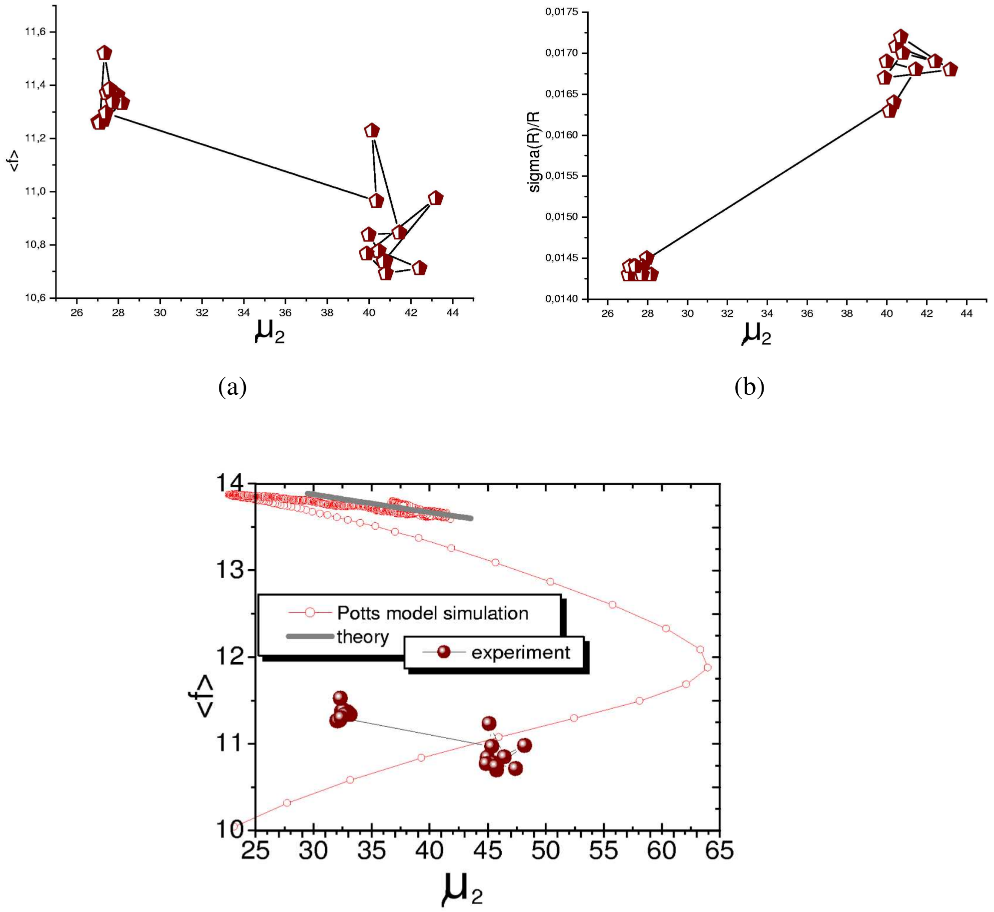

(a)

(b)

(c)

FIGURE 41. The trajectories in the $(\langle f \rangle, \mu_2$ plane (a) and in the $(\frac{\sigma_R}{R}, \mu_2)$ plane (b). As referred to in the simulations the first tend to stabilize in the region well visible in (c). There is no obvious correlation here between the experiment and simulations. In the same time it must be noted that the experimental distributions are stable but at different absolute values than for the simulations. This is due to the lower value for the mean number of faces in the experimental results as compared to the simulations.

of fast tomography as developed in Chapter 3. The Dreft foam provided results that were important for two reasons. Firstly to verify the feasibility of imaging a system inaccessible earlier due to its high rate of evolution. Secondly, these results have clearly demonstrated the behavior of the characteristic parameters in a regime that is far from the scaling state. Parameters like the average number of faces, or its second moment have not been presented for the fast evolving bubbling foam as they are very unstable during the whole period of observation, do not show any obvious tendency and in consequence are not significant for this particular type of liquid froth. The distributions of parameters belonging to the first (validation) category undergo a

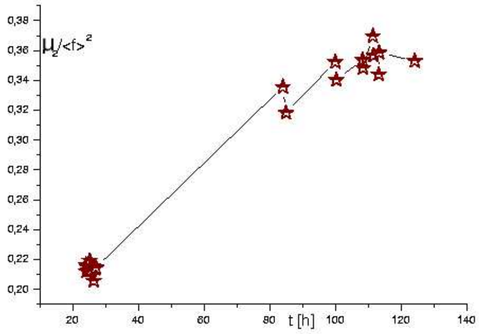

FIGURE 42. The time evolution of the topological polydispersity $\frac{\mu_2}{\langle f \rangle^2}$.

significant evolution during the period of observation. This change is perhaps even more significant than it was expected, especially for $\frac{\langle V_f \rangle}{\langle V \rangle}$ and $\frac{\langle S_f \rangle}{\langle S \rangle}$ which are presumed to stabilize rather rapidly.

The transition in this chapter from a young foam to the aged shaving foam is symbolic in the sense that it has been expected to be the step over a transition period towards the scaling state. The parameters in the validation category immediately showed a different behavior in comparison to those of the young froth. They were very stable and to a good approximation in accordance with the theory and the extensive Potts model simulations. These simulations that have been performed by Thomas et al (Thomas *et al.*, 2006). were used extensively in this work to serve as a guideline for what can be expected from various distributions in the 3D foam. The simulation results have been obtained simultaneously and independently from our experiment and they are complementary to experimental measurements discussed in this chapter.

After finding the topological quantifiers to be stable, a similar situation was found with the geometrical quantifiers $P(\frac{V}{<V>})$ and $P(\frac{S}{<S>})$. The stability of the shape of the distribution for the number of faces was also observed pointing out that all necessary conditions are fulfilled for the shaving foam to be in a regime close to the scaling state. The complementary parameters however do show more discrepancy with respect to the simulations and theory. This is not a surprise as the growth rate or the mean number of faces are very sensitive parameters. The main difference to the simulations is seen in the mean number of faces, that stabilizes around 11 for the shaving foam, while the Potts model simulations give a value of 13.7 and the simulations of Glazier 14.08. It seems that the second moment of the number of faces corresponds well to the simulations. Therefore we have tried to use this quantifier in order to attribute a particular state to our shaving foam as was shown in figure 40(d).

Finally as an outlook it must be noted that the experiment that resulted in the images used in this study has been performed only a relatively short time before this work is presented, therefore there are still many more interesting samples that have not been analyzed yet. For instance the Dreft foam (see 13) that is very dry at the late stages of its evolution is expected to give further important insight into the physics of dry foams. Preliminary results of this dry foam

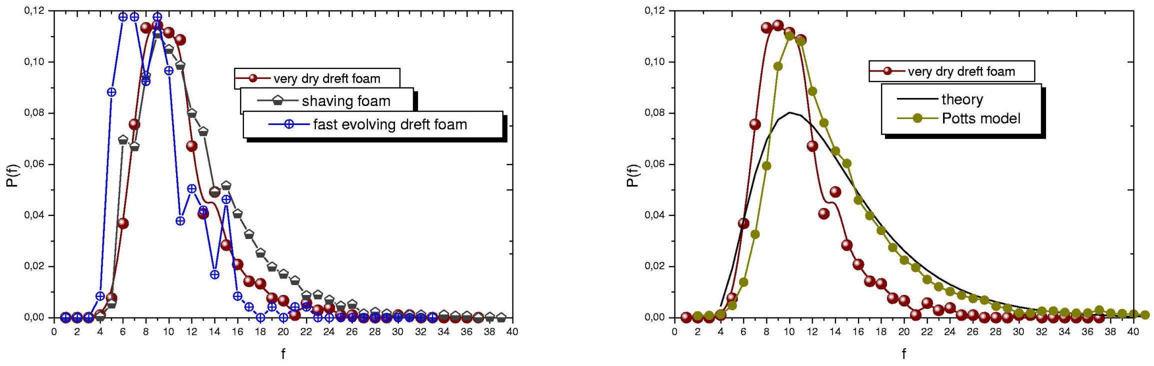

(a)

(b)

FIGURE 43. The distribution function of the number of faces for the three liquid foams with different characteristics (a). Here the P(f) for the fast bubbling foam is for time $t = 44$ min, for the shaving foam we took an average over the second run and for the dry dreft foam the $P(f)$ at $t = 20$ hours is shown. In (b) the comparison of the same distribution of the dry Dreft foam to the Potts model simulations and the theory shows the same shift towards lower number of faces as it was evident in the case of the bubbling foam and the shaving foam as well.

are encouraging partly also because it is rather difficult to achieve correct labeling for this type of samples as it has been addressed in this chapter. The distribution function of the number of faces for the dry Dreft foam and the two more extensively discussed foams is plotted in figure 43(a). The theory and the simulations assumes dry foams, hence it is of interest to compare the profile of such a very dry foam to the theoretical one (figure 43(b)).

CHAPTER 5

The road to projection x-ray tomography

1. The advantages of a focused over a parallel beam

It follows from the data presented in section 2.1 that the divergence of the x-ray beam emerging from a synchrotron source is extremely low. As a consequence we speak about parallel beam imaging in contrary to laboratory x-ray experiments where by the nature of its generation the fan- or cone-beam geometry is usually the case. The parallel beam has many advantages for tomography, such as easy and artifact free reconstruction. The high brilliance of the source also results in a much higher number of useful photons at the level of the detector. The beam angular divergence at the ESRF is $10 - 200\,\mu$rad demonstrating the important difference in this value when looking at a typical laboratory source divergence which emits over half space. The divergence of the latter must not necessarily facilitate the imaging with x-rays but certainly can be attributed at least one important advantage - the magnification - the pillar of the idea of projection imaging with divergent x-rays.

The improvement of the spatial resolution triggered by a broad spectrum of industrial and biological applications is certainly one main driving force towards new designs and techniques in todays' imaging technologies. This is particularly true for techniques that provide 3D information about a sample in a nondestructive manner. X-ray tomography is the oldest among them and yet still evolving. Changing the parallel geometry of a synchrotron beam in order to take advantage of both the geometric magnification and high monochromatic flux appears to be a very promising direction towards nano-imaging. Using Fresnel zone plates as objective lens and keeping the x-ray energy below 7 keV has brought resolutions of about 100 nm (Neuhausler *et al.*, 2003; Youn and Jung, 2005). One step forward is to combine x-ray microscopy with tomography to access the bulk properties of materials at similar precision using highly penetrating hard x-ray radiation (Mayo *et al.*, 2003; Schroer *et al.*, 2004).

In the parallel beam geometry, usual for micro-tomography at synchrotron radiation facilities, the spatial resolution is essentially determined by that of the high resolution detector. The best optics do not provide resolutions significantly better than a micron (FWHM of the point-spread-function for the $0.28\,\mu m$ optics used at ESRF, has been measured to be approximately $0.8\,\mu m$ in the best case). The x-ray/visible light conversion scheme furthermore results in poor efficiency at high resolution due to the thin conversion screen required. No drastic improvement in spatial resolution of these devices can be expected. Therefore one has to consider other directions like chaning the geometry of the imaging system. Bent graded multilayers set in the Kirkpatrick-Baez (KB) geometry allow to focus undulator radiation to spots below 90 nm (Hignette *et al.*, 2005) and preserve a very high quasi-monochromatic flux (5 10^{11} photons/s with a medium monochromaticity, $\Delta E/E \approx 10^{-2}$). A line focus of approximately 40 nm was reported (see figure 4) and further progress can be expected. Furthermore improvement of spatial resolution does not necessarily imply a reduced efficiency as it is the case for the high resolution detectors or Fresnel zone plates.

The principal advantage of using a divergent beam at the synchrotron source is the possibility to overcome the spatial resolution limit set by the detection system. Simply by placing the sample in the divergent beam and modifying its relative distance to focal plane and to the detector we take advantage of the geometrical magnification likewise for laboratory tomographs, but with the major difference in beam properties. Beside the high flux, the synchrotron beam is partially coherent and also offers the possibility to tune the wavelength. A $125\,\mu m$ aluminum wire was used on figure 1 to demonstrate the magnifying effect on images taken with divergent beam. The images of the wire also contain phase contrast which beside the magnification is an important property of the imaging system described in this chapter.

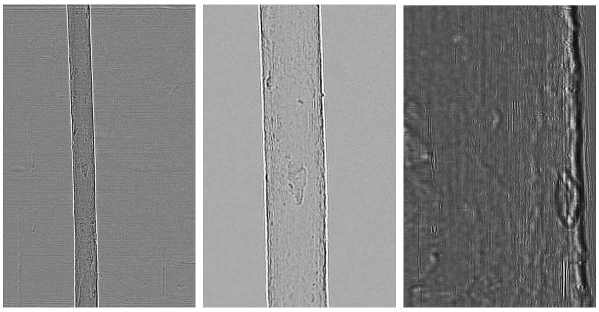

(a) (b) (c)

FIGURE 1. Radiographs of a $125\,\mu m$ aluminum wire placed in the divergent x-ray beam produced by KB optics at 3 different distances z_s from the focal plane which by keeping the detector to focus distance z_d constant results in magnifications of $M = \{18(a), 46(b), 278(c)\}$). At the highest magnification only one edge is imaged since the field of view is smaller than the diameter of the wire.

2. Focusing x-ray optics

A divergent beam or a spherical wave can be produced at a synchrotron source by introducing a focusing optics. In spite of the difficulties imposed by the almost unity value of the refractive index for x-rays, the quick developments in micro-fabrication techniques and surface figuring in the last decades brought several important X-ray optics components to real use.

Intheh late 1980s an original idea of controlling the beams of neutral particles, x-rays, and neutrons was proposed by Chumakov. Founded on using multiple reflection and special geometry of reflecting surfaces inside hollow glass capillaries, the idea was patented by Chumakov in 1984. The first x-ray capillary lens was created in his laboratory at the Kurchatov Institute of Atomic Energy in 1985, and the first neutron lens in 1987. Chumakov type lenses can today provide focal spot sizes as small as several micrometers.

Compound refractive lenses (Snigirev *et al.*, 1996) are similar to ordinary lenses for visible light. Such lenses are relatively simple to produce and work well for harder x-rays. The theory of the ideal compound refractive lens was elaborated for example by Protopopov in 1998 (Protopopov and Valiev, 1998) and more specifically by Kohn (Kohn, 2003). For longer wavelengths, however, gain in the focus decreases due to absorption in the lens material. The most recent study of the best achievable focal spot size using adiabatically focusing refractive lenses claims that in theory values below 10 nm for hard x-ray energies (Schroer and Lengeler, 2005) should be possible. In practice the numerical aperture of these lenses, and consequently the opening angle of beam is (too) small.

An alternative focusing method based on refraction was proposed by Hrdý (Hrdy, 1998). He proposed to use the diffractive-refractive effect, which is the refraction phenomenon occurring during Bragg diffraction. It was shown theoretically (Hrdy, 1998) and experimentally (Hrdy and Siddons, 1999) that x-rays that are diffracted from a parabolic longitudinal groove machined into a single-crystal monochromator are sagittally focused and hence a crystal may be used as focusing device.

Fresnel zone plates (FZP) have become an elegant way of x-ray focusing. However, the current limit in precision of their fabrication imposes strong increase of the spot size and decrease of their efficiency with shorter x-ray wavelengths. This limits their application mainly to lower energies ($E < 10\,keV$). The simplest type of FZP is an amplitude plate composed of zones alternately transparent and opaque to X-rays. In this case the focusing originates mainly from the relatively different absorption of neighboring zones. The efficiency can be considerably improved using Fresnel phase zone plate which focuses x-rays through the relative phase change between neighboring zones. The Fresnel phase zone plates can be realized choosing an appropriate material with a thickness such that the phase retardation $\Delta\varphi$ of the incident wave is π in those zones that are opaque in the amplitude FZP. Fone plates are chromatic which limits the flexibility of the system based on this type of focusing. The best focus achieved recently with a tantalum Fresnel zone plate fabricated by electron beam lithography approaches $50\,nm$ for $8\,keV$ x-ray energy (Suzuki *et al.*, 2005).

Also recently reported is a new type of linear zone plate which is produced by sectioning a multilayer and illuminating it in Laue geometry (Kang *et al.*, 2006). At a photon energy of 19.5 keV the multilayer Laue lens gave a one dimensional focus with FWHM as small as 30 nm by the efficiency of 44%.

In practice it is often difficult to achieve sufficiently high structures that would result in a π phase shift, especially for narrow zones. A solution to this problem consists in working in reflection instead of transmission geometry. This situation can be obtained using the Bragg diffraction of a perfect crystal on which a Fresnel zone plate is grown. This is what a Bragg-Fresnel lens (BFL) achieves (Aristov *et al.*, 1986). The wave diffracted at a Bragg angle by the lower surface of the BFL zone structure gains an additional phase shift as compared to that reflected by the upper surface. The height of the relief has to be adjusted in order to have a π phase shift, but it is reduced compared to the transmission geometry. On the similar principle a new 2D focusing X-ray lens was developed (Li *et al.*, 2003; Erko, 1990) by combining a linear thin-film Fresnel lens and a multilayer mirror. In the multilayer Bragg-Fresnel lens (MBFL), the Fresnel zones focus the X-ray beam vertically by diffraction, whereas the multilayer mirror is bent to focus X-rays horizontally. This unique combination eliminates the need for a second mirror in conventional Kirkpatrick-Baez mirror-based microprobes. The spot size achieved is approximately $2\,\mu m$ (vertical) x $12\,\mu m$ (horizontal) from an incident beam size of $250\,\mu m$ (V) x $200\,\mu m$(H).

An alternative to focusing hard x-rays providing coherent beams with very small lateral dimensions are waveguides (Pfeiffer *et al.*, 2002). X-ray waveguide structures consist of a low density guiding layer sandwiched in between layers of higher density. The beam size at the exit can be as small as a few tens of nanometers. The geometric acceptance of an x-ray waveguide is much smaller than the typical beam size at present synchrotron radiation beamlines, therefore the beam is typically coupled into the guide from the top rather than from the front. The low coupling efficiency may be compensated to some extent by modifying the coupling geometry and prefocusing the beam with a high gain system such as the Kirkpatrick-Baez optics (Jarre *et al.*, 2005).

In a way, the simplest focusing technique is based on using the grazing incidence of x-rays to fabricate mirrors that reflect the beam and, by imposing a particular curvature, also focus it at the same time. But, the critical grazing angle of reflectivity decreases linearly as the energy increases for ordinary metal surfaces which has an adverse impact on the design of a focusing system for higher energy x-rays. As a consequence the projected area of an individual mirror element is decreased and so is the field of view (FOV) together with the latter the focal length for a fixed diameter system is increased. To compensate, mirrors coated with multilayers have been designed. It is theoretically possible to increase the incidence angle by coating the mirror surface with a multilayer such that closest to the vacuum strong reflection occurs for particular Bragg angles . The ability to produce a coated mirror with close to theoretical performance is, however, technically challenging. The development of multi-layer coated mirrors was started in the early 80s. The limiting fabrication factor was the precise control of thickness of each layer. An impressive innovation in the form of graded multilayer first appeared in space telescopes and later fabricated for x-ray imaging (Morawe *et al.*, 2003). Its particularity being the varying period on the parabolic substrate so that only a small band width can be diffracted; the system stays in Bragg condition while the angle of incidence varies due to the curvature of the mirror. One mirror essentially focuses the beam in the plane containing the surface normal. For two dimensional focusing two mirrors have to be used in crossed geometry as first described by Kirkpatrick and Baez in 1948 (Kirkpatrick and Baez, 1948). These instruments are used for different applications at synchrotron sources and there is an obvious progress in their performance (Iida and Hirano, 1996; Ablett *et al.*, 2002). The imaging with such a Kirkpatrick-Baez focusing system is described in (Mokso *et al.*, 2006)

Among the most recent achievements we can mention the focused beam down to $36\,nm$ FWHM reported from the $1\,km$ long Spring-8 beamline (Yumoto *et al.*, 2005). This diffraction limited spot size was achieved at $15\,keV$ with mirrors elliptically shaped by computer-controlled plasma chemical vapor deposition and elastic emission machining techniques.

The above list is by no means complete, no mention was for instance made of specific focusing optics for Astronomy such as wide angle (Lobster eye) optics (Hudec *et al.*, 2004; Pina *et al.*, 2000). After this short overview we shall now turn towards reflective optics and multilayers since this is the optics we used for the projection imaging.

3. The Kirkpatrick-Baez focusing system

3.1. Instrument description

. Choosing the focusing optics for x-rays is a question to outweight the drawbacks of the chosen system by its best applicability to selected applications. The tideous alignment of a KB system was here considered to be a minor drawback compared to the advantages that the Platinum coated mirrors or multilayers in such arrangement offer. These advantages will be listed next.

Aimed for hard x-rays, the efficiency of reflective optics or multilayer does not deviate far from unity, and even in the configuration with two reflections (horizontal and vertical mirror) it is possible to have scanning times much shorter than it would be feasable with other type of x-ray focusing optics.

The high photon flux at the exit is further ensured by working without additional monochromator upstream of the KB optics. The monochromacity of the beam is determined by the width of the undulator harmonic used and the bandwidth of the multilayer coating the first mirror. This is justified since the reflective and multilayer coated optics are not energy dispersive unlike diffractive or refractive optics.

The achromacity makes it possible to scan with fixed mirror geometry over a certain energy range around the maximum of the multilayer efficiency or till the critical angle is too small resulting in low reflectivity. The latter is crucial for spectroscopy experiments with high precision 2D mapping of the sample.

It must not be omitted in this introduction that a more severe inconveniency for tomography is related to the figure errors of the mirrors and other imperfections of their surface (further details are given in section 4). Moreover, the thermal stability needs to be addressed (in section 3.3).

In the current tomography setup as sketched on figure 2 (a) the sample is set at a small distance ($20 - 300$ mm) downstream of the focal plane and a magnified Fresnel diffraction pattern is recorded on a medium resolution detector set at a large distance (several meters) from the focus. Figure 2 (b) is the photograph of the instrument that has been used at ID19 (Hignette *et al.*, 2001) for the experiments discussed below. The two mirrors in crossed geometry (Kirkpatrick and Baez, 1948) serve as two-dimensionally focusing optics. In the focal plane we obtain ideally a de-magnified image of the source. To achieve a focused image it is necessary to satisfy

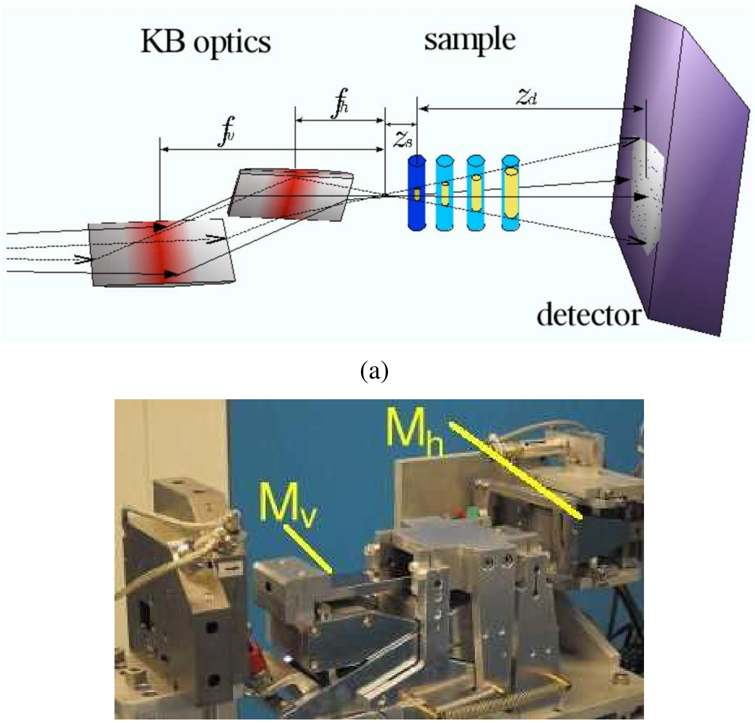

(a)

(b)

FIGURE 2. (a) Principle drawing of the imaging system with the two mirrors in cross geometry. The sample represented by the cylinders can be placed at various defocus positions. This in turn modifies the field of view as highlighted with the yellow cylinder. A side view photo (b) of the Kirkpatrick-Baez mirror system at ID19 shows the two optical elements in the beam which are the mirrors and the precise slits at the entrance of the beam (to the left in the image).

the lens equations at the center of the first ($m = v$) and second ($m = h$) mirror:

$$\frac{1}{p_m} + \frac{1}{q_m} = \frac{2}{R_m sin\theta_m};\ m = \{h, v\} \tag{81}$$

where p_m and q_m are respectively the source-to-mirror center and mirror center-to-focal plane distances, R_v and R_h are the radii of curvature of the mirrors at their center and θ_m the angle of incidence on each mirror. The ratio of the focus and source size equals the ratio of their relative distances from the mirror system q_m/p_m. The source at ID19 is at a distance of $145\,m$ and will allow to achieve very strong de-magnifications. The vertically focusing mirror M_v has a focal distance $q_v = 280\,mm$ while the horizontally focusing one M_h projects the source to a distance $q_h = 95\,mm$. The source size (FWHM) at this low β section is $s_h = 135\,\mu m$ and $s_v = 25\,\mu m$ in horizontal and vertical direction respectively, resulting in an ideal de-magnified source image of $sd_h = 88\,nm$ and $sd_v = 48\,nm$. In reality, the contribution to the focal spot size is more complex as the mirrors have a finite length. For extended mirrors the ideal shape is a portion of an ellipse with the source located in one ellipse's focus and the formed spot in the other ellipse's focus. In our case ($p_m \ll q_m$) the ideal ellipse is nearly a parabola. The vertically focusing first optical element of the KB, M_v is coated with a graded multilayer (each of the

30 W/B_4C layers has a central thickness of $4.7\,nm$ varying along the lengths of the mirror with a 33% gradient) which acts as monochromator and increases the acceptance angle of the system, a crucial parameter in imaging. The angle of incidence on the Pt coated horizontally focusing mirror is 2.8 mrad whereas it is 7 mrad on the vertical optics at an x-ray energy of 20.5 keV. The opening angles of the cone beam are 2 mrad and 3.5 mrad in respectively the horizontal and vertical direction. The acceptance in the horizontal direction is $\simeq$200 μm but $\simeq$ 1 mm in vertical direction thanks to the multilayer coating of the vertically focusing mirror.

The mirrors leaving the fabrication process are flat and theyare mechanically bent to the desired elliptical shape (Hignette *et al.*, 1998). To approximate the required ellipse, moments are applied at both ends of a substrate clamped on a mechanical bender based on flexure hinges. The mirrors are pre-bent in the metrology laboratory and the final shape is given at the beamline. The bending to the correct shape at the beamline is done with an alignment algorithm derived from adaptive optics techniques. An x-ray camera is positioned in the plane where one wants to focus the x-rays. A frame is acquired which is a coarse image of the focal spot. The resolution of the x-ray camera does not allow to measure the size of the spot, but its position can be determined very precisely. The exact position of the spot can be measured by its center of gravity, but this method is way too coarse for our needs. Therefore we employ an inter-correlation method implemented at ESRF (Hignette *et al.*, 1998) consisting of a parabolic regression on the cross-correlation of the profile and its mirror. Provided that the precise slits upstream the first mirror are closed in one direction to form a very narrow beam (typically 20 μm) they define the region where this line beam hits the mirror. Sending a small displacement on them will displace this region and by acquiring the next image we can step by step identify the shape of the mirror or actually the angular errors with respect to the ideal shape. If the mirror is correctly bent all rays will arrive at the same position. The bending system of each mirror is equipped with two actuators (picomotors). To characterize the system, small displacements of the actuators are applied and the response of the system is measured by scanning the slit. The interaction matrix H of the bending system is thus built in this way and the correction vector $C = (H^T H)^{-1} H^T Y$ can be sent to the actuators. The whole procedure is performed on both mirrors separately. It is found to converge after a few iterations but the system can only be optimized over a limited range of the mirror as two actuators allow only to correct up to a second order polynomial in the angular errors and a 3rd order polynomial in the mirror shape. A 4th order polynomial error will be present in the mirror shape. To compensate for this to some extend a linear variation of the substrate width is necessary. In this case, calculations show that the maximum slope error with respect to the stigmatic ellipse could be less than 0.4 μrad rms in the energy domain $7 - 30$ keV and the system would essentially be limited by the polishing errors of the substrate. However practically it was found to be true only for the central part of the mirror.

The focusing system is mounted on a light but very rigid frame optical table (figure 3(a)) equipped with air pads ensuring the natural vibration frequency of 90 Hz. This is an important point for a system that was not permanently mounted on the beamline and had to be displaced before each experiment. Integrated on the same table is the sample stage as well (figure 3(b)).

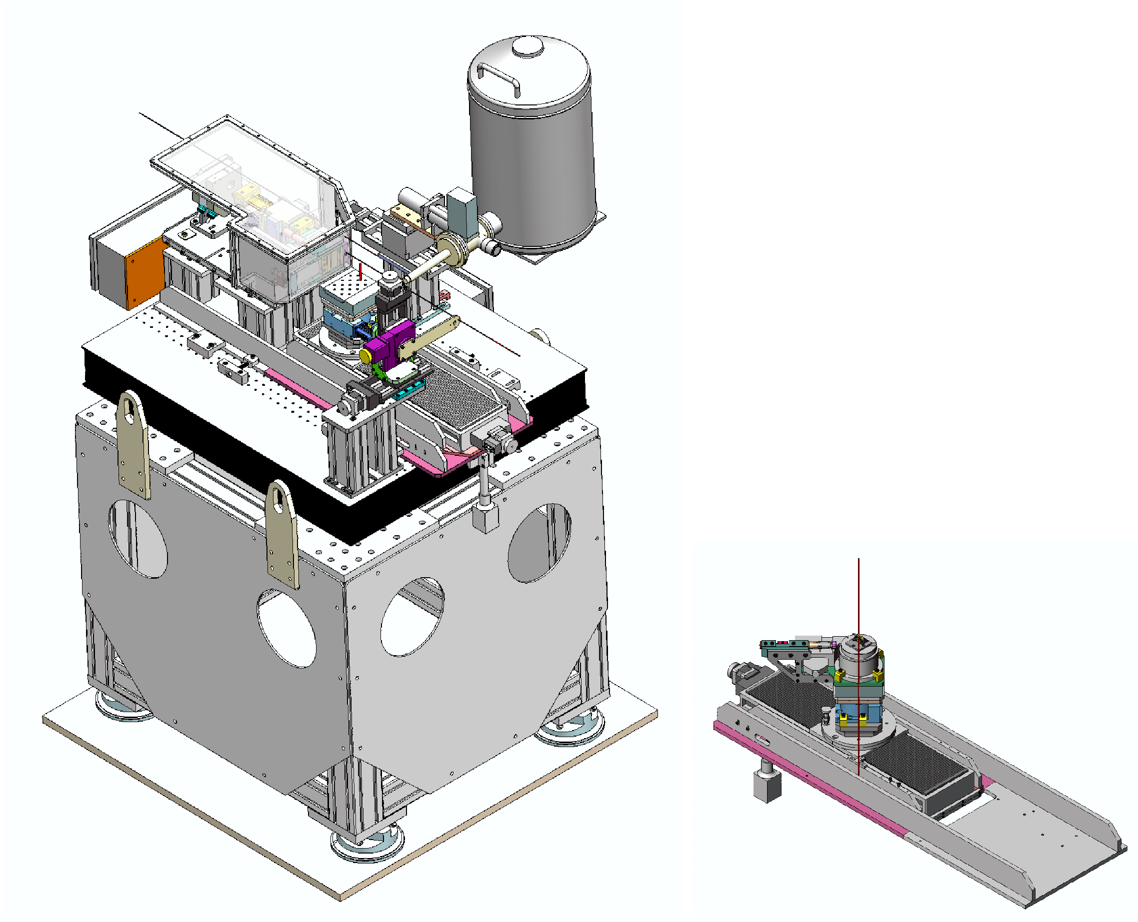

(a) (b)

FIGURE 3. A drawing of the complete KB system (a) placed on the light optical table with air-pads. The mirrors are in the plexi-glass box to protect from dust and aid thermalization. The nitrogen container of the energy dispersive detector for fluorescence is also visible on the drawing. Mounted on the corner of the table is the arm with two translations and a rotation serving as the holder of the grid that can be used during the experiment to measure the beam properties. The separate image of the sample stage (b) shows the long translation on which the elevation stage and the precise translation perpendicular to the beam direction is placed with the pusher and rotation stage on top. The long translation can be tilted to be parallel to the KB reflected beam and to ensure the perpendicularity of the rotation axis with respect to the new beam direction.

The entire sample stage is placed on a $300\,mm$ long translation (OWIS). The choice of the range of this translation in the direction of the incident beam was based on the possibility to have a sufficiently large room for the focus-to-sample distance variation, thereupon to vary defocus for phase retrieval as well as the magnification of the imaging system. This translation carries a $15\,mm$ elevation stage (HUBER) and a precise linear stage (NEWPORT) for moving the rotation/sample in and out of the beam. Mounted on top of these stages are the rotation stage and the 'pusher' designed at ESRF (P. Bernard). The pusher is basically a fine positioner bringing the sample on the rotation axis. For this purpose the sample is sitting on a plate magnetically connected to the rotation stage and keeping contact with it only through three steel balls. By turning the rotation we select the direction in which the pusher executes the sample gliding. This approach replaces conveniently two perpendicularly mounted translations which would increase the height of the whole sample tower and induce parasitic movements due to the cabling. Finally the upmost important piece of the sample tower is the rotation stage. A Newport RV80 rotary stage has been selected to fulfill as closely as possible the numerous criteria. The product specifications given by the manufacturer include the typical values for uni-directional repeatability of $0.0002°$, wobble $16\,\mu rad$ and eccentricity $1.4\,\mu m$. The values measured in the precision metrology laboratory at ESRF are as follows: typical wobble $16-20\,\mu rad$ measured on two bidirectional full rotations and eccentricity $1\,\mu m$ measured at $73\,mm$ from the top face of the stage on two bidirectional full rotations. These values are important to keep in mind when interpreting the tomographic scans and the possible parasitic movements of the sample due to the mechanics of the sample stage. We perform the tomography with a rotation over a half turn ($180°$) and with the sample as close as possible to the top face of the rotation ($\simeq 15$ mm) hence the measured eccentricity value is expected to overestimate the actual errors .

3.2. Spot size measurement

. In (Hignette *et al.*, 2005) we find a focal spot size measurement for the system introduced above. The FWHM of the approximately Gaussian profiles of the vertical and horizontal focus were $86\,nm$ and $83\,nm$ respectively. The measurement was performed with a fluorescence scan of a $38\,nm$ high, $5\,\mu m$ wide, golden stripe deposited on a polished vitreous carbon substrate. The small incidence angle (< 10 mrad) allows a reasonable width and efficiency of the stripe without affecting the spot measurement. The measurement provides directly a line scan of the spot. This approach is preferable to the more usual knife edge scan, where the derivation process always introduces significant errors. The spot measurements were repeated after modifications which were aimed to improve the thermal stability of the system. We observed a slight increase in the size of the focal spot probably due to vibrations the building of ID19 being exposed to strong wind during the experiments. The best reproducible result we could measure was of the order of $110\,nm$ in both directions.

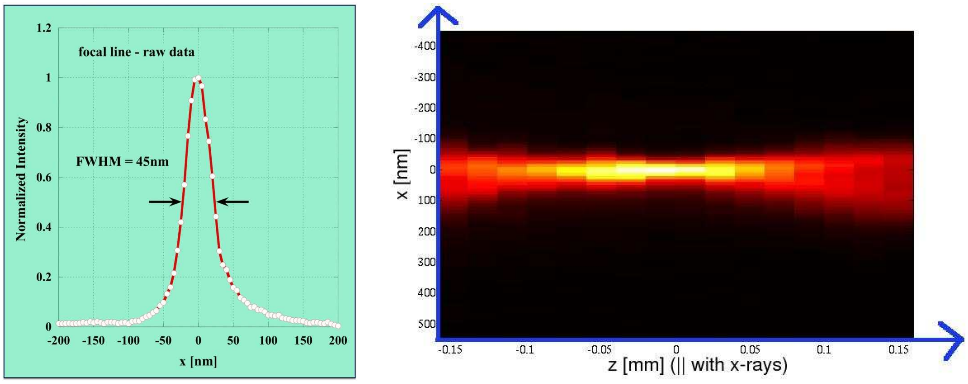

(a) (b)

FIGURE 4. The fluorescence profile of the scan through the focal plane using a 17 nm high nano-stripe deposited on a carbon substrate. Figure (b) represents the scans through the beam for various z values (to find the best real focus).

Recently a new multilayer coated mirror has been tested. We measured the one-dimensional focal spot size in the vertical direction at 24 keV beam energy. A scan of the fluorescence signal through the focal plane is shown in figure 4(a). The full width of the raw data is 45 nm. After deconvolution for the finite effective width of the nano-stripe, the full width at half maximum reduces to $41\,nm$. This value is practically the diffraction limited spot size for the $130\,\mu$m entrance acceptance used during the experiment.

3.3. Thermal stability

. If we don't take into account some random events (such as running in biking shoes down the stairs above the experimental hutch) the stability of the focal spot is mainly influenced by the temperature variations of the whole system. These variations induce both, changes in focal distance, and changes in lateral position of the focal spot. On figure 5 we illustrate this observation in terms of the focal plane to exit mirror distance and the recorded temperature of the experimental hutch. By plotting the horizontal (or vertical) focal distance position as a function of the temperarure (figure 5(b)) a linear relationship is observed.

	vertical focus (1st mirror)	horizontal focus (2nd mirror)
perpendicular to beam propagation direction	14 μm/K (25 μrad/K)	2.4 μm/K (-12.6 μrad/K)
in-beam direction	-2850 μm/K	-1330 μm/K
reaction on the KB temperature increase	angle increases	angle decreases

TABLE 1. Basic characteristics of the thermal response ofthe KB system in terms of mirror shape or angle variation as obtained from the measurements.

Already this long term stability measurement implies the need to employ a precise temperature regulation. To give this problem a more quantitative character a plot of vertical focus displacement versus mirror temperature is presented in figure 6. From here follows that in order

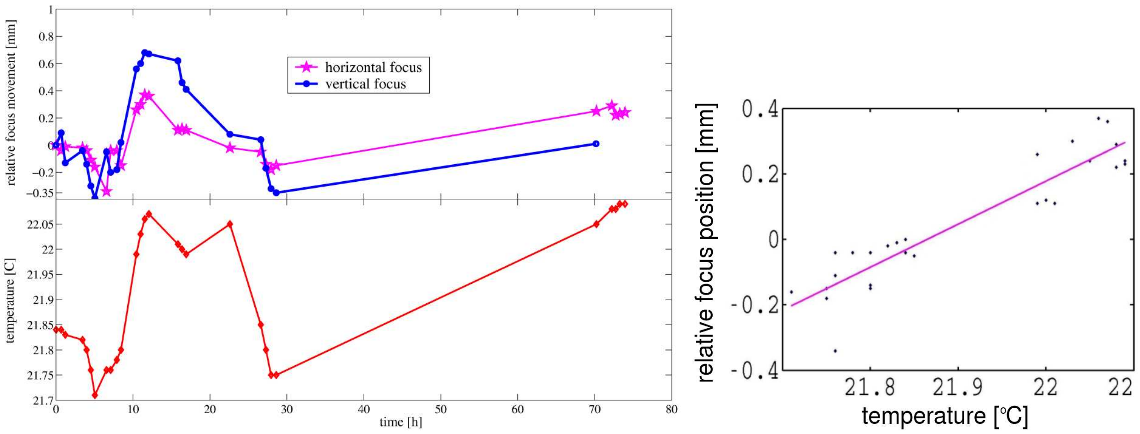

(a) (b)

FIGURE 5. In (a) the changes in focal distance along the beam direction obtained from grid images are presented in the upper figure as a function of time, the lower is the hutch temperature during the measurement. In (b) the relative position of the horizontal focal plane as function of temperature and its linear fit.

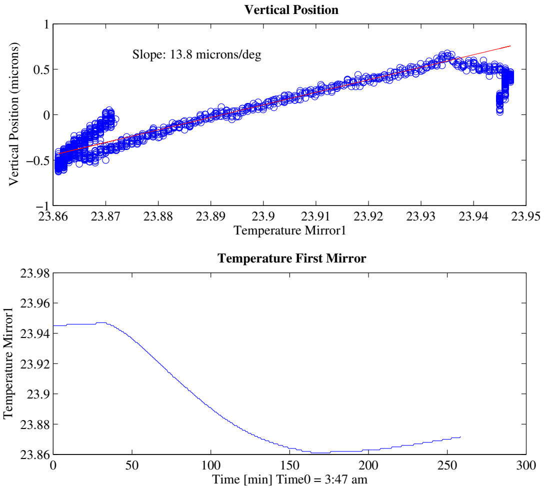

FIGURE 6. Top: Vertical position of the focus as a function of the mirror temperature. Botton: temperature as a function of time.

to obtain a reasonable (of the order of the focal spot dimensions) focal spot stability we would have to keep the temperature deviation of the system in the range of a few mK.

From the tests we have performed it was possible to summarize the thermal characteristics of the KB system in table 1. The movements in the lateral direction are most likely due to changes in the angle of mirror and can be expressed as $2.\Delta\theta_m.p_m$. The corresponding angular changes are $25\,\mu$rad/K and $-12.6\,\mu$rad/K in respectively the vertical and horizontal direction. The in-beam movement or change in focal distance can be caused by change in angle, change in curvature or a combination of both. From expression 81 we have

$$\frac{\Delta q}{q} \simeq \frac{\Delta \theta}{\theta} + \frac{\Delta R}{R} = \frac{\Delta \theta}{\theta} + \frac{\Delta (1/R)}{(1/R)} \tag{82}$$

with $1/R$ the mirror curvature, $\theta_v = 7mrad$, $\theta_h = 2.8mrad$, $q_v = 280mm$ and $q_h = 90mm$. It can be clearly seen that the main contribution to the change in focal distance is due to the changes in curvature for which we find relative values of 0.014 and 0.01 in respectively the horizontal and vertical direction. In terms of mechanical deformation of the bender arms this indicating that when the temperature increases, the bender arms dilate in such a way that the mirror curvature increases. This is attributed to the much higher thermal dilatation of steel, the principal material of the bends, as compared to the silicon of the mirror. Simulations of material dilatation by means of finite elements methods done by L. Zhang from the ESRF optics group seem to be in agreement with our measurements. The thermal dilatation coefficient, α_{steel} of steel is 17×10^{-6} while that of the Silicon mirror $\alpha_{Si} = 2.6 \times 10^{-6}$. Since the change in mirror curvature can be expressed in terms of the thermal dilatation coefficients and the gradient of temperature as $\frac{\Delta(1/R)}{1/R} = c.\left(\alpha_{bender} - \alpha_{mirror}\right)\Delta T$, the choice is obvious for how to reduce the sensitivity of the system to thermal effects. The new INVAR ($\alpha_{INVAR} = 3 \times 10^{-6}$) benders were installed to decrease the temperature sensitivity of the KB assembly.

While simulations and experiment agree in the way the mirror curvature is affected by the temperature, another source of focal spot drift has to be identified. As seen from images directly on the imaging camera and long term measurements of the focus position with the KB alignment camera, the angle of the mirror does change as well. Since the KB construction is symmetric (except of the linear gradient in the width of the mirror substrate), no obvious reason for this angular drift was found.

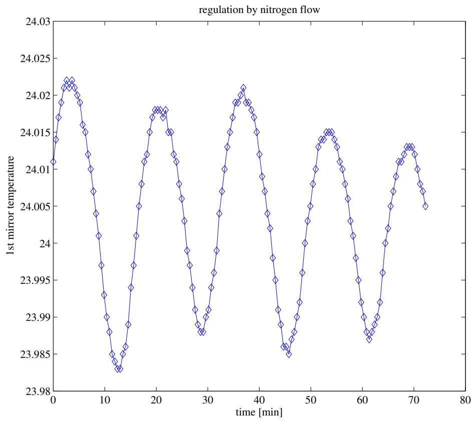

FIGURE 7. Regulation of the mirror temperature by nitrogen flow. The graph shows the temperature at the vertically focusing mirror where a feedback thermal sensor is placed. The amplitude of the temperature oscillations is of the order that we aim for. The short response time ($\sim$ 15 minutes) of the system is characteristic for this kind of temperature regulation but the oscillations are destabilizing the system.

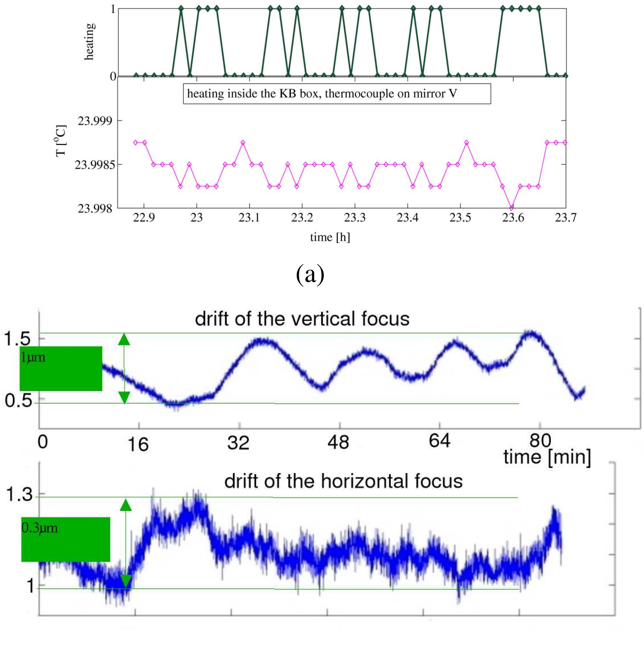

(a)

(b)

FIGURE 8. Regulation taking the mirror temperature as reference. The vertical focusing mirror temperature deviation is less than 2mK as presented in time domain (a) but periodic displacement of the focal spot perpendicular to the x-ray beam propagation direction is still observed in (b).

To achieve better stability we have gradually modified selected elements of the KB configuration and tried different temperature regulation schemes. The first step was to implement a straight-forward temperature control by regulating the temperature of the nitrogen blown into the KB box, Doing so by letting it pass through heat regulated porous media. Although the nitrogen regulation was precise to 2 mK (see figure 7), in long term the whole system still followed the temperature of the hutch. In addition the undesired destabilizing effect of the abrupt changes in entering gas temperature has been observed.

In the next step, heating elements were installed inside the box as well as 5 thermocouples each of them placed to a carefully selected element of the KB mechanics. Most of them served only as indicators, one of them located on the lateral face of the first mirror, provided feedback for the regulation of power to the heating elements. Figure 8 demonstrates that despite of the successful effort to keep the mirror temperature constant within ± 1 mK, the switching on and off the heater results in focal spot instabilities of $\approx 1\,\mu m$ and $\approx 0.2\,\mu m$ for vertical and horizontal focus respectively. Taking the thermocouple on the base plate as feedback element yields similar results. We attribute these instabilities to thermal gradients in the system.

As the most soffisticated temperature regulation scheme, we have tested the regulation by Peltier elements. In figure 9 the response of the system to an abrupt temperature change is demonstrated. The regulation was done with Peltier elements mounted on the support of the mirrors. They heat or cools the system in order to hold it at a temperature set by an external unit. Different elements of the KB have different responses to this heating or cooling and it

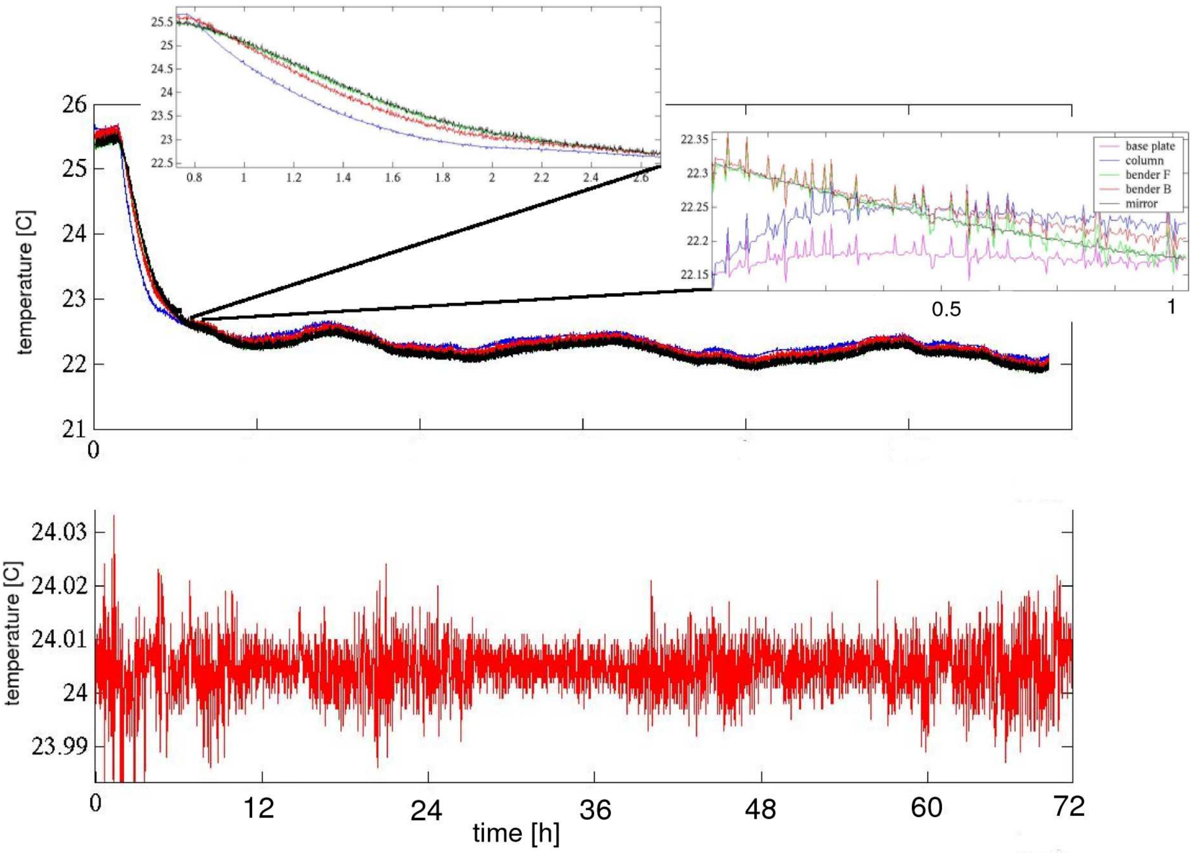

FIGURE 9. The response of the system to an abrupt temperature change. Top: The complete set of thermocouples is monitored during a period of 72 hours. Zoom at two regions is in the upper figures. The bottom most plot is the temperature of the nitrogen gas blown in the box of the KB (The gas temperature stabilizes within minutes and remains stable for the whole period of measurement).

was important to understand this in detail. Finally the long term stability was improved by regulating the temperature with the little heat produced by the holding current of the slits inside the KB box.

Although the thermalization of the KB system at ID19 has proved to be beyond the possibilities of the current beamline dispositive, the work performed had significant impact on projecting the new experimental station for nano-imaging where a KB system is installed. Many aspects of the thermalization needs were understood during the above study, one of the most important being the insufficiency of regulation by convection inside the KB housing. Also the various ways of thermally isolating the KB box does not represent an efficient solution and can not be expected to be robust to significant changes in the surrounding temperature. Therefore it is important to have a rather global view when installing systems with extreme stability requirements and start by assuring a reasonable thermalization of the experimental hutch.

We have not yet considered the thermal contribution of the incident x-ray beam. The power deposited when part of the x-rays are absorbed by the first mirror causes a small increase in mirror temperature. Four consecutive tomographic scans induce the sawtooth-like temperature profile shown in figure 10.

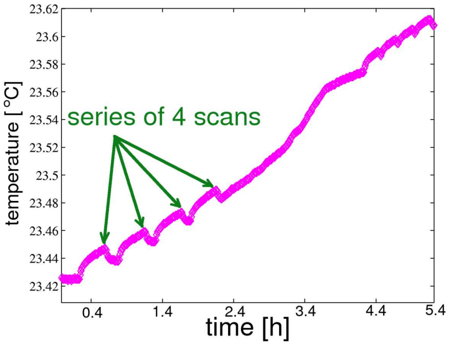

FIGURE 10. The incident x-rays are partially absorbed by the mirror. The energy deposited this way is mostly dissipated in heat as observed in this figure, since the four consecutive sawtooth features in the temperature plot correspond to the four scans of the holotomographic procedure.

The temperature of the mirror varies by typically 10 mK when the incoming beam (in 16 bunch injection mode) hits the mirror surface. This has for the moment a minor effect compared to the temperature changes due to the drift of the hutch temperature.

4. Magnification for tomography

The focusing device provides a spherical wave illumination of the sample. Referring to figure 2(a) for the wave-field in one dimension at the detector in the abberations free case, we can write:

$$u(x) = \frac{1}{z_S\sqrt{i\lambda z_d}} \int e^{i\frac{\pi}{\lambda z_s}\xi^2} T(\xi) e^{i\frac{\pi}{\lambda z_d}(x-\xi)^2} d\xi \tag{83}$$

here x is is the coordinate in the plane of the detector, z_s and z_d are the the sample-to-focal-plane and sample-to-detector distance as marked in figure 2(a). After straight-forward rearrangements in the integral we have

$$u(x) = \frac{1}{\sqrt{\lambda z_s}} e^{\frac{i\pi}{\lambda}\frac{x^2}{z_s+z_d}} \int e^{i\frac{\pi}{\lambda}\frac{z_s+z_d}{z_s z_d}(\xi-\frac{z_s}{z_s+z_d}x)^2} T(\xi) d\xi \tag{84}$$

We can introduce at this point the effective defocus distance D and the magnification M as

$$D = \frac{z_s.z_d}{z_s+z_d} \quad \text{and} \quad M = \frac{z_s+z_d}{z_s}. \tag{85}$$

and rewrite formula 84 as

$$u(x) = \frac{1}{\sqrt{\lambda z_s}} e^{\frac{i\pi}{\lambda}\frac{x^2}{z_s+z_d}} \int e^{i\frac{\pi}{\lambda D}(\xi-\frac{x}{M})^2} T(\xi) d\xi \tag{86}$$

From here it is seen that the divergent geometry is equivalent to a plane wave illumination with the equivalent defocusing distance D and the magnification M. In the case of large magnification ($z_s \ll z_d$), the defocusing distance is essentially equal to z_s. In the parallel beam geometry ($z_s \gg z_d$), the magnification is close to unity and the defocusing distance $D \approx z_d$.

For the parallel case this latter instructs that to do holotomography based on multiple intensity measurements it is sufficient to change relative sample-to-detector distance by moving the detector only while in the case of the divergent beam that would not alter significantly the defocus distance($D = \frac{z_d}{M}$). Instead as follows directly from relations 85 one has to manipulate the sample position along the beam direction. This is the reason for choosing the configuration of the KB system and sample stage as described in the previous subsection.

For all the projection microscopy presented in the next chapter the x-ray detector consists of a Gd_2O_2S:Tb scintillator, a Fast REad-out LOw Noise CCD based camera and visible light optics. It provides an effective pixel size of $7.46\,\mu$m and is installed at a fixed distance $z_s + z_d$ of $3.93\,$m from the focal plane. The energy was set to $20.5\,$keV (wavelength $\lambda = 0.06\,$nm) corresponding to the third harmonic of the $32\,$mm period undulator of beamline ID19 located 145 m upstream of the KB device.

A single radiograph can be recorded with a spatial resolution better than $100\,$nm, but the resolution in tomographic mode is generally worse than that and much effort is needed to keep it close to the value of the individual projections. Before the three dimensional reconstruction itself can be applied, individual images must undergo preprocessing to compensate for several image quality degrading phenomena present in the imaging system. A first correction is related to the figure errors of the reflecting surfaces resulting in deviations with respect to a spherical wave of the sample illumination. In first approximation they induce a geometrical distortion of the images. To correct for this distortion, two-dimensional grids, in particular two silicon phase gratings of 2 and $3\,\mu$m period are used as simple wavefront sensors. At the end of the tomographic image acquisition the grids are imaged at the same focus-to-sample distance z_s. By registering the positions of the maxima and minima of the grid images and employing a pure geometrical optics approach, the angular displacements α of the real extrema compared to the ideal grid image can be readily related to the phase distortion $\Delta\varphi(x, y, z)$ of the wavefront by

$$(\alpha_x, \alpha_y) = -\frac{\lambda}{2\pi}\left(\frac{\delta\Delta\varphi}{\delta x}, \frac{\delta\Delta\varphi}{\delta y}\right). \tag{87}$$

with coordinates x and y perpendicular to the mean propagation direction z. From the average observed period in the images one directly determines the exact magnification and thus the focus-to-sample distance assuming the grid pitch is known with sufficient accuracy.

The information obtained this way has been used to 'undistort' the radiographs by means of interpolation techniques. The idea behind the undistortion procedure can be explained with the help of figure 11. In the most general case we assume the measurement of the wavefront to be performed at the plane G not coinciding with the plane S in which the tomographic scan has been taken. For simplicity we derive in one-dimension the relation between the displacement Δx_d of the grid maxima position x_g measured at the detector and the distortion expected in any other plane S where the sample is placed. Due to the angle deviation δ_i arising from the improper mirror curvature the grid i-th maxima x_{gi} is projected not into the expected point $x_{di} = \frac{z_D}{z_g} x_{gi}$ but into a point shifted by Δx_{di}. This point then corresponds to sample coordinate

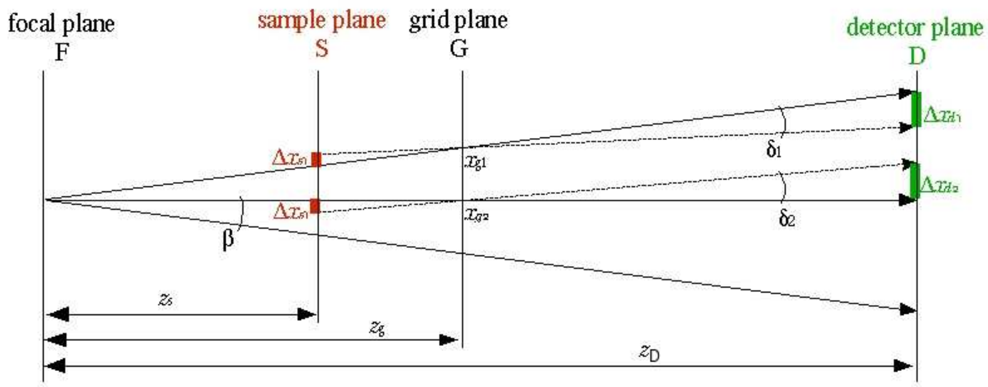

FIGURE 11. Graphical representation of the calculation of image distortion measured at a given plane using the two-dimensional grids. Note that $z_D$is now the fixed distance from focal plane to detector, unlike the above defined z_d being the sample to detector distance.

x_{si} given by

$$x_{si} = x_{di} + \Delta x_{di}. \left(\frac{z_s - z_g}{z_D - z_g} \right) . \frac{z_D}{z_s} \tag{88}$$

If the grid is placed exactly in the same plane after removing the sample, this equation simplifies. But it can be more convenient to measure the mirror deformation by placing a grid in a different plane without removing the sample. In such cases the generalized equation (88) must be used.

Figure 12 demonstrates the applicability of this method to undistort the images, by undistortion of the image of the grid that was used to measure the distortions .

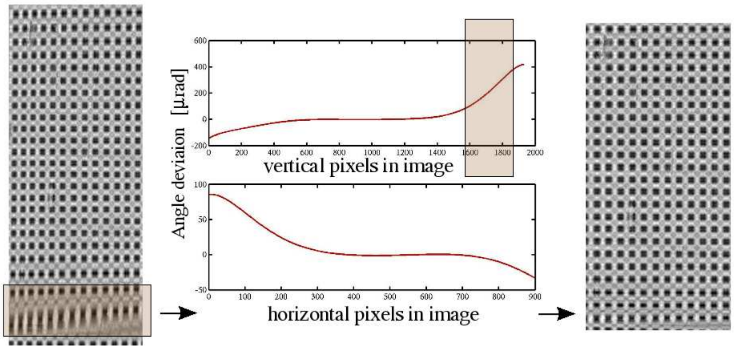

FIGURE 12. Characterization of the wavefront with a 2 μm period grid. Left: distorted image; middle top: vertical angular deviation as a function of the vertical pixel coordinate; middle bottom: horizontal angular deviation as a function of the horizontal pixel coordinate; right: same grid image after correction of the distortions. The optical figure errors increase towards the edges of the mirrors as highlighted on the lowest part of the left image.

Due to the defocusing a single radiograph is a Fresnel diffraction pattern determined both by the attenuation and phase modulation introduced by the object. To disentangle the object information radiographs are recorded corresponding to different focus-to-sample distances. More than two values of z_s are required in practice for reliable phase retrieval due to intrinsic properties of Fresnel diffraction patterns, a single pattern at defocusing distance D being blind to the spatial frequencies $\sqrt{p/(\lambda D)}$ of the phase modulation for all natural numbers p. The next step consists in bringing all images to the same magnification and origin. This procedure will be illustrated on a two-dimensional example in section 6.1. Having performed this data processing we obtain in-line holograms of the sample as in the parallel beam case. To these we apply the phase retrieval algorithms (Cloetens *et al.*, 1999) modified for the KB geometry. The modification involves merely to incorporate the relations 85 that formalize the equivalence between divergent and parallel beam geometry.

Another element of the adaptation of the direct phase retrieval procedure consists in understanding the frequency contents of each projection. As each scan is recorded at a different magnification using the same detector, after incorporating the equivalence relations 85 one still faces the problem of the sampling frequency difference. The highest spatial frequencies contained in the images of highest magnification can not be found in the less magnified images since the detector response is finite. For these spatial frequencies it is as if only a single distance is available, hence the phase retrieval can be undetermined. When treating the processed radiographs as a set of parallel projections the absence of these frequencies can manifest itself in the form of marked noise content. To remove the frequencies contained only in one projection set a low pass filter is used with the cut-off frequency equal to the highest frequency in the second best magnified image. The Fourier transform of the image at the highest magnification then looses the frequency components above this value as shown in figure 13. Such a modification of the images causes certainly blurring, but at the same time, one condition for the propagation based multiple distance phase retrieval is fulfilled this way and the image quality in terms of noise is better. The effect on a real dataset will be examined in section 6.2.4.

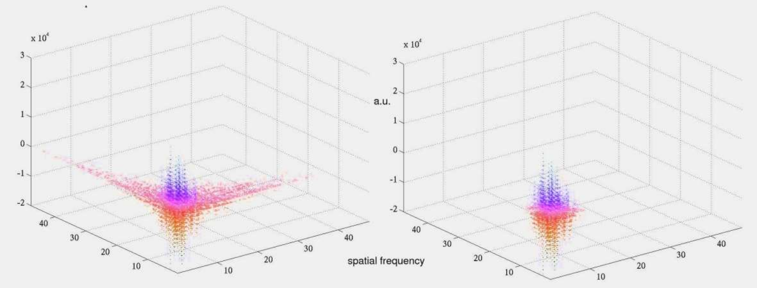

FIGURE 13. Frequency representation of an image of an Al-Cu sample at highest magnification is shown in the left figure. The right distribution is obtained after cutting the tails that are not contained in the projection at the next best magnification

The phase maps constitute *projections* of the object and therefore the correct input for the tomographic reconstruction. The reconstructed slice is a quantitative representation of the local refractive index decrement δ, which is proportional to the electron density. For the tomographic reconstructions we use the same filtered back-projection algorithm as for the parallel beam case. This is justified as a first approximation by the small divergence of the beam not exceeding

3.5 mrad. Two types of samples were investigated: narrow samples (diameter of $70 - 100\,\mu m$) whose lateral dimensions do not exceed the field of view even at the highest magnification and wide samples whose lateral dimensions (of the order of $1\,mm$) exceed by a factor of 10 or more the field of view. The reconstructions on the narrow samples show strong ring artifacts as can be seen in the tomographic slice in figure 14, which is based on a single distance without phase retrieval. The rings are attributed to imperfect correction of the background image introduced by the beamline and KB optics. This correction is done for practical reasons by the so-called flat-field correction which consists in dividing the intensity of the image with the sample by the intensity without the sample and does not take into account any wave phenomena (in reality a division of the complex wave-fields would be required). This approximation fails when strong refraction effects occur as it is the case near the boundaries of an object with a diameter of $50 - 100\,\mu$m. This 'lens-effect' is much less pronounced on nearly flat samples so it is not perturbing the radiography of this kind of objects. However this represents only a fraction of the possible materials to study, therefore other solutions to prevent the strong refraction or to correct for it are required. In practice embedded samples or samples exceeding the field of view in the direction perpendicular to the rotation axis represent an elegant solution since the specimen preparation of the bulky samples is of course much easier. Furthermore they are more relevant from the application point of view (for instance for in-situ deformation experiments and other dynamic studies). Employing this type of samples brings us to the *local tomography* mode.

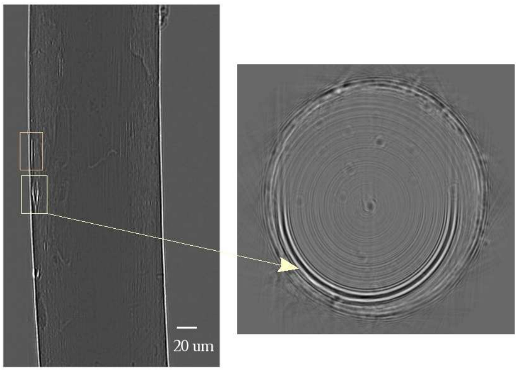

FIGURE 14. The origin of ring artifacts with the KB system. The radiograph of an aluminum wire (left) featuring a dust particle on the mirror and its tomographic slice (right) with a strong ring artifact. The artifact arises because the projection of the dust particle is not removed from the raw images by the flat-field procedure due to refraction at the edge of the sample with which the image of the dust particle coincides.

The filtered backprojection algorithm is a global procedure in that the standard convolution formulas for reconstruction at a single point require the integrals over all lines within some plane containing the point. Local tomography, as introduced initially, results in the reconstruction of the related function Λ_f where Λ (in mathematics literature known as Calderon's operator) is formally the square root of $-\Delta$, the positive Laplace operator. The inversion formulas for this operator are approximate and have to be carefully chosen depending on the accuracy of the available measurements. The reconstruction of Λ_f is local in the sense that the reconstruction at a point requires integrals only over lines passing infinitesimally close to this point. Λ_f has the same smooth regions and boundaries as f. However, Λ_f is cupped in regions where f is constant (Faridani *et al.*, 1992; Ramm and Katsevich, 1996). For conventional absorption CT, local tomography algorithms to reconstruct the $\Lambda_\mu(x, y, z)$ function instead the attenuation coefficient $\mu(x, y, z)$ have been proposed (Faridani *et al.*, 2001) and are based on the linear combination

$$L_f = \Lambda_f + q.\Lambda_f^{-1} \tag{89}$$

where q is determined by trial and error. For phase contrast tomography a local reconstruction algorithm was recently derived, based on the homogeneous weak absorbing object assumption (Anastasio *et al.*, 2003). The principle is the relation between the simply backprojected image $T_{BP}(x, y, z)$ and the desired object function $T(x, y, z)$

$$T_{BP}(x, y, z) = \Lambda^2 T(x, y, z) * \frac{1}{\sqrt{x^2 + y^2}} \tag{90}$$

hence a convolution with a low pass filter. All the singularities contained in T are contained in $\Lambda^2 T$ implying the same to be true for the T_{BP}. Anastasio's derivation assumes the knowledge of the wavefield directly behind the object. This information is principally not available when using the KB setup for magnified tomography. Nevertheless the influence of local tomography in phase-contrast based imaging is less pronounced than in absorption tomography the reason being the fact that the filtering operation explicitly applied in local absorption tomography is applied implicitly to the phase contrast projection data by the wave-field propagation within the paraxial and the near-field approximation.

The effect of projection truncation (by local tomography) in phase contrast microtomography was empirically studied by Weitkamp, to come to the conclusion that the region of interest (ROI) reconstructed from truncated projections is very similar to the corresponding region of the image that was reconstructed from the un-truncated projections by the use of filtered back-projection (Weitkamp *et al.*, 2002). The quantitative results that will be presented in the next chapter confirm this interesting aspect of the FBP in phase contrast tomography.

CHAPTER 6

Applications at sub-micrometer resolution

1. Examples in two dimensions

A relatively simple experiment consists in recording only 2D projections of a flat sample at high resolution. Such an experiment can be complementary to fluorescence mapping. Both can be performed with the same instrument described in the previous Chapter. For the fluorescence mapping, unlike in the tomographic setup, we place the region of interest of the sample into the focal plane.

The cellular and subcellular distribution of biologically relevant elements, such as phosphorus (ATP, DNA), zinc (transcription factors), calcium (second messenger proteins) and iron is a scientific question of strongly increasing importance in biomedical and life sciences research. The x-ray beam of selected energy impinging on the sample excites secondary emission from it. The radiation emerging from the sample includes the characteristic X-ray lines of major and trace elements present in the sample. The emitted x-rays are detected using an energy dispersive detector. In our case it is a Roentec silicon drift detector installed at an angle of 90° with respect to the beam and 45° with respect to the plane of the flat sample (see figure 1). The intensity of the fluorescence spectra depends on the concentration of the studied elements but also on the intensity of the incoming beam. In this respect the KB is very efficient with a x-ray flux up to 10^{12} photons/s. One principal difficulty for the spatial resolution of x-ray fluorescence maps is to achieve the appropriate focal spot size. With the above described KB system also this requirement is met.

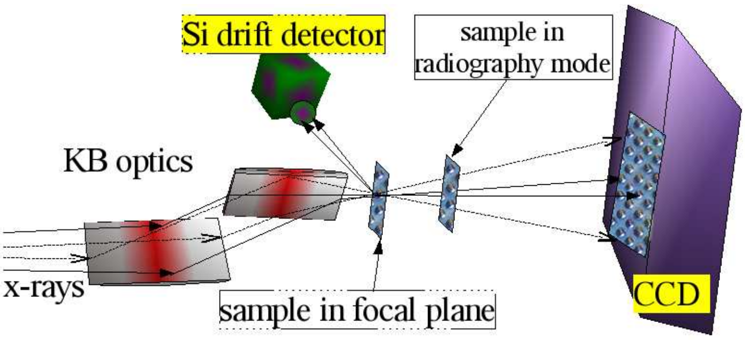

FIGURE 1. The setup for fluorescence mapping in combination with radiography.

Radiographs acquired during the fluorescence measurements have several function. Firstly, they serve to obtain images of the sample that help for the alignment of the appropriate region. Secondly, we can correlate the element distribution map resulting from the spectroscopy with the micro-structure as shown in the phase maps. In our context radiography of a neuron cell will in addition serve to demonstrate the alignment and phase retrieval procedure which will also be used in the tomography setup. The approach is illustrated in Figure 2 on a flat sample consisting

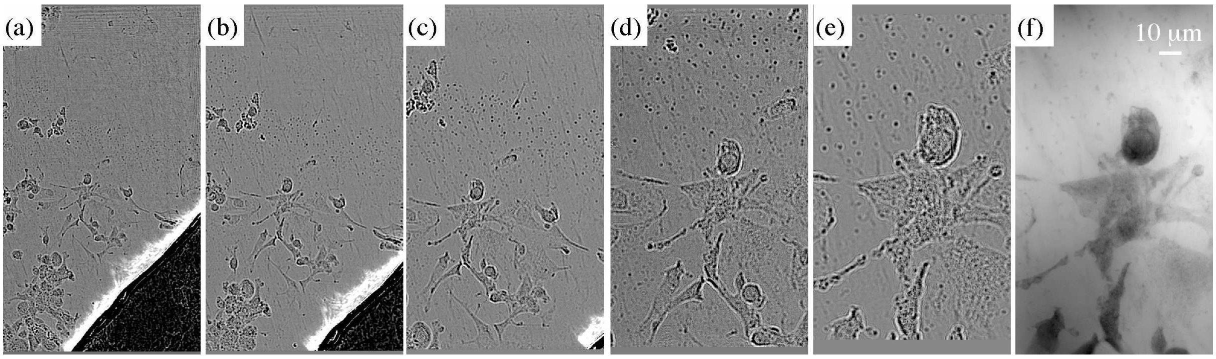

FIGURE 2. A neuron cell at multiple defocus distances and the relative phase map (f) as a result of the combination of all the five radiographs (a)-(e). These projections of a freeze-dried neuron cell demonstrate the effect of the sample-to-focus distance z_s variation on the magnification M and effective defocusing distance D. The radiographs are corrected for mirror distortions and recorded at $z_s = \{225;\ 175;\ 125;\ 75;\ 45\}$ mm, corresponding to magnifications $M = \{17;\ 22;\ 31;\ 52;\ 87\}$. Retrieved phase map in (f) is obtained by combining numerically the five radiographs and bringing to the magnification of the image at the smallest z_s. The pixel size of (e) and (f) are hence identic and equal to 85 nm. Note that in (f) the resolution is not affected by many deteriorating phenomena present in the tomographic mode.

of freeze-dried neuron cells on a 2 μm thick polymer film. Figures 2(a), (b), (c), (d) and (e) are radiographs after correction for the mirror distortions but before bringing them to the same maximum magnification as radiograph (e). The result of the phase retrieval procedure is shown in Figure 2(f). The algorithm uses the five distances and assumes the object to be a pure phase object (we apply the approximation 2.2.13). As evidenced by comparison between images (e) and (f), phase retrieval is unavoidable in this geometry to improve the spatial resolution that would be otherwise degraded by the presence of the diffraction pattern.

For the fluorescence mapping we virtually divide the sample by a 2D mesh with a period that approximately corresponds to the resolution of the technique given by the $100\,nm$ focal spot size and its stability. The sample is mounted on a XY piezo table with a range of $100\,\mu m$ and an accuracy of $20\,nm$. Assuming that the focus does not vibrate or drift more than its own dimension, we raster-scan the sample accross the focal spot with the piezo stage to obtain the full spectrum of x-ray fluorescence at each scan point. The resulting three-dimensional data set (sample x position, sample y position, photon energy E) is reduced to maps reprepresenting the elements of interest (e. g., Iron in our case) by integrating over spectral regions of interest (ROI filtering) or to concentration maps by fitting the spectra.

A measurement of the full fluorescence map of a $20 \times 20\,\mu m^2$ sample region takes typically a few hours. During this time the position of the focal spot must be well defined in order to obtain a correct scan, hence the thermal stability is an issue for this type of imaging as well.

Another example for the use of the very high spatial resolution of the system has been presented in (Pereiro-Lopez *et al.*, 2005) on the case of Ga penetration at grain bondaries. In order to observe this phenomenon, one has to characterize simultaneously the presence of nanometric liquid metal penetration layers and possible associated relative grain movements of the same amplitude. The high flux of the KB system allowing short exposure times is here essential as the penetration time of Ga along the grain boundary of an Al bi-crystal is of order of tens of seconds as seen in figure 3.The grain separation is calculated by measuring with cross correlation techniques the motion of two regions at either side of the grain boundary. In order to quantify correctly the grain separation it is crucial to account for the image distortion introduced by the mirrors and determined with a two dimensional grid pattern placed in the beam before or after the image acquisition (see equation 88) .

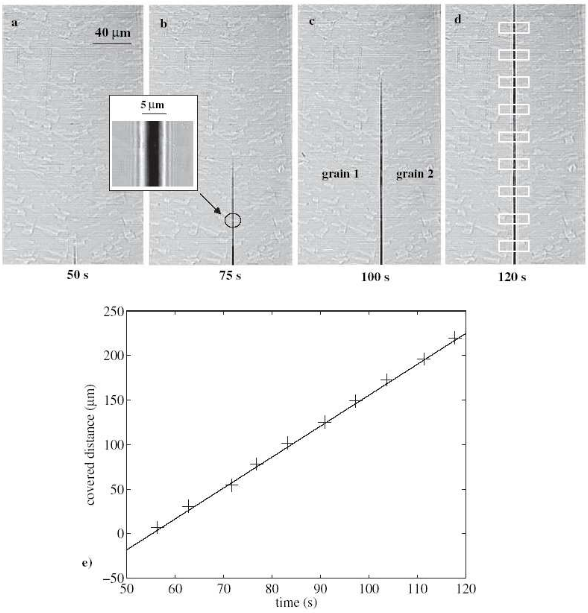

FIGURE 3. (a)-(d) are the radiographs showing Ga penetration and (e) shows the distance covered by the Ga layer as a function of time. (courtesy of Eva Pereiro)

2. Aluminum alloys

2.1. Aluminum matrix alloys: an introduction

. Although it is the most abundant metallic element on the Earth's surface, the discovery of aluminum is of a fairly recent date. Oersted probably isolated the first metallic impure aluminum in 1824 by reducing aluminum chloride with potassium amalgam, but generally Wöhler is credited with the discovery of the metal by virtue of the first isolation of less pure aluminum in 1827 and the first description of several of its properties.

Pure aluminum is too soft for most structural applications and therefore is usually alloyed with several elements to improve its corrosion resistance, inhibit grain growth and of course to increase the strength. The optimum strengthening of aluminum is achieved by alloying and heat treatments that promote the formation of small, hard precipitates which interfere with the motion of dislocations. Aluminum alloys that can be heat treated to form these precipitates are called heat treatable alloys. Pure aluminum is not heat treatable because no such particles can form.

Near nano-structured or ultrafine-grain materials are defined as materials having grain sizes whose linear dimensions are in the range of $100\,nm$ to $1\,\mu m$. The physical properties of these materials are potentially superior to those of their coarse-grained counterparts. This potential superiority results from the reduced size or dimensionality of the near nanometer-sized grains as well as from the numerous interfaces between adjacent grains resulting in a large volume fraction of grain boundaries.

For structural applications studies of the microstructure and its modification due to heat treatment need to be conducted in the bulk of materials. X-ray tomography has proved to be a very suitable technique to do this for Al based alloys.

In the following sections we present two aluminum alloys. First being the Aluminum - Silicium, the second an Aluminum - Coper sample.

2.2. Performance of phase retrieval methods for the Al-Si type samples in the KB geometry

. Before proceeding to the main point of this section, a short notice is relevant on the possibility to reconstruct the scans without performing phase retrieval. Using a less rigorous approach one could consider the dark and bright fringes where phase contrast is present as a region of respectively more or less absorption. If the system can be adjusted so that this effect is optimized for best visual quality, conventional tomography could be performed. The reconstruction based on absorption works if the images are approximately projections, i.e. if the contrast is weak. The tomogram on figure 4 is the result of such simplified reconstruction approach. Though this section deals with Aluminum/Silicon alloys, for illustration here we have chosen onpurpose the Al-Cu sample. The reason is that the Al-Si sample would show very little contrast and on a more absorbing sample we still clearly see the contrast degradation by the Fresnel diffraction pattern near the interface of the particles. In addition to this, no quantitative tomography is possible in this case without phase retrieval. Phase retrieval is then a necessity if one aims to extract the most out of the images particularly with the KB setup. It has been shown in (Cloetens *et al.*, 1997) that the filtered backprojection algorithm which is strictly only valid for absorption, will also give correct results in the so-called *edge detection regime*. This regime is reached when the defocusing distance D is small, such that for a given resolution $\lambda D f_{max}^2 \ll 1$, where f_{max} is the maximum spatial frequency which is related to the object size a. Each border in the sample is a phase jump which is imaged independently. The image has close similarity with the object, and an immediate interpretation is possible. For large distances D when the object size is much smaller than the first Fresnel zone ($a \ll (\lambda D)^{1/2}$ or equivalently $\lambda D f_{max}^2 \gg 1$) the far-field holographic regime is set on (Fraunhofer diffraction). For intermediate distances D where the size of the Fresnel zone is comparable to the characteristic dimensions of the object, the resulting image is an in-line hologram. This is always the case for the KB system. It is not possible to have D too small as that would mean an extremely small field of view and very severe distortion effects if we move close to the focal plane.

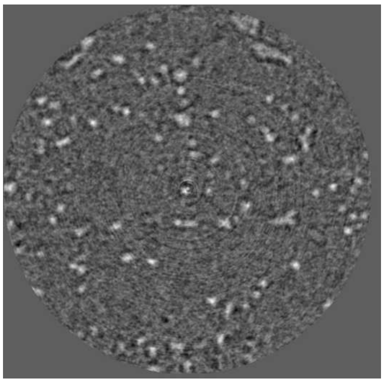

FIGURE 4. Tomographic slice of an Al-Cu alloy without phase retrieval. The pixel size is 90 nm. The contrast degradation can be clearly seen wherever an abrupt density variation takes place. The tomographic slice which is shown here contains 1024×1024 pixels.

As the first example we will address the microstructure of an Al-Si alloy. With conventional absorption based x-ray imaging we can not distinguish between the Aluminum and Silicon phase since their mass attenuation coefficients are too close to each other, $\beta_{Al}(20.5\,keV) = 3.65\,10^{-9}$ and $\beta_{Si}(20.5\,keV) = 4.15\,10^{-9}$(NIST, 2006). Therefore coherent imaging is required to measure the refractive index difference $\Delta\delta$ rather than $\Delta\beta$ as the former is three orders of magnitude larger. The sample itself is machined to a cylinder of 1 mm in diameter and scanned at five different defocus planes. The five sample-to-focal plane distances were $z_s = \{47.5;\ 67.5\,;127.5;\ 187.5;\ 267.5\}$. The closest position corresponds to magnification $M = 83$ so with the $7.46\,\mu$m pixel size of the detector this results in the image pixel size of 90 nm.

The post-processing described for the two dimensional imaging in sections 4 and 1 is used for the radiographs of the tomographic scans. When the corrected radiographs are prepared, we proceed to the phase retrieval step.

Since the tomographic imaging at the given scale with the KB-type instrument has not yet been reported we have tested and compared several phase retrieval methods in order to find which is best adapted to our setup. Moreover this comparison can be helpful for other non-standard scanning instruments. All the tests were performed on real data sets. The advantage over the use of a phantom is that the robustness of the selected method with respect to noise and other experimentally unavoidable artifacts comes to daylight.

To start with the simplest case, we first apply the slowly-varying phase approximation (given by formula 2.2.14) to retrieve the phase maps. Hence we assume that the sample is a pure phase object and that there are no abrupt phase variations. This assumption is obviously too strong for the Al-Si sample as we have the Si grains that do not necessarily fulfill the condition of slow phase variation and there is an envelope of absorption as well. The result corresponds to these

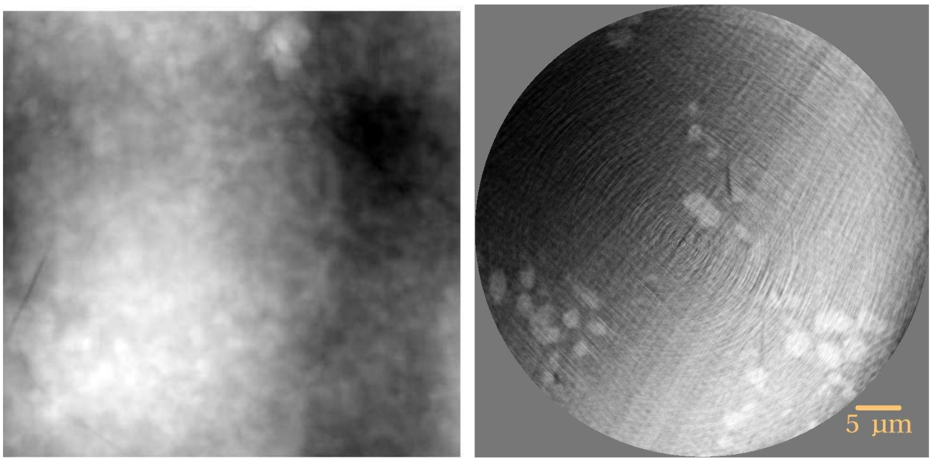

(a) (b)

FIGURE 5. Phase retrieval based on the slowly varying phase approach results in a phase map (a) (here the Al-Si sample) with little contrast and a tomographic slice (b) with an intensity gradient (north-west / south-east on the image). The reconstructed slice is 1024×1024 pixels corresponding approximately to the horizontal field of view of the imaging system. The pixel size is 90 nm as it is the case for all the images in this section on the Si alloy.

considerations, as seen in figure 5. Both the phase map (figure 5(a)) and the tomographic slice (figure 5(b)) show that the high spatial frequencies are missing and a gradient of intensity is clearly visible on the tomographic slice.

A less restrictive approach used extensively for the tomography with parallel beam is the weak-object approximation (see equation 2.2.15). The phase map 6(a) contains high frequency noise, that has severe consequences as can be seen in the reconstructed slice in figure 6(b). The 'semi-ring' artifacts are rather strong in this case. We name it 'semi-ring' artifact since these are generally not the usual $360°$ rings, but often they are half rings (we rotate over $180°$) with the centers of rotation not always at identical postion for each ring; a consequence of the misalignment of the individual scans in the holotomography recording process. Therefore it is rather difficult to correct for them in the image. The noise amplification is related to the non-perfect flat-field procedure. The transfer function shown in figure 2.2.1 will have many closely spaced zeroes for the relatively large distances used in our experiments. Even in the case of five distances, significant amplification of the hight spatial frequencies can result. This is especially the case for the highest spatial frequency range where only one distance contributes effectively. With other words, even in the case of five distances, the twin image problem is only partially solved.

The correction by a recursive refinement of the phase maps, for the nonlinear terms that are neglected in the weak object approximation has its benefits. The segmentation of the sample in figure 6(c) is considerably more simple when the high frequency noise is reduced. The recursive step is however CPU time consuming and does not always bring a significant improvement.

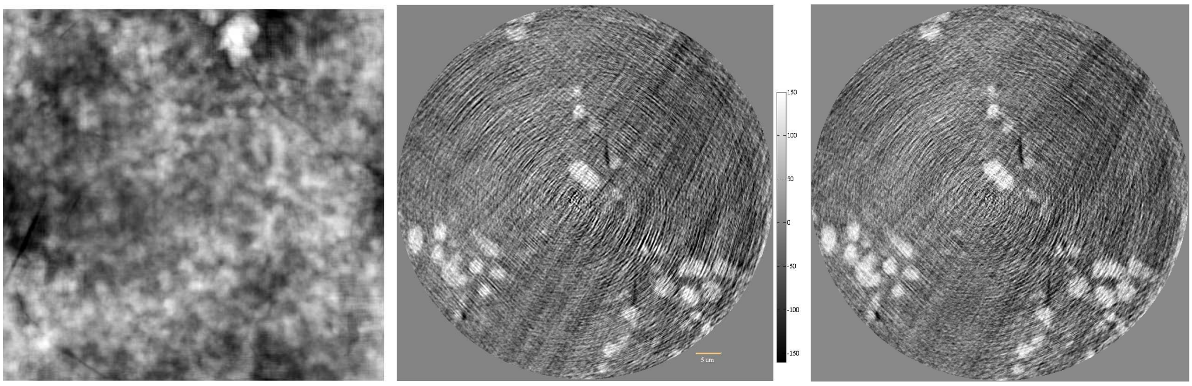

(a) (b) (c)

FIGURE 6. A phase map (a) and tomographic slice (b) for the case of the weak-object approximation. This direct method followed by 5 iterative refinement steps (recursive correction of nonlinear terms) results in the tomogram (c) with less high frequency noise. The phase map is not shown for the recursive step as small changes are difficult to observe on the phase maps that contain the projection of the whole bulk sample. This is partly the reason for comparing rather the tomographic slices.

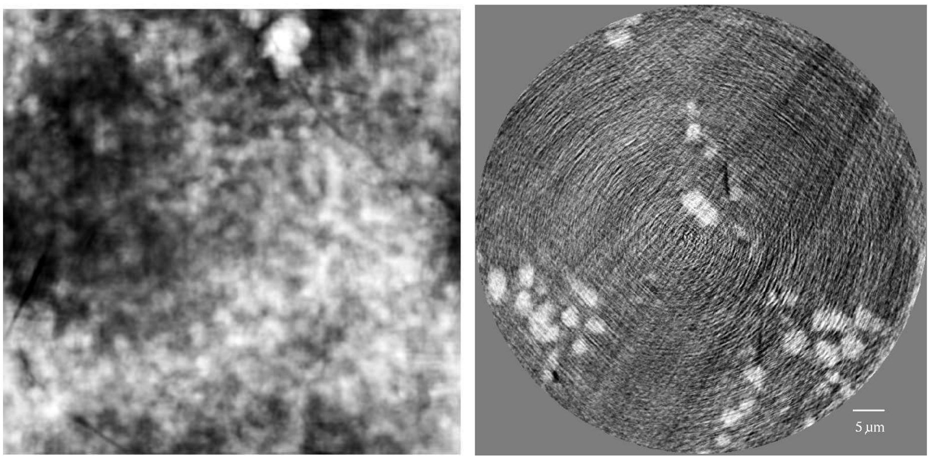

(a) (b)

FIGURE 7. The phase map (a) and the tomographic slice (b) for the paraboloid method. Note the dark stripes on the tomographic slice marked by the arrows. These arise due to the contribution of large objects entering the field of view for only a few projections.

More adapted to our special configuration and to this sample is the last direct method tested here. The paraboloid method (see equation 2.3.18) is usually applied in electron microscopy, but has not been very successful with X-rays for the parallel beam case. The reason for more success here is that our sample exceeds the field of view and hence does not introduce strong phase gradients at the sample edges. The paraboloid method is better adapted to flat samples with fluctuations around a rather constant average. The tomogram in figure 7 (b) reveals the

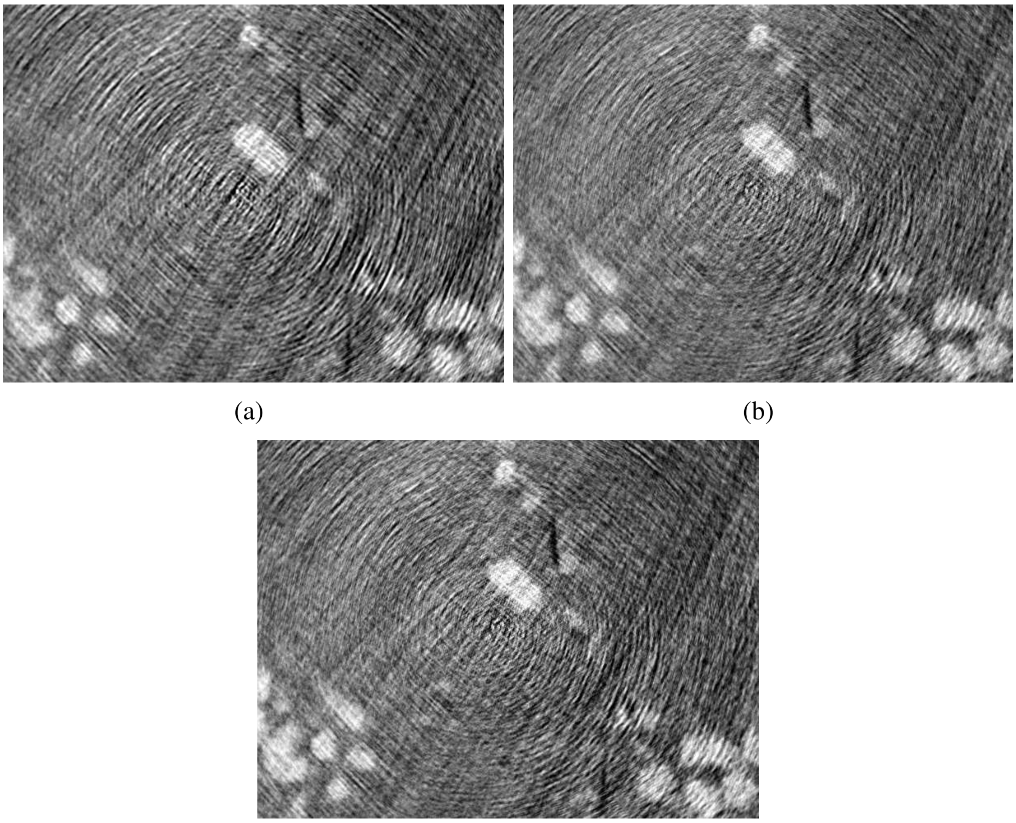

(a) (b)

(c)

FIGURE 8. Comparison of a detailed view of the tomographic slices if phase retrieval is performed using the weak-object approximation (a), its refinement by recursion (b) and the paraboloid approximation (c). (b) and (c) have similar quality, however the recursive steps are very CPU time consuming compared to the direct paraboloid method.

improvement of the reconstructed image quality in the sense of less high frequency noise and better contrast.

Attention has not yet been payed to the clearly visible stripes present on all the tomograms shown in the above comparison (see e.g. figure 7 (b)). They are due to a large object entering the field of view at the angles corresponding to the direction of the stripes. This object, even if present only in a few projections, contributes significantly as it introduces a faulty phase shift and absorption profile at the given angle. For the segmentation and analysis of the image this artifact is usually not a limiting factor.

We can conclude that the best direct method for the phase retrieval in the case of the Al-Si cylinder imaged in the magnified setup is the paraboloid method.

2.3. 3D quantitative measurements of the Al-Si microstructure: grain shape and distributions

. A volume rendering performed with the commercially available software Amira is shown in figures 9. The latter gives a persuading visual proof of the not so surprising fact that the Silicon particles are gathered in distinct regions on the borders of ’dendrits’. The dendritic geometry is a result of the cooling process. The first phase that solidifies contains only very small amount of Si, it is called the α-phase of the solide with the typical structure called dendritic. The phase that is still liquid is then enriched in Silicium. When we reach the temperature called 'eutectique' the liquid has a particular composition containing Silicium. A little decreasing in temperature is now enough to completely solidify the alloy, and the Si particles (in white on figure 9) are located in this 'eutectique' part of the alloy. It is also in this moment when the porosity (red on figure 9) is created as well as the iron rich component (blue on figure 9). This spatial distribution typical for the cast dendritic structure of this alloy can of course not be determined with two dimensional imaging techniques.

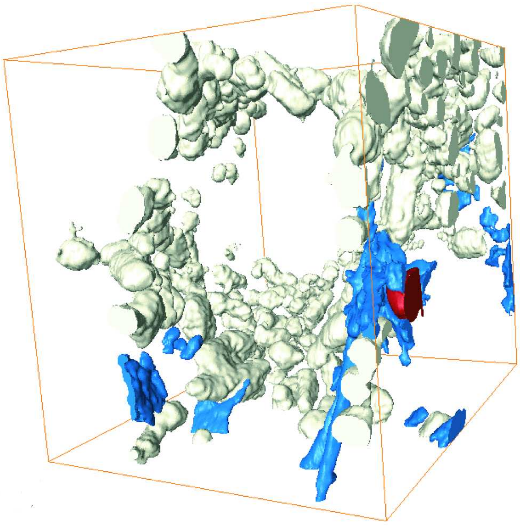

FIGURE 9. A 3D iso-surface representation of the AlSi sample. The Silicon of the eutectic phase accumulates in specific structures. The white particles stand for Silicon, red for air and blue for iron rich inclusions. The subvolume on the image has the dimensions of 300 × 300 × 300 pixels with 90 nm pixel size.

In accordance with what has been stated in the previous chapter we can determine the relative values of the refractive indices δ for the compounds present in the material of study. Having chosen a slice in figure 10 that contains an air-filled pore it is furthermore possible to determine all the δ values nearly absolutely assumed that $\delta_{air} = 0$. What we actually reconstruct in the tomograms is

$$-\frac{2\pi\Delta\delta}{\lambda} \tag{91}$$

which implies that measuring the gray-scale value difference in the slice gives the refractive index difference between the element x and y using $\Delta\delta = -\frac{\lambda}{2\pi}(gv_x - gv_y)$. Based on a mean gray-scale value in selected regions on the tomographic slice the above formula provides the results summarized in table 1.

The measured difference in refractive index $\delta_{Al} - \delta_{Si}$ between the Al and Si phase in the tomographic slice is $0.13 \pm 0.03 \times 10^{-6}$ very close to the expected value of 0.14×10^{-6} for pure Al-Si. The error of the measurement expressed in the form of its standard deviation arises

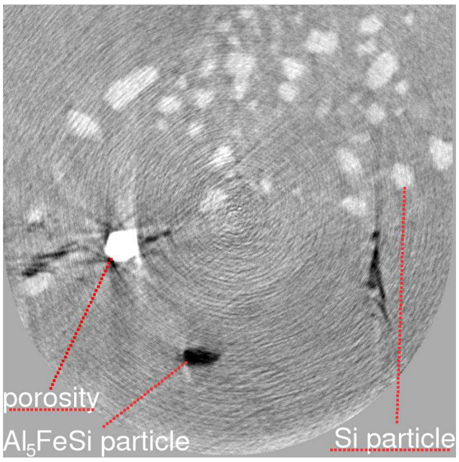

FIGURE 10. Lateral slice (1024×1024 pixels at 90 nm pixel size) accross a region of the Al-Si cylinder where the three phases are visible and an air pore which saturates for the gray-scale level chosen. The dotted lines show the corresponding features in the image that have been used to calculate the refraction index decrement difference of the composites.

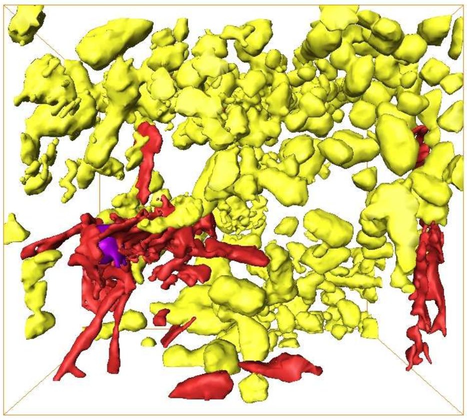

FIGURE 11. 3D rendering of the Al-Si sample showing clearly the shape and distribution of the Al_5FeSi particles in the volume. The labeled particles have three colors each standing for a separate phase. Yellow for Silicon, red for the Al_5FeSi component and violet for the air pore

from the noise in the image and is mostly due to reconstruction artifacts. As the tomographic slice (figure 10) and volume renderings (figures 9 and 11) show, there is yet another phase in the studied material. Its refractive index decrement is inferior to that of pure iron hence this third compound is rather an iron rich phase of the form $Al_xFe_ySi_z$ with x, y, z not easy to determine. The presence of these different phases was expected from the composition and processing of the material. The most common reported composition of iron rich particles in this alloy is Al_5FeSi, while some Al_8Fe_2Si can be found as well. The density of the intermetallic phase is also determined from the measurement to be $\approx$ 3.3 g.cm^{-3} allowing to identify it as being

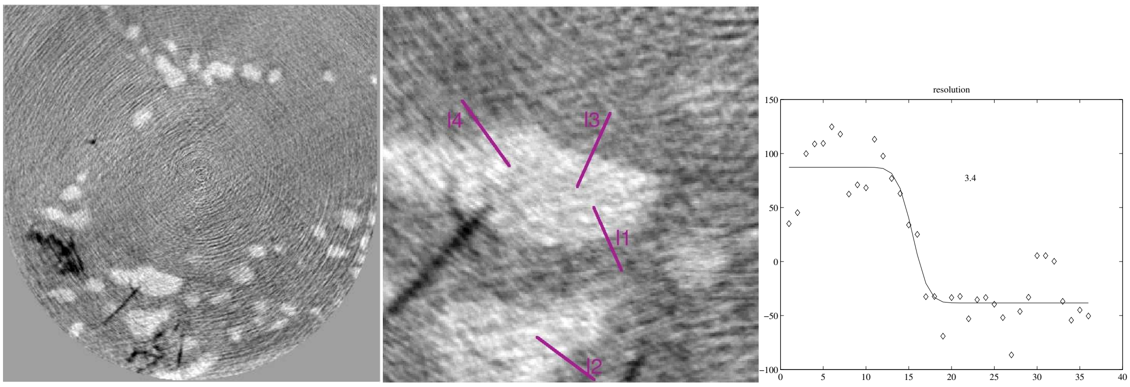

(a) (b) (c)

FIGURE 12. The determination of the spatial resolution in a slice (a) of the AlSi sample. (b) is the zoom on two Si particles used for the measurement. The dark lines represent each a subset of 3 pixel wide lines whose averaged profiles were fitted (c). The average of all the fits gives the final estimate of the resolution (3.2 pixels).

Al_5FeSi since this compound has a defined density of $3.3 - 3.35$ g.cm^{-3} to be compared with 3.58 g.cm^{-3} for Al_8Fe_2Si. This result is consistent with the most common observations

	measured value [x10^{-6}]	tabular value [x10^{-6}]
$\delta_{Al} - \delta_{air}$	1.03 ± 0.084	1.29
$\delta_{Si} - \delta_{air}$	0.89 ± 0.084	1.15
$\delta_{Al-Fe-Si} - \delta_{air}$	1.29 ± 0.087	$\delta_{Fe} = 3.65$
$\delta_{Al} - \delta_{Si}$	0.13 ± 0.032	0.14
$\delta_{Al} - \delta_{Al-Fe-Si}$	-0.27 ± 0.038	$\delta_{Al} - \delta_{Fe} = -2.36$
$\delta_{Si} - \delta_{Al-Fe-Si}$	-0.4 ± 0.038	$\delta_{Si} - \delta_{Fe} = -2.55$

TABLE 1. Relative refractive index increments for the compounds in the tomographic scan

An automatic ring artifact removal procedure did not improve the image quality. As a consequence an interactive ring artifact removal procedure in Adobe Photoshop (Paul Tafforeau, private communication) has also been tried, but it has effected in a negative way the spatial resolution in the image. The latter is determined with the aid of a complementary error function fitting a selected edge (or more precisely an average over several edges). Three lines at each of the orientations indicated in figure 12 (b) form a total of 12 edge profiles that have been evaluated to give a mean value of 3.2 pixels for the resolution. The pixel size being 90 nm, the estimated resolution is 290 nm.

2.4. The optimal phase retrieval procedure for the Al-Cu alloy

. The next sample is a cast Al-Cu alloy again machined down to a cylinder of approximately 1 mm diameter investigated at five consecutive distances during the holotomographic scan. In this case the closest distance is $z_{s1} = 27.5$ mm from the focal plane followed by the sample positions at $z_{s2} = 67.5$ mm, $z_{s3} = 127.5$ mm, $z_{s4} = 187.5$ mm and $z_{s5} = 267.5$ mm. These correspond to magnifications $M_1 = 144$, $M_2 = 58$, $M_3 = 31$, $M_4 = 21$ and $M_5 = 15$. The final voxel size is 52 nm and the field of view approximately $50\,\mu$m in the horizontal and $90\,\mu$m in the vertical direction. This is the smallest voxel size at which tomography with the KB was performed. Taking into account this particular status of the scan the detailed results of preprocessing are presented next, starting with the distortion measured with the grid at the five sample positions. Figure 13 is similar to the one shown in section 4 when discussing the correction for grid distortion. Here we show the results of the distortion measurements in order to compare the distortion profile at the closest and the largest distance. As expected, the shape stays essencially the same, only the amplitude (y axis) diminishes for bigger z_s hence smaller magnification. This is in accordance with the expected behavior in the geometrical optics limit that has been the assumption here and as well the one leading to formula 88.

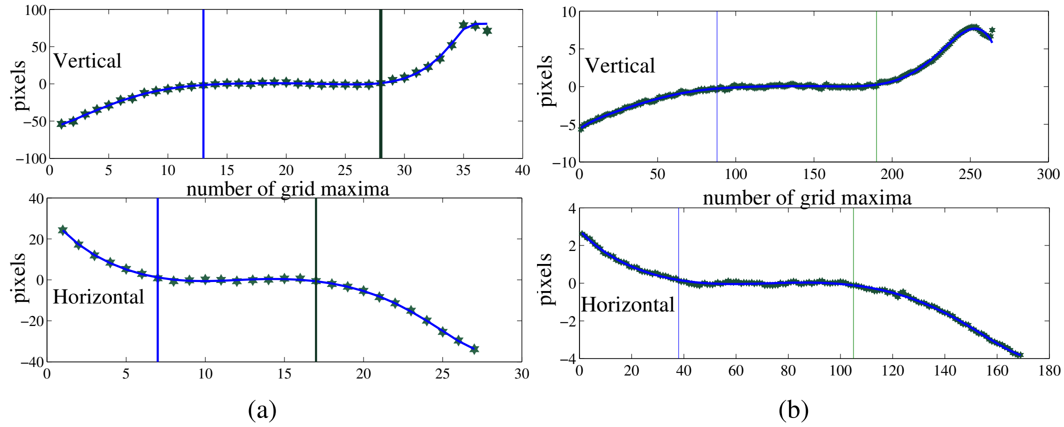

FIGURE 13. Distortion profile as measured by the 2D Si grid at $z_s = 27.5$ mm (a) and $z_s = 267.5$ mm(b). At the closest distance (a) the $2\,\mu$m grid, for the following distance (including (b)) the $3\,\mu$m period grid was used. The region between the vertical markers is the one used as reference to calculate the distance with respect to the focus.

In vertical direction we limit the holographic reconstruction to 1024 pixels eliminating thus from the projections the two extremities of the vertically focusing mirror.

After correction for distortion and magnification, the last step before phase retrieval is the refinement of the mutual alignments of the projections with respect to a reference plane that has been chosen such that the sample moves the less during the corresponding scan. The movement of the rotation axis position is determined by correlating the projection No.1 with proj No.2, then No.2 with No.3 etc. for the whole scan containing in this case 900 projections (angular step of $\pi/900$). For the Al-Cu series the scan moving the smallest amount was the one at $z_s = 27.5$ mm as explained in figure 14(a). By cross-correlation techniques the shifts are calculated and afterwards used in the phase retrieval. For an ideally stable and reproducible system the misalignment between the projections at different distances would be constant during the scan, hence independent on the angle at which the projection is taken. In practice this is far from the case. There is an apparent change in misalignment (figure 14(b) and (c)) during the scans of the order of maximum 30 pixels which corresponds to 1.5 μm. Keeping in mind the specifications of the rotary stage, the measured shifts can be nearly exclusively attributed to this and to the temperature variation. As seen in figure 14 (b),(c), the displacement is calculated for each fifth projection in the scan and is interpolated with either a polynome or a spline function. For the final reconstruction the polynomial fit (8th order) was favored partly empirically and partly because of the fact that the fine shape of the displacement curve may be due to random errors in the cross-correlation. Of course there still persists the effect of rotation axis errors since the displacement correction is only relative between the individual scans. One possible way to correct for the horizontal errors in absolute rotation axis movement during the scan is to acquire a scan of a highly absorbing thin needle, monitor its position during the rotation using inter-correlation techniques and use these values in the preprocessing of the radiographs. We

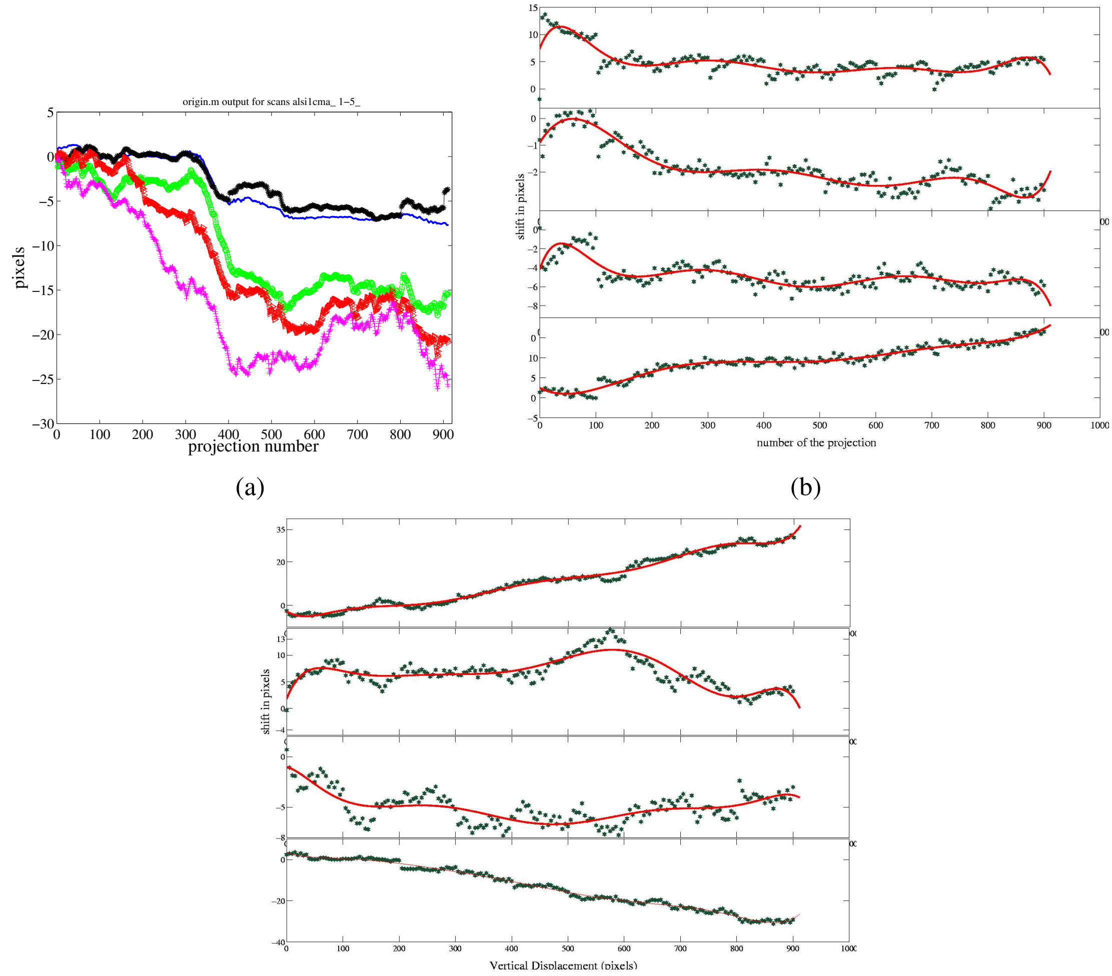

(a)

(b)

(c)

FIGURE 14. Estimated shift of the rotation axis position during scan acquisition shown for the five distances (a). Each scan correspond to a different defocus distance hence the values that are given in pixels on the graphs are related through the magnification. Figures (b) and (c) show the horizontal and vertical displacement of the projection at each angle during the five scans of the Al-Cu sample. The shifts are fitted with 8th order polynomes.

have implemented such routine for scans in the parallel beam case. In the case of the KB this approach is less successful as one can not assume that the errors are reproducible in this range of spatial resolution.

What concerns the optimal phase retrieval method, the situation is different if in the composition of the alloy there is Copper (present as Al_2Cu) instead of the Silicon. For Copper at $20\,keV$, $\beta_{Cu} = 1.34\,10^{-7}$ and $\delta_{Cu} = 4\,10^{-6}$, hence a considerably bigger difference between Al and Cu than in the case of the Al-Si. The applicability of the paraboloid method which retrieves the complex object $T(x)$ is here limited by the effect of phase wrapping in other words the restriction of the reconstructed phase value to the interval $\langle -\pi, \pi)$. This occurs whenever an inverse trigonometric function is used for the phase reconstruction. As a consequence, for an object with phase variation greater than 2π and calculating only the principal value of this phase, the resulting phase map has a sawtooth form. The relationship between the wrapped and the true phase is

$$\Phi(x,y) = \varphi_W(x,y) + 2\pi k(x,y) \tag{92}$$

where $\Phi(x,y)$ is the true (unwrapped) phase value at the coordinates (x,y), $\varphi_W(x,y)$ is the experimental wrapped phase at the same point, and $k(x,y)$ is a wrap count integer field. The phase *unwrapping* problem consists in singling out the correct integer field $k(x,y)$. The solution in 1D is simple, but in 2D the difficulty lies in the registration of phase jumps particularly in noisy data and in the fact that a false jump can corrupt a large two dimensional valid phase distribution. Over the past 15 years more than 200 journal papers have been published on this subject (a short list of the different methods with references can be found in (Meneses *et al.*, 2005) and an extensive introduction to the problem in (Ramm and Katsevich, 1996)), but the methods suggested are generally very particular for a given application and often path dependent or/and noise sensitive. The phase unwrapping as described by (Volkov and Zhu, 2003) can be a promising approach, but it has not yet been fully implemented.

The iterative algorithm encounters the same problem. When tomograms are reconstructed from wrapped phase data, one gets stripes due to pixels with wrong values as shown on figure 15. This problem is still to be solved. The iterative method as proposed in section 2.3.3 could therefore not yet be fully implemented.

The best result for the phase retrieval in the case of the Al_2Cu sample has been obtained by using the homogenous object approach in phase retrieval as described by formula 2.3.17. The ratio $\chi = \Delta\beta/\Delta\delta = 0.019$ for the Al_2Cu was obtained by calculation based on the value of form factors from the NIST database (NIST, 2006). We obtain the same result calculating the β and δ separately (XOP software package developed at ESRF). A phase map together with a tomographic slice of raw reconstructed data in figure 16 shows the result. The beneficial effect of cutting high spacial frequencies can be seen when comparing images (a) and (b). The elimination of all the high spatial frequency components not contained in at least two radiographs results in blurring of the highest magnified scan and hence the final phase maps

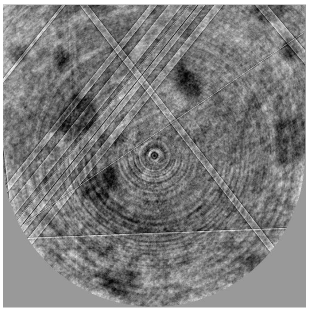

FIGURE 15. Reconstructed slice using the iterative method proposed in section 2.3. The need for phase unwrapping is obvious from the well visible stripes in this image emerging due to phase variations greater than 2π.

as well. At the same time the reduction of noise allows to correctly threshold the output and interpret the result.

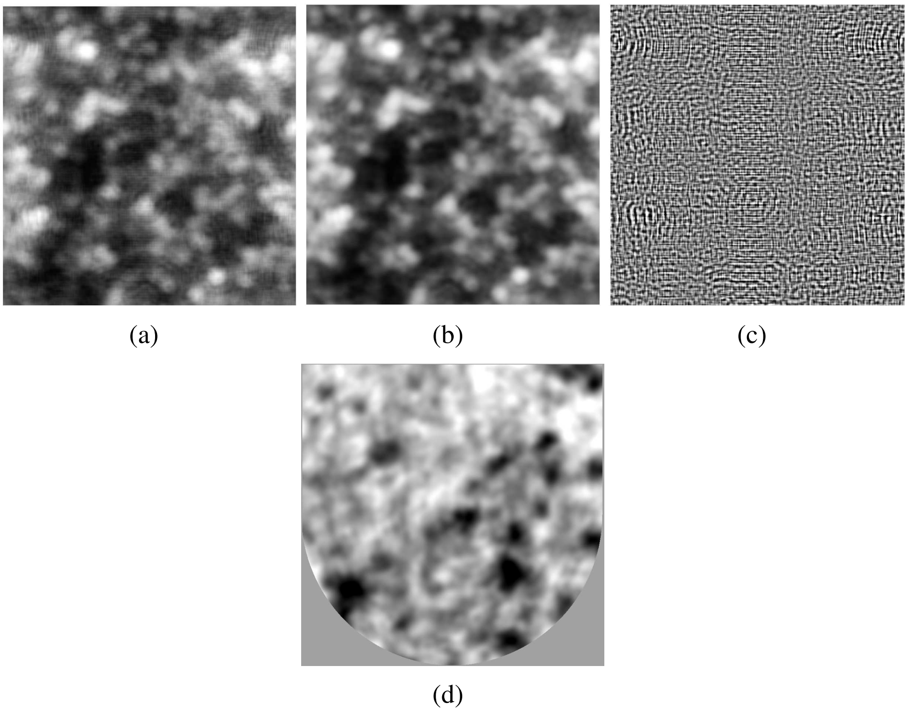

(a) (b) (c)

(d)

FIGURE 16. Phase maps of the Al-Cu sample (part of500×500 pixels at 52 nm pixel size) comparing homogenous object approach (a) to the same approach with eliminated high spatial frequencies (b) and their difference map (c) on the Al-Cu sample. The resulting tomographic slice with the frequency cut applied in (d).

2.5. Following the microstructural changes in Al-Cu during annealing

. Heat treatment of metals is often associated with the hardening process. Hardness measurements can provide a good indication of the strength of a material and since strength is related to the number, type and spacing of precipitates, hardness measurements can be used to monitor the precipitation process. We can address this question from the other point of view and monitor the microstructure of the material during the heat treatment that would allow to directly correlate the macroscopic measurements with those at the scale of the particle sizes. In situ solidification experiments on Al alloys have been performed with x-ray tomography at a temporal resolution of the order of 15 minutes and a spatial resolution of $3\,\mu$m giving access to important statistical parameters (Ludwig *et al.*, 2005). At the high spatial resolution we are addressing in this work the temporal resolution of the experiment in (Ludwig *et al.*, 2005) could not be reproduced but stays of the order of 45 min. We follow therefore the annealing phenomenon ex-situ in only three steps corresponding to the initial (not-annealed) sample $S1$, the same sample after 12 hours of annealing $S2$ and the final state after 24 hours of annealing $S3$. During the annealing the sample is kept in a furnace at a constant temperature of $530\,°C$ while it is imaged at room temperature after quenching and repositioning on the tomographic stage. The interest of going to higher spatial resolution resides in the possibility to characterize the morphological changes of the particles with better precision and also to demonstrate the possibilities of the novel instrumentation for x-ray imaging.

The tomographic volume is as usual converted to an 8 bits representation and thresholded. The visual justification of the threshold value can be seen in figure 17.

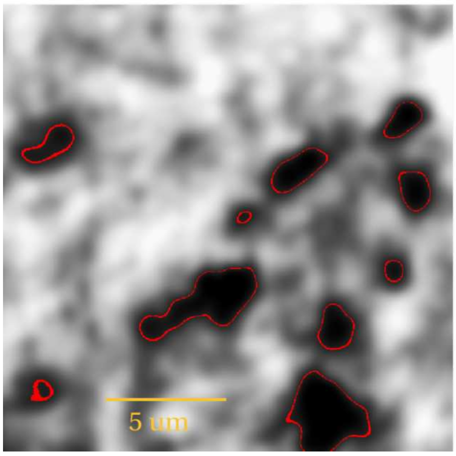

FIGURE 17. Tomographic slice of the Al-Cu sample after 24 h of annealing. The outer edge of the red contours indicates the thresholding at the grey-scale value of 71 (0-255 is the full range for the images) which is a rather crucial parameter for the extraction of quantifiers for the particles.

The Cu is generally used at about 2 wt% to create small precipitates (10 nm in size at most) and strengthen the alloy. The most famous example is the Au_4G precipitate hardening Al alloys. A higher concentration of Cu leads to the formation of coarse Al_2Cu particle which are the object of observation in this study. Higher copper content is sometimes used because these coarse particles increase the modulus and strength of the alloy but in the meantime they reduce its ductility. The volume fraction occupied by the Al_2Cu particles at S1,S2 and S3 has been measured using image analysis. It has been found that the long range average of the Al_2Cu does not change during diffusion at 530 °C, only the local distribution does. This is the first verification of proper segmentation and image quality and the correct recognition of the same region in the consecutive scans. The nominal composition of the sample is a $Al - 7$ wt% Cu and the volume fraction of Al_2Cu measured from the images in average over the three scans is equal to 6.6 ± 2.4 wt% (the standard deviation of 2.4 is obviously purely due to the 2D nature of the calculation hence it is a measure of the volume fraction variation by plane index rather than beeing a real statistical weight for the 3D volume fraction.)

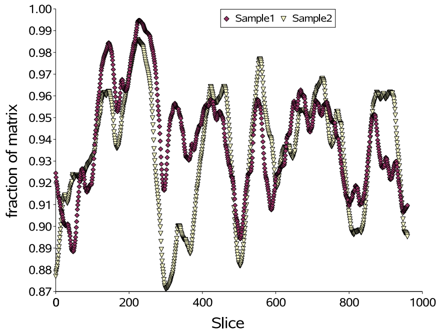

FIGURE 18. The volume fraction of the matrix relative to the total volume for the initial material - S1 (violet diamonds) and for the 12 h annealed sample - S2 (yellow triangles). The slice per slice variation of Al_2Cu particles after annealing follows closely the initial distribution and the mean values are very similar if the whole volume is considered.

The refractive index difference for the two phases in the material has been considered in order to estimate the density of the Al_2Cu phase. For a volumic fraction of 10 % Al_2Cu the measured density value of $\rho_{Al_2Cu-matrix} = 2.71$ g.cm^{-3} has been reported in (Conlon *et al.*, 2000) (due to the effect of substitution on the lattice parameter of solid solution it is only marginally larger than that of pure Al). The $\delta_{Al-Al_2Cu} = -0.46 \pm 0.03 \times 10^{-6}$ calculated from the tomograms suggests a density of $\rho_{Al_2Cu} \approx 3.75 \pm 0.05$ g.cm^{-3} for the Al_2Cu particles which is higher than the values for $Al - 10$ wt% Cu ($\rho_{Al_2Cu} \approx 3$) given in the same reference.

The well defined Al_2Cu particles over the entire reconstructed volume can be rather easily labeled in the binarized image. Since the experiment has not been done in-situ, care had to be taken to image approximately the same sample region at different annealing times keeping in mind that the field of view is only $50\,\mu$m in this case. In addition the backtracking of the individual structures in the resulting volumes S1 and S2 before and after annealing has been hampered due to the drastic structural changes that the Cu particles had undergone. A flavor of that is given in figure 19. It is easier to compare S2 and S3 in terms of particle shapes. On figure 19 (b) an arrow marks a dendrite that disappears after further annealing for 12 hours (figure 19 (c)). These and other features may be quantitatively determined by particle analysis on the three volumes.

Among the parameters of relevance for the study of the annealing process, the volume fraction of the donor particles, their interface area, number and size are of particular importance. For the Al-Cu alloy similarly to the previously discussed Al-Si they have been evaluated with ImageJ, particularly with the 3Dparam plugin by L.Salvo (Salvo, 2005). The results are summarized in Table 2. Parameters a, b and c stand for the sides of the parallel prism having the

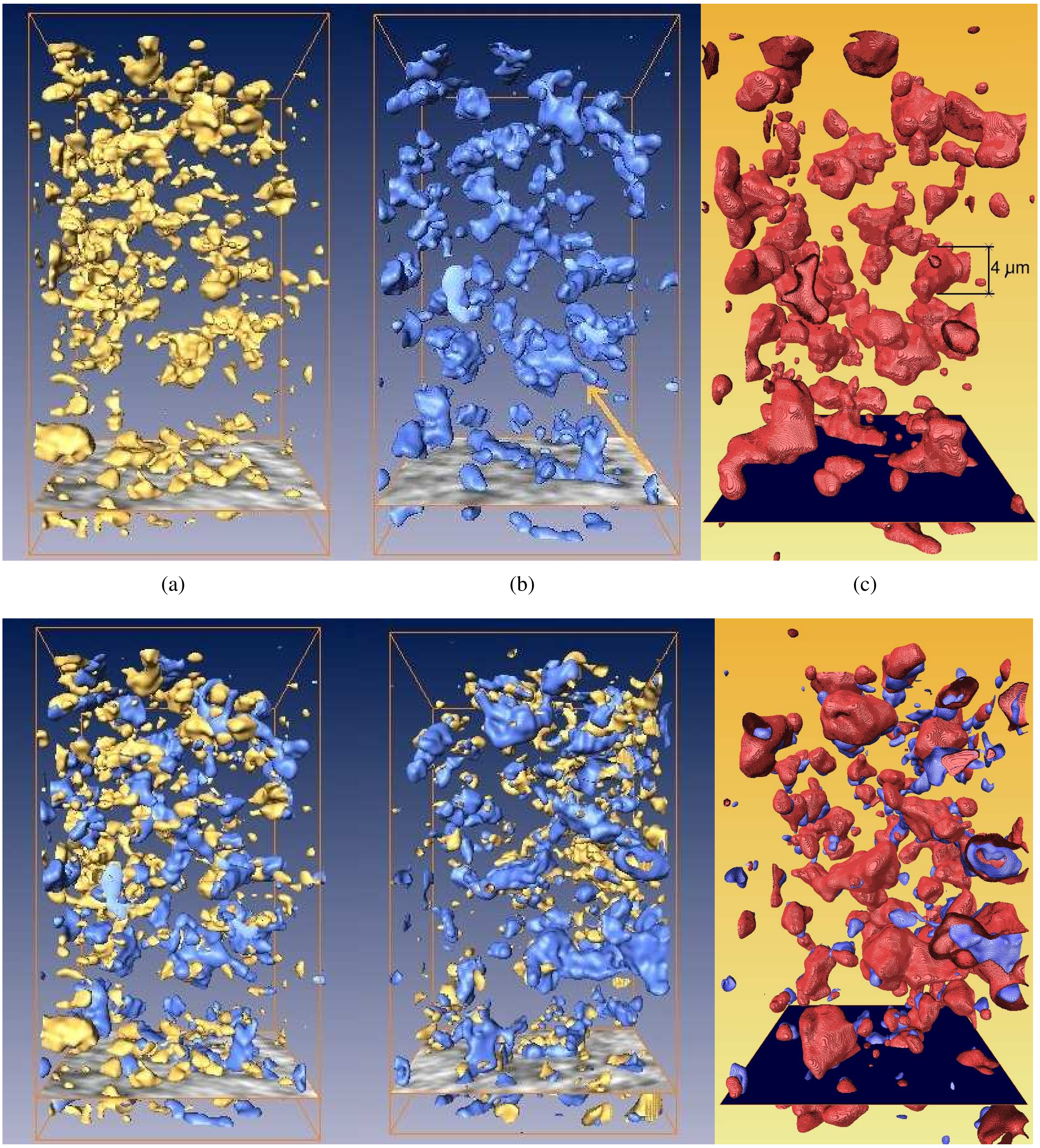

(a) (b) (c)

(d) (e) (f)

FIGURE 19. Three sub-volumes (each of dimensions $544 \times 540 \times 960$ pixels) of the same sample region for the Al-Cu sample in its initial state S1 (a) and after 12 hours S2 (b) and 24 hours S3 (c) of annealing. In (d) the superposition of S1 and S2 after finding the identical region for both volumes. For a different orientation the superposition of S1-S2 (e) and S2-S3 (f) are also shown.

	S1 - initial		S2 - 12 h		S3 - 24 h	
mean quantifiers	value	dispersion [%]	value	dispersion [%]	value	dispersion [%]
volume $[\mu m^3]$	3.13	257	11.65	247	18.6	224
surface $[\mu m^2]$	9.9	199	25	177	30.49	167
sphericity	0.8	16	0.77	18	0.84	13
a $[\mu m]$	0.76	87	1.26	86	1.29	90
b $[\mu m]$	0.45	82	0.74	78	0.82	78
c $[\mu m]$	0.32	74	0.53	74	0.64	74
a/b	1.63	32	1.61	23	1.48	30
a/c	2.2	34	2.28	34	1.85	34
b/c	1.35	20	1.4	30	1.26	16
global quantifiers						
surface sum $[\mu m^2]$	2215		2405		2195	
number of particles	222		96		72	

TABLE 2. The parameters extracted for all the three steps in the annealing process of the Al-Cu alloy.

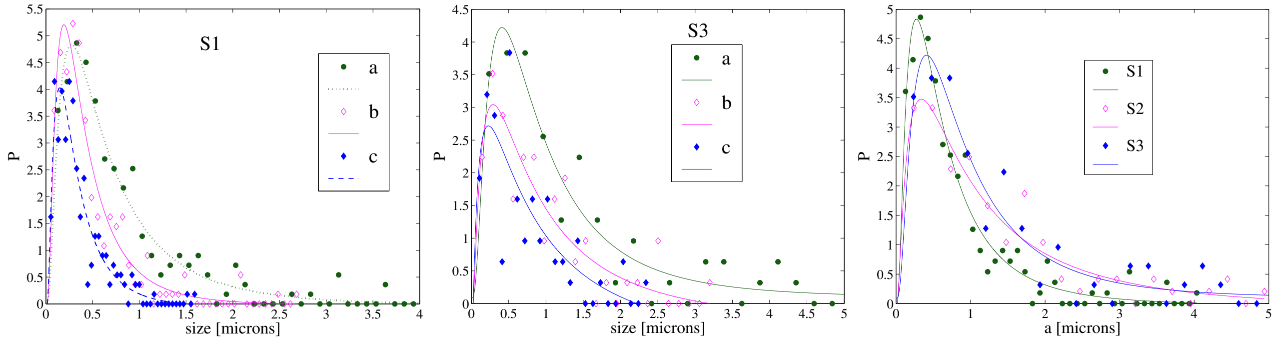

(a) (b) (c)

FIGURE 20. Distribution of the major, intermediate and minor diameters of particles in S1 (a) and S3 (b) and the evolution during annealing of the distribution of the major diameter (c). The curves are lognormal fits of the corresponding data.

same moment of inertia as the particle. We will refer to the major side a as the particle size or its major diameter. The sphericity of the particle in terms of its volume V and surface S is obtained as $6V\sqrt{\frac{\pi}{S^3}}$. The distributions of a, b and c are shown in figure 20, respectively for the initial state (a) and the final state (b) . The distributions shown are relative to the mean value of the given parameter $\frac{P(a)}{\langle a \rangle}$. The major diameter distribution as a function of annealing stage (figure 20 (c)) changes its shape and peak position. For the sample after 24 h of annealing we observe that the peak position is shifted, as expected, toward bigger particle sizes from 0.27 in S1 to $0.48\,\mu$m in S2. In the meantime the lognormal fitting function is narrower for the S3 stage than for S1 and S2. Also of interest is the behavior of the ratio of the major and minor particle diameter a/c in figure 21. While the peak of the distribution changes with annealing towards smaller ratios between a and c meaning that particles would get rounder, the mean value behaves differently. In accordance with the FWHM of the distributions the mean ratio

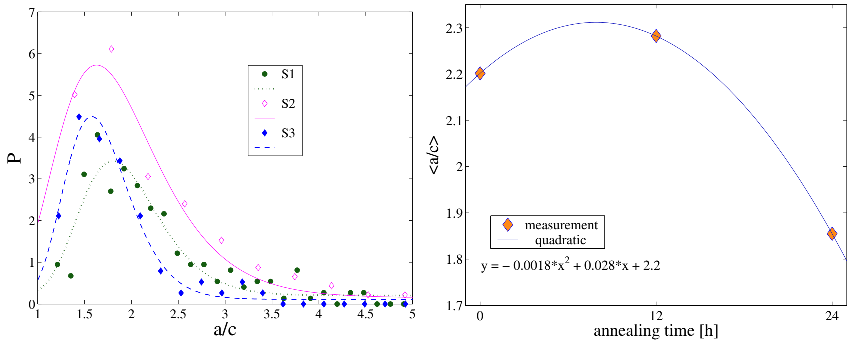

(a) (b)

FIGURE 21. Distribution of the major- to minor- particle diameter ratio a/c for the three instances during annealing (a). The curves are fitted with lognormal probability distribution functions. The time evolution of a/c (b) is fitted using a quadratic fit.

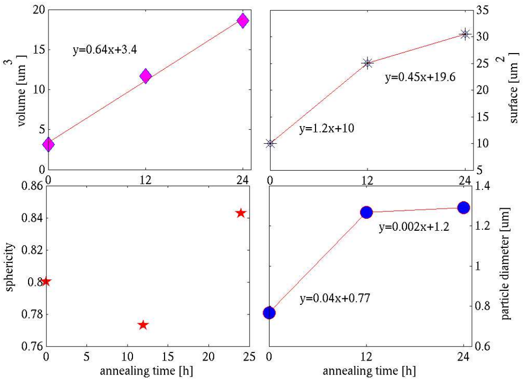

FIGURE 22. From left to right and from top to bottom the time evolution of the particle mean volume, surface, sphericity and main particle diameter.

a/c has a peak for the stage at $12\,h$ of annealing. The quadratic fit in figure 21 (b) hints at a possible peak with the explanation that particles in the first step become less symmetric/round as a consequence of joining each other. After this intermediate step they again tend towards the smallest moments of inertia and the ratio a/c becomes smaller. This reasoning is sustained by the measured evolution of the mean sphericity, shown in figure 22, which is minimal for S2 and maximal for S3. To quantitatively and precisely describe the particle behavior more data points would be required by recording more often the 3D structure of the sample during the annealing either in-situ or ex-situ with shorter repetition times between the scans. In complete agreement with the general course of annealing are the mean values of parameters in the three volumes. They however represent only a volume with few particles (after eliminating the particles on the border there are 222 in S1, 96 in S2 and 72 in S3 left). The mean volume, surface area and diameter increase during the annealing (see figure 22).

3. Conclusions and perspectives of the experimental method

The experiments on tailored much coarser microstructures (Conlon *et al.*, 2000) undergoing an isothermal heating show that in the early stages the distribution of average particle diameter peaks at the value of $1 - 5\,\mu$m. For the general purpose of understanding the process of the coalescence of coarse particles at elevated temperatures this kind of experiments are interesting and justify our experiments carried out at improved spatial resolution compared to earlier work. In the experiments presented here the annealing time between the initial and the consecutive stages was too long to gradually follow the shape transformation of the particles or even evaluate their growth law. One can still clearly see on the three-dimensional renderings and the concentration profiles that the same region of the material can be backtracked. The shape transformation is more obvious when comparing the later two stages of annealing and although its precise determination is out of the scope of this work the important message is the feasibility of such kind of experiment at sub-micrometer resolution. Our first results open the way to study other transformations at fine scale like damage induced stress in fine scale microstructures.

Conclusions and perspectives

In the framework of this thesis an innovative acquisition scheme for fast tomographic imaging has been implemented, as well as the first three-dimensional phase-contrast tomograms have been acquired with a new focusing x-ray setup. The fast acquisition has been implemented to be able to perform the first extensive study of the coarsening behavior of liquid foams, whereas the magnified tomography has been applied to high resolution studies of aluminum alloys. As these two fields require separate research, the document was thematically divided into two parts.

I.

The first part is devoted to the technical aspects of the tomographic technique, particularly at the ESRF beamline ID19, and the application of the new acquisition scheme to the imaging of liquid foams. We have improved the temporal resolution and field of view of the setup, which allowed to obtain for the first time experimental data with good statistics on three dimensional liquid foams.

The two chapters preceding the implementation and application of fast tomography provide the most essential background on the physical principles used in the following. In **Chapter 2** a brief summary of the image formation theory in the Fresnel regime was given. Phase retrieval methods to extract the quantitative information contained in the propagation images have also been reviewed. An iterative method based on the Gerchberg-Saxton algorithm is proposed for multiple intensity measurements and a curved wavefront with abberations. A common paper (Guigay *et al.*, 2004) on the use of the “partial Talbot effect” as a convenient method for coherence measurement of the synchrotron beam, is given in appendix of this Chapter. This effect is further exploited to characterize the wavefront delivered by the focusing optics.

Chapter 3 describes the tomographic acquisition scheme at the ID19 beamline. Its initial state, essentially sequential, was not satisfactory from the point of view of efficiency and consequently of speed. The high flux of 3rd generation synchrotron beams allows for short exposure times and fast acquisition of radiographic projections. However, as described here in detail, the transition from individual projections to tomography involves a rather complex communication network between the sample stage, the camera and the master software. The network was redesigned and the new scheme practically implemented on the beamline. It assures parallelization of the tomographic procedure to its maximal extend.

Tests have been performed in order to understand the effect of each important parameter such as the exposure time, the number of projections, the scanning mode and last, but not least, the detector itself. It was found that the optimal configuration for our application consists of the (ESRF developed) FReLoN 2k14 detector in Frame Transfer Mode. In spite of the DALSA camera being faster, the choice was made based on the overall evaluation of speed to image quality and the required field of view. Without significant decrease in image quality with the current flux at the ESRF, the exposure time can be kept at the minimum that the detector allows and the number of views may be adjusted in such a way as to meet the requirements on the total scanning time. However decreasing this latter to less than one quarter of the total number of pixels (perpendicular to the rotation axis) in the reconstructed image will increase the noise, particularly at the periphery of the slice.

Such an optimization is indispensable for a successful experiment requiring non-standard acquisition mode. The imaging of any evolving system implies complications. Let us recall that the complete lifetime of the "Dreft" washing-up liquid foam, presented in chapter 4, was approximately equal to the usual scanning time at ID19 a couple of years ago. The change was gradual and the Fasttomo device server described in chapter 3 was one of the ultimate units that have been implemented as part of the present work. The mentioned Dreft foam could now be followed in three dimensions with a time interval of less than two minutes between scans and an image quality sufficient for the segmentation. It was an important point to access the three dimensional structure of several fast evolving foams.

Chapter 4 describes the image analysis on the foam data sets: i.e. the segmentation of foam images and labeling of individual bubbles. It is not a trivial problem and much effort has been put in it by different research groups, including our collaborators from Rennes (Lambert *et al.*, 2005) who developed the 'Cluster Split Convex' method that has been successfully applied to our images. For very dry foams, where only the vertex is visible in the images, a second method, based on weighted distance constraints combined with a watershed method, has been introduced.

The presentation of experimental results starts with the 'easy to measure' liquid fraction as a function of time and foam depth. Its variation for two different foams is shown. In the last section we show that we can access the distributions of a foam that is very young, far from the scaling state, and compare them directly to those obtained from a shaving foam, a candidate for reaching the scaling state during the experiment. In the first case, the distributions of mean parameters were unstable during the whole period of observation. We have to keep in mind that the period of observation was approximately equivalent to the lifetime of this foam. This underlines the notion in foams unlike for grains of a long transition period before reaching the scaling state, hindering the experimental verification of its existence. As a validation of the hypothesis that the shaving foam is in the scaling state, the distributions of the relative parameters were found to be stable and in good agreement with the extensive Potts model simulations of three-dimensional foams that have been developed by (Thomas *et al.*, 2006) who provided the data for the charts in which the comparisons are given. Based on the plots of the second order moments of the mean number of faces a possible time correlation was proposed between the shaving foam and the Potts model simulations. The growth rate measurements resulted in a zero intercept at the value of $f_0 = 14.7$. This deviates from the value given in simulations but is in accordance with the formula proposed by Glazier (Glazier, 1993) that relates f_0 to the number of faces and its second moments.

The outlook is relatively well defined since only a part of the large amount of data produced by the fast scanning experiments could be processed so far. Particularly promising appears the Dreft foam that was followed during a long time. This foam (see also figure 15) has several ten thousands of bubbles in the imaged volume in its initial state and ends with ~ 1000 bubbles at a liquid fraction below 0.5 %. This foam gives similar growth rate curves, but a higher number of average faces as compared to the shaving foam. The latter point was the main discrepancy between the simulations and the experimental results from a shaving foam.

The data sets which are now available for various types of foams will allow to do intercorrelations of relevant parameters for different foams.

The fast acquisition is now a standard acquisition modality on the ID19 beamline. It has already been applied to other in-situ studies such as hardening of cement and studies of metal alloys at high temperature. It is expected to be an important asset of the facility in the future.

II.

In the second part of the thesis we have described the Kirkpatrick-Baez focusing system and its first applications (Mokso *et al.*, 2006). In terms of stability and image quality the developments presented in this part of the thesis provide valuable evidence for the feasibility of phase contrast tomography in magnifying geometry.

Since the ultimate goal of this research is to improve the spatial resolution in tomography for applications, four different contributions are important for the characterization of the imaging system:

- the thermal stability and mechanical imperfections
- effects of distortion induced by mirror imperfections
- effects of refraction on sample borders
- phase propagation effects with the influence of the magnification

Each of these factors must be understood if one desires to reach sub-micrometer spatial resolution in the reconstructed volumes.

Chapter 5 presents the instrumentation used for imaging in projection geometry. Two mirrors in crossed-geometry provide a two-dimensional focal spot of the dimensions $\simeq 90 \times 90$ nm^2 (41 nm in vertical direction with a new multilayer coated mirror). The conclusion on the first of the four important parameters, the thermal stability, is that we can reach a temperature stability better than 0.01 K on the mirror, but it is very difficult to do so without undesirable secondary effects on the mechanics introduced by the thermal regulation elements. A better material choice is thus suggested (invar benders) and we conclude that the requirements are very strict on the thermal stability of the whole experimental hutch in which nano-focusing experiments are to be performed. For imaging, the second effect is important and discussed in the last section of this chapter. The abberations of the wavefront due to mirror figure errors are measured using two dimensional grid images and the fractional Talbot effect. The information obtained this way is then used to 'undistort' each projection of the tomographic scan. Finally the third effect discussed in this last section of Chapter 5 is the wave effect on the sample boundary where abrupt phase variation occurs. The origin of strong ring artifacts in the reconstructed images of samples that are smaller than the field of view at magnifications used in this study (sample diameter of 50 to $100\,\mu$m) has been explained. To prevent their occurance we propose to work in so-called local tomography mode when the sample lateral dimension exceeds the field of view. Images obtained this way are free of the 'lens-effect' due to refraction on the sample boundaries which is at the origin of the ring artifacts. Moreover this tomographic mode is much better suited to practical applications because it does not require sophisticated sample preparation.

The adaptation of the phase retrieval methods to the new geometry is introduced in this chapter as well.

Chapter 6 caries two important messages.

Firstly the comparison of the performance of different phase retrieval methods applied on real images from the Kirkpatrick-Baez system. Due to the relatively large focal plane-to-sample distance (equivalent to the defocus distance in the case of the focusing system) the reconstruction based on “edge enhancement” does not work. Small defocus distances would mean an extremely small field of view and strong effects of mirror distortions; therefore phase retrieval is needed. It was found that the best images are obtained using the paraboloid method in the case of too strong absorption and phase contrast. We applied it on the Aluminum-Silicon sample to obtain images of the typical three-dimensional distribution of the Si particles in the Al matrix. It was also shown on an image that the iterative method introduced in Chapter 2 is promising but it should be coupled in the future to a two-dimensional phase unwrapping procedure. Varying the magnification implies a variable frequency content in the projections and this takes such an effect as if for the highest spatial frequency only one distance is available. For a homogenous sample a partial solution to this is the coupling of phase and attenuation as it was shown in the case of the Al-Cu sample.

Secondly, on the Al-Si sample the quantitative nature of phase contrast tomography in local mode has been demonstrated by retrieving the relative densities of the two main components Si and Al in the studied volume. Furthermore the chemical form of the third (iron rich) component was determined. All this at a spatial resolution of 290 nm seldomly achieved earlier in the range of hard x-ray energies ($\sim$ 20 keV) that we have been working with.

The above example illustrates the feasibility of sub-micrometer resolution tomography on bulky samples using a divergent beam and phase retrieval.

As for the outlook, the second example in the last Chapter indicates the possibilities of the combined use of sub-micrometer spatial resolution and high photon flux. The annealing of the Aluminum-Copper sample has been followed ex-situ at three stages. Particle analysis was performed and showed results in accordance with the expected behavior of the alloy undergoing the annealing process. More stages of the annealing process can be imaged, moreover the storage ring filling mode during the experiment gives $\approx 1/3$ of the flux that is available at ESRF. It brings us to the conclusion that the high flux in this configuration could be exploited for shortening the acquisition time and studying dynamic processes at resolutions superior to any other three-dimensional imaging technique for hard x-rays. Such studies will benefit from both aspects, spatial and temporal resolutions described in this work.

Résumé de la thèse

Les techniques d'imagerie sont utilisées, en science des matériaux, comme méthodes de caractérisation non destructives. Elles emploient des sondes diverses pour interagir avec la matière et révéler les variations locales des propriétés des matériaux étudiés (atténuation, densité électronique etc.). Parmi ces techniques la tomographie au rayons X ouvre la voie à la caractérisation tridimensionelle. Les deux sujets principaux de cette thèse sont l'amélioration des résolutions temporelle et spatiale de la tomographie aux rayons X. Ces deux aspects sont traités séparement. Dans la premiére partie, la description d'une nouvelle méthode de tomographie rapide et l'application aux mousses liquides est presentée. La deuxième partie est consacrée a l'étude d'une système optique pour la focalisation d'un faisceau de rayons X durs et son utilisation pour produire des images tomographiques avec une résolution spatiale de l'ordre de quelques centaines de nanometres.

Le travail ici présenté a eté réalisé à l'Installation Européenne de Rayonnement Synchrotron (ESRF) à Grenoble. Le rayonnement synchrotron offre des propriétés particuliérement intéressantes pour la micro- et nano-tomographie, notamment un *flux de photons utiles élevé*, nécessaire pour la tomographie rapide et la *cohérence transverse* du faisceau, permettant l'imagerie de phase aux rayons X, et utilisée pour la tomographie par projection dans la deuxième partie de ce document.

Amélioration de la résolution temporelle en tomographie

Les systèmes qui évoluent dans le temps, posent des problèmes quand on veut étudier leur structure tridimensionelle. Pour obtenir un tomogramme d'un objet donné, la condition est que cet objet ne change pas sa structure pendant l'acquisition du scan. Avec les sources de rayons X de laboratoires la durée d'un scan tomographique avec une résolution $\sim 10\,\mu$m est de quelques heures. Sur ID19, à l'ESRF, la même procédure est plus courte, grace au flux élevé de photons utiles des synchrotrons de troisième génération. Il y a deux ou trois années un scan 'rapide' durait typiquement une demi-heure à ID19. C'est encore trop long pour l'étude des systèmes tels que les mousses liquides, qui changent considérablement pendant ce temps. La raison principale était la sequentialité de la procédure de scan tomographique et la communication lente entre les unités individuelles comprenant le système de détection, la système de translation et de rotation et finalement aussi le logiciel de contrôle. La situation n'était pas satisfaisante et il fallait restructurer la synchronisation de ce dispositif expérimental.

L'optimisation du dispositif pour la tomographie rapide.

Un nouvel élément, en forme de 'Device Server', a été introduit dans la schéma d'acquisition d'images. Le troisième Chapitre donne une description de ce 'Device server' de tomographie rapide. Sa fonction est de communiquer avec les moteurs actifs pendant un scan (la rotation et une translation). En parallèle, un autre Device server pour le détecteur a été introduit, par la groupe informatique de l'ESRF. Avec ces deux nouveaux éléments, le scan et devenu plus rapide, grâce à une gestion plus efficace des differents éléments. Le logiciel de contrôle, au lieu de 'parler' aux moteurs et à la camera, a maintenant pour fonction de distribuer les instructions aux deux 'Device servers'. Une fois les instructions données, les deux Device servers sont autonomes et peuvent contrôler les moteurs ou le détecteur en parall\'{e}le. Pour comparer le protocole initial de communication avec celui decrit ici, voir le Diagramme 3.3.3 qui répresente le cours des signaux pendant la tomographie.

Le nouveau 'Device server' de tomographie rapide est un logiciel écrit en C par nos collaborateurs, Carlos Medrano et Imma Plaza de l'Université de Zaragoza. Ma contribution à ce travail a consisté à définir le Device server, le tester et mettre au point les différentes versions pour arriver à installer la version finale avec le fonctionnement désiré. Le Device server nous permet de travailler dans trois modes différents:

- le scan **'pas** à **pas'** se divise en deux sous-modes. Si le premier mode est séléctionné, au début du scan, le détecteur prend une image, suivi par le mouvement de la rotation. Dès que la rotation est arrivée à la position demandée, la prochaine image peut être prise. Un deuxième mode, que nous appelons 'quasi-continu', se distingue par la prise de la prochaine image, sans attendre la fin du mouvement de la rotation.
- le **'timescan'** prend les images sans bouger la rotation
- la scan **continu** lance la rotation avec une vitesse constante qui est detérminée au début du processus. La camera prend les images successives pendant le mouvement de la rotation.

Les différents modes ont été testés de façon quantitative, pour trouver la meilleure configuration des paramètres de système. L'effet du mode continu sur la qualité d'image est faible. Ayant choisi ce mode pour l'acquisition rapide, il est important de connaître l'effet d'autres paramètres, comme le temps de pose et le nombre des vues. Pour séparer les deux, plusieurs tests ont été éffectués et les résultats résumés dans les tableaux 4 et 5 du Chapitre 3. Nous avons trouvé que la meilleure configuration est de laisser le temps de pose au minimum (dicté par le détecteur, 60 ms pour la FreLoN 2k14) et de varier le nombre de projections en fonction du champ de vue et du temps total de scan desiré. Les études montrent qu'une réduction du nombres de vues au dessous d'un quart du nombre de pixels en direction latérale introduira un bruit fort qui peut êmpécher l'interprétation des images.

Trois caméras ont été testées, la camera commerciale DALSA, et deux caméras FreLoN developpées à l'ESRF. Les deux caméras FreLoN différent essentiellement en termes de vitesse. Nous avons surtout utilisé lanouvelle, plus rapide FreLoN 2k14. La DALSA est une camera encore plus rapide que la FreLoN, mais la FreLoN 2k14 donne des images de plus haute qualité pour le même temps de pose et un plus grand nombre de pixels. En conséquence, la camera FreLoN 2k14 a été choisie pour l'imagerie des mousses liquides décrite dans le Chapitre 4.

Pour conclure, un schéma d'acquisition parallèle des images en tomographie a été implementé sur la ligne de lumière ID19 de l'ESRF. Cette méthode est devenue une mèthode de routine qui a été utilisée depuis pour plusieurs applications. Un scan de moins d'une demi-minute est faisable en routine avec le mode continu du Device Server.

L'imagerie des mousses liquides.

Avec le nouveau dispositif de tomographie rapide, nous avons developpé une application qu'il n'était pas possible de considérer avec la vitesse de tomographie antérieure aux études décrites dans ce Chapitre. Les mousses liquides sont un système complexe, qui évolue relativement vite. Jusqu'a présent, il n'existait pas d'études satisfaisantes des mousses en 3D. Pour la première fois, nous avons pu suivre l'évolution des mousses liquides en 3D avec un nombre de bulles suffisant pour obtenir une bonne statistique.

Bien que les images soient d'une très bonne qualité, la "labélisation" des bulles individuelles dans une mousse n'est pas une tâche simple. La première partie de ce chapitre décrit deux méthodes de labélisation.

La première est basée sur la procédure de 'ClusterSplitConvex' integré dans le logiciel Aphelion, que nous avons utilisé. Cette methode marche bien sur les mousses pas trop sèches.

La deuxième methode calcule les distances ponderées des centres des bulles et ensuite utilise cette information comme entrée pour une methode de partage des eaux ('Watershed'). Cette methode a été développée pour les mousses très sèches. Mais il y a encore des incertitudes sur certains aspects de cette méthode, qui a tendance à ne pas reconnaître certaines bulles. Pour cela, nous avons effectué plusieurs tests, mais pour les trois mousses décrites dans ce document nous avons utilisé la première methode, plus fiable.

Une caractéristique des mousses, simple à obtenir à partir des images tomographiques, est la fraction liquide. Les évolutions temporelles et spatiales pour deux mousses de proprietés différentes sont données sur les Figures 4.2.10-12. Ces deux mousses ont été suivies pendant leur évolution en termes de caractéristiques geométriques et topologiques. La première d'entres-elles est une mousse de liquide vaisselle 'Dreft'. Cette mousse évolue très vite, avec une vie moyenne de moins d'une heure. Une évolution aussi rapide demande une acquisition de quelques secondes. Pour cette mousse nous avons pris 400 images de dimensions 2048×1024 pixels, avec une temp de pose de 60 ms. Au final, cela donne ~ 24 s de temps total pour un scan tomographique. Aprés la "labelisation", nous avons pu accéder aux distributions des paramètres pendant l'évolution de cette mousse. Les distributions comme le volume et la surface moyens par rapport au nombre de faces des bulles $\frac{<V_f>}{<V>}$, $\frac{<S_f>}{<S>}$, accuse une variation marquante entres les images consécutives. Cela est une indication que cette mousse n'est pas dans un état particulier, dit 'invariant d'échelle' dans lequel les paramètres rélatifs ne changent pas. Cette mousse 'Dreft' est un très bon exemple pour montrer qu'on peut obtenir ces caractéristiques importantes en 3D d'une mousse évoluant aussi vite. Elle est aussi un bon 'contre-exemple' de mousses dans l'état invariant d'échelle. L'observation de l'évolution, très marqué des paramètres relatives pour une mousse jeune, nous servira pour la comparaison avec une autre mousse ayant vieilli beaucoup plus longtemps.

La mousse à raser (figure 23) a été preparée 24 heures avant le début de l'experience même et a été suivie pendant les 5 jours de cette experience. Les distributions de volume et de surface moyens par rapport au nombre de faces sont très stables pour cette mousse. Leur forme peut etre comparée au résultats de 'Potts model' simulations, qui utilisent les méthodes Monte Carlo.

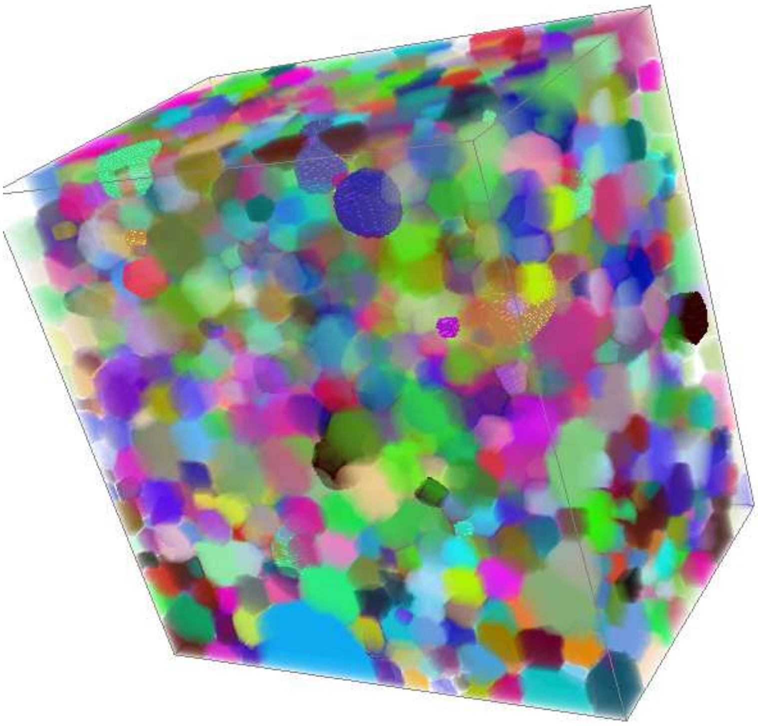

FIGURE 23. Une sousvolume de la mousse a raser.

Ces résultats ont été mis à notre disposition par les auteurs de (Thomas *et al.*, 2006). Ils ont produit ces simulations en parallèle à nos expériences. On trouve cette compariason dans l'image 4.2.27. La corrélation est bonne, surtout pour la distribution de surface. Dans la catégorie des paramètres de *validation* que la mousse se trouve dans l'état invariant d'échelle, nous avons montré que le volume, la surface et le diamètre moyens des bulles sont les functions $t^{3/2}$, t et $t^{1/2}$ (voir figure 4.2.28).

Une deuxième catégorie de caractéristiques des mousses inclut les volume, surface et diamètre des bulles normalisés par les paramètres moyens, $\frac{V}{<V>}$, $\frac{S}{<S>}$ et $\frac{V^{1/3}}{<V^{1/3}>}$. Ces distributions, pour des temps différents pendant l'évolution de la mousses à raser, sont aussi stables et en très bon accord avec les simulations de Potts model.

Finalement le taux de croissance du volume des bulles a été evalué en Figure 4.2.31. La valeur de f_0, oú la courbe croise le zéro est 14.7, ce qui est différent des résultats obtenu à l'aide des Potts model simulations ($f_0 = 16.7$), mais plus proche des résultats des simulations par Glazier (Glazier, 1993).

Nous pouvons récapituler que la stabilité des distributions suggère que la mousse à raser est très proche d'un régime invariant d'échelle, qui n'a pas encore été démontré experimentalement pour les mousses tri-dimensionelles. Nous avons pu étudier la dynamique de mousses differentes grâce à la nouvelle technique de tomographie rapide.

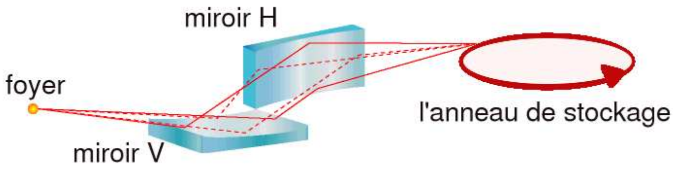

FIGURE 24. Le principe d'une optique Kirkpatrick-Baez.

La tomographie aux rayons X durs, à résolution spatiale sub-micrométrique

L'amélioration de la résolution spatiale motivée par des nombreuses applications est certainement un des moteurs pour l'innovation des techniques d'imagerie. Cela est particulièrement vrai pour les techniques tri-dimensionelles, comme la tomographie aux rayons X. Avec le rayonnement synchrotron, la limite de résolution a été poussée, pendant la dernière décade, vers la valeur d'environ $1\ \mu$m. Pour un faisceau synchrotron parallèle, cette limite est imposée par la physique de détection des rayons X, particulierement par le scintillateur. Avec une modification de géometrie de faisceau, on peut se détacher de cette limite. Par un dispositif dit de Kirkpatrick-Baez cette modification a été efféctuée, et le faisceau divergent utilisé pour l'imagerie 3D décrit dans (Mokso *et al.*, 2006).

Le chemin vers la tomographie agrandie.

La Figure 24 montre deux miroirs focalisant le faisceau de rayons X parallèle pour produire un micro-foyer d'un diamètre d'environ 90 nm.

Un faisceau divergent est obtenu. L'element focalisant en direction verticale, est une multicouche qui, par rapport à un miroir simple, donne une champ de vue plus important dans cette direction. Les deux miroirs sont courbés par un système mécanique dans une forme elliptique pour obtenir une image réduite de la source originale.

Notre but est d'arriver aux résolutions spatiales de cent nanometres ou dessous. Cela impose des contraintes très imporantes sur la stabilité du foyer. Celui-ci est influencé par les vibrations mécaniques et surtout par les variations de température. Le matériau des miroirs est le Silicium, la construction autour est en acier. Les coefficients de dilatation différents pour ces deux matériaux sont à l'origine d'un mouvement du foyer en direction latérale mais aussi en direction paralelle au faisceau quand la courbure du miroir varie quand la température change.

Le Chapitre 5 contient une section ou tous les essais de thermalisation du système sont décrits. La conclusion peut etre formulée dans le sens que nous arrivons à maintenir la température d'un miroir constante dans une gamme de moins de 10 mK, mais le système de régulation va toujours introduire des instabilités du système KB entier liees aux gradients thermiques.. Deux solutions s'imposent: faire un choix de matereau plus approprié (mechanique en invar) et avoir une thermalisation aussi bonne que possible du laboratoire oú on veut faire l'imagerie avec une résolution nanométrique. Les petites variations en température peuvent être corrigées par un système de régulation de température directement sur la boite du KB. La stabilité thermique est importante pour la l'imagerie par fluorescence avec le KB ou l'échantillon est placé au foyer, mais aussi pour la tomographie agrandie oú l'échantillon est placé en dehors du foyer.

Si l'échantillon est placé à une distance z_s du foyer dans le faisceau divergent, et le détecteur à une distance z_d de l'échantillon ($z_d \gg z_s$), on obtient sur le détecteur une image agrandie de l'échantillon. Dans le cas général, c'est une image de phase et d'amplitude avec une distance de défocalisation effective

$$D = \frac{z_s . z_d}{z_s + z_d}$$

et un agrandissement

$$M = \frac{z_s + z_d}{z_s}$$

En évitant de placer l'échantillon trop proche du foyer ou les effets des distortions des miroirs sont grands et le champ de vue petit, la distance D devient relativement grande. On se trouve dans le régime de diffraction de Fresnel et, pour l'interprétation des images obtenues avec le KB, on a besoin utiliser des méthodes de reconstruction de la phase.

Avant la reconstruction, il est nécessaire de corriger la distortion introduite dans les images par les miroirs. Une méthode basée sur la mesure du front d'onde utilisant une grille bidimensionelle est developpée. Les écarts sur la position des maxima et minima mesurés dans l'image de cette grille peuvent etre rapportés aux les abbèrations du front d'onde produites par les miroirs. Nous avons utilisé cette information pour éliminer la distorsion de chaque projection dans un scan tomographique.

Dans le cas d'un objet de dimensions latérales $50 - 100\,\mu$m, donc plus petit que le champ de vue typique pour nos scans, on a observé une effet de réfraction important sur les bords de cet échantillon. Si une particule de poussière ou une imperfection est présente sur la surface d'un miroir, l'image de cet objet parasite va apparaître sur la radiographie de l'échantillon. Si l'image de cette poussière coïncide avec le bord de l'échantillon, et en conséquence de la réfraction, la position de son image n'est pas la même que sur une radiographie sans l'échantillon. Si on utilise la correction habituelle de champ plat en divisant la radiographie avec l'échantillon pixel par pixel par la projection sans l'échantillon, l'image de la poussière ne sera pas eliminée et introduira des artefacts sous forme de cercles (ring artefacts) dans la reconstruction tomographique. Une solution très bien adaptée à notre système est d'employer la tomographie locale, c'est-à-dire, de placer dans le faisceau un échantillon de diamètre plus grand que le champ de vue. Les effets de bord sont dans ce cas éliminés, parce que il n'y a pas de bords dans l'image. C'est une solution bien pratique, car la fabrication des échantillons d'environs 1 mm en diamètre est beaucoup plus facile que pour ceux de diamètre de $50\,\mu$m.

Faisant ces corrections on a preparé les projections pour la reconstruction de la phase. Le premier pas a été de modifier les méthodes de faisceau parallèle décrit par (Cloetens, 1999), pour l'adapter à notre nouvelle géometrie. Le choix de la méthode la mieux adaptée à un type d'objet en particulier est le sujet du Chapitre 6.

Les applications de la tomographie en projection.

Nous avons traité deux types d'échantillons dans cette étude. Les deux sont des alliages d'aluminum, mais avec un contraste d'absorption different. Le premier est un alliage Aluminum - Silicium ($Al - Si$) Sur cet echantillon, des méthodes différentes de reconstruction de phase (listé dans le Chapitre 2) ont été testées. Parmi les methodes de *phase lentement variable* (2.2.13), de *l'objet faible* (2.2.15) et la *méthode paraboloide,* (2.2.18) la mieux adaptée aux images obtenues avec le system KB, est la méthode paraboloide. Cette méthode a été appliquée sur le $Al - Si$ pour obtenir les cartes de phase et ensuite les tomogrammes. La résolution spatiale a été mesurée sur les tomogrammes bidiminensioneles, avec un résultat de 290 nm. Cinq distances $z_s = \{47.5;\ 67.5;\ 127.5;\ 187.5;\ 267.5\}$ mm ont servi pour obtenir les cartes de phase. La plus petite de ces distances correspond à un agrandissement $M = 144$, donc à une taille de pixel effective de 90 nm (utilisant le detecteur avec l'optique de 7.46 μm taille de pixel).

Une mesure quantitative des trois composants, Al, Si, et $Al_xFe_ySi_z$ présents dans le volume reconstruit a servi comme preuve que les résultats sont interprétables, pas seulement de facon qualitative, mais aussi quantitative. La densité mesurée du composant avec Fer, correspond à Al_5FeSi, ce qui n'etait pas connu, mais qui est l'intermetallique le plus souvent présente dans ce type d'alliage.

L'autre alliage étudié pendant un processus de recuit, était le un alliage Aluminum - Cuivre (Al_2Cu). La méthode donnant les meilleurs résultats pour ce type d'échantillon (la différence en absorption entre Al et Cu est autent plus important qu'entre Al et Si) est basée sur l'approche de l'objet faible. Pour améliorer la qualité des tomogrammes nous avons du supprimer les fréquences spatiales les plus hautes de l'image qui a été prise au agrandissement le plus élevé. C'est une conséquence de la géometrie du système. La variation de la distance de défocalisation est liée à la variation de l'agrandissement. Cela implique que, pour la défocalisation la plus petite, la valeur de l'agrandissement est le plus important, et les fréquences spatiales les plus hautes, contenues dans cette projection, ne sont pas présentes dans les autres projections prises avec un agrandissement plus faible. Pour la reconstruction de phase on a besoin au moins de deux projections contenant les mêmes fréquences. Pour cet alliage nous avons aussi modifié la méthode de l'objet faible, en introduisant le rapport entre les parties réelles β (absorption) , et imaginaire δ (réfraction) de l'indice de réfraction complexe, $n = 1 - \delta - i\beta$.

Cet échantillon a été suivi pendant 24 heures de traitement thermique. Les images ont été prises au temps de t_{init}, $t_{init} + 12$ et $t_{init} + 24$ heures. Nous avons retrouvé la même region dans les images 3D de ces trois séries (voir Figure 6.2.16) et comparé les distributions caractéristiques des particules. En bon accord avec les prévisions pour un échantillon thermiquement traité, les particules sont agrandies et le nombre de particules dans le même volume diminué. Cet exemple montre qu'il est possible de caracteriser les processus dynamiques avec une résolution spatiale très élevée. Ce dernier résultat ouvre les portes pour de nombreuses applications nouvelles.

La conclusion est que nous avons realisé un microscope au rayons X durs en géometrie de projection, ce qui permet d'explorer la structure intérieure des matériaux en 3D avec une résolution de 290 nm.

Appendix

.

.

Bibliography

Ablett, J. M., C. C. Kao, and A. Lunt, 2002, Rev. Sci. Inst. **73**(10), 3464.

Anastasio, M. A., D. Shi, F. D. Carlo, and X. Pan, 2003, Phys. Med. Biol. **49**, 121.

Aristov, V. V., A. A. Singirev, Y. A. Basov, and A. Y. Nikulin, 1986, in *AIP Conf. Proc.*, volume 147, p. 253.

Bartholomew, R. N., and R. M. Casagrande, 1957, Industrial and Engineering Chemistry **49**(3), 428.

Born, M., and E. Wolf, 1990, *Principles of Optics*, 7th edition (Pergamon press, Oxford).

Bracewell, R. N., and A. C. Riddle, 1967, Astrophysics J. **150**, 427.

Brakke, K., 1992, Exp. Math **1**, 141.

Burkhard, A., A. Prause, and J. A. Glazier, 1999, in *Proceedings of the 5th Experimental Chaos Conference Orlando, Florida*, edited by M. Ding, W. L. Ditta, L. M. Pecora, and M. L. Spano, pp. 427–436.

Cloetens, P., 1999, *Contribution to phase contrast imaging, reconstruction and tomography with hard synchrotron radiation*, Ph.D. diss., Vrije Universiteit, Brussel.

Cloetens, P., W. Ludwig, J. Baruchel, D. V. Dyck, J. V. Landuyt, J.-P. Guigay, and M. Schlenker, 1999, Appl. Phys. Lett. **75**, 2912.

Cloetens, P., M. Pateyron-Salome, J. Y. Byffiere, G. Peix, J. Baruchel, F. Peyrin, and M. Schlenker, 1997, J. Appl. Phys. **81**(9), 5878.

Conlon, K. T., E. Maire, D. S. Wilkinson, and H. Henein, 2000, Metall. Mater. Trans. A **31A**, 249.

Cormack, A., 1963, J. Appl. Phys. **34**, 2722.

Cormack, A., 1964, J. Appl. Phys. **35**, 2908.

Erko, A. I., 1990, J. XRay Sci. Technol. **2**, 297.

Faridani, A., K. Buglione, P. Huabsomboon, O. Iancu, and J. McGrath, 2001, Contemporary Mathematics: Radon Transforms and Tomography **278**, 29.

Faridani, A., E. L. Ritman, and K. T. Smith, 1992, SIAM J. Appl. Math. **52**(2), 459.

Feldkamp, L. A., L. C. Davis, and J. W. Kress, 1984, J. Opt. Soc.. **1**(6), 612.

Fienup, J. R., 1982, Applied optics **21**(15), 2758.

Fortes, M. A., 1986, J. Mat. Sci. **21**, 2509.

Gerchberg, R. W., and W. O. Saxton, 1972, Optik **35**, 237.

Glazier, J. A., 1993, Phys. Rev. Lett. **70**, 2170.

Glazier, J. A., and B. Prause, 2002, in *Proceedings of the Eurofoam Conference, Delft*, edited by P. Zitha (Verlag MIT, Bremen), p. 120.

Glazier, J. A., and J. Stavans, 1989, Phys. Rev. **A 40**(7398).

Gonatas, C., J. Leigh, A. Yodh, J. Glazier, and B. Prause, 1995, Phys. Rev. Lett. **75**, 573.

Goodman, J. W., 1988, *Introduction to Fourier optics*, Electrical engineering series (Mcgraw-Hill), second edition.

Guigay, J.-P., 1977, Optik **49**(1), 121.

Guigay, J.-P., S. Zabler, P. Cloetens, C. David, R. Mokso, and M. Schlenker, 2004, J. Synchrotron Rad. **11**(6), 476.

Gureyev, T. E., A. Pogany, D. M. Paganin, and S. W. Wilkins, 2004, Optics Communications **231**, 53.

Henke, B. L., 1981, in *AIP Conf. proceedings*, edited by B. L. Henke and D. T. Attwood, pp. 146–155.

Herman, G. T., 1980, *Image reconstruction from projections: the fundamentals of computerized tomography* (Academic Press, New York).

Hignette, O., P. Cloetens, G. Rostaing, P. Bernard, and C. Morawe, 2005, Rev. Sci. Instrum. **76**(6), 063709.

Hignette, O., A. K. Freund, and E. Chinchio, 1998, in *Proceedings of the SPIE Materials, Manufacturing, and Measurement for Synchrotron Radiation Mirrors*, edited by P. Takacs and T. W. Tonnessen, volume 3152, pp. 188–199.

Hignette, O., G. Rostaing, P. Cloetens, A. Rommeveaux, W. Ludwig, and A.Freud, 2001, in *Proc. SPIE*, volume 4499, pp. 105–116.

Hounsfield, G. N., 1972, *A method of and apparatus for examination of a body by radiation such as x-ray or gamma radiation*, Patent specification 1283915, The Patent Office.

Hrdy, J., 1998, J. Synchrotron Rad. **5**, 1206.

Hrdy, J., and D. P. Siddons, 1999, J. Synchrotron Rad. **6**, 973.

Hudec, R., L. Pina, A. Innemam, and L. Sveda, 2004, Nuclear Physics B **132**, 320.

Iida, A., and K. Hirano, 1996, Nuc. Inst. Meth. Phys. Res. B **114**, 149.

Jackson, J. D., 1975, *Classical electrodynamics*, second edition (John Willey and Sons, New York).

Jarre, A., C. Fuhse, C. Ollinger, J. Seeger, R. Tucoulou, and T. Salditt, 2005, Phys. Rev. Lett. **94**, 074801.

Kak, A. C., and M. Slaney, 1987, *Principles of computerized tomography* (IEEE Press).

Kang, H. C., J. Maser, G. B. Stephenson, C. Liu, R. Conley, A. T. Macrander, and S. Vogt, 2006, Phys. Rev. Lett. **96**, 127401.

Kenue, S. K., and J. F. Greenleaf, 1979, Ultrason. Imaging **1**, 232.

Kirkland, E. J., 1984, Ultramicroscopy **15**(3), 151.

Kirkpatrick, P., and A. V. Baez, 1948, J. Opt. Soc. Am. **38**(9), 766.

Koehler, S. A., H. A. Stone, M. P. Brenner, and J. Eggers, 1999, Langmuir **16**(15), 6327.

Kohn, F. G., 2003, J. Exp. Theor. Phys. **97**(1), 204.

Koren, G., F. Polack, and D. Joyeux, 1993, J. Opt. Soc. Am. A **10**(3), 423.

Krinsky, S., 1983, IEEE Transactions on Nuclear Science **30**(4), 3078.

Lambert, J., I. Cantat, R. Delannay, A. Renault, F. Graner, J. A. Glazier, I. Veretnikov, and P. Cloetens, 2005, Colloids and Surfaces A **263**, 295.

Li, Y., M. Yasa, O. Pelletier, C. R. Safinya, E. Caine, E. Hu, and P. Fernandez, 2003, Appl. Phys. Lett. **82**(15), 2538.

Ludwig, O., M. Dimichiel, L. Salvo, M. Suery, and P. Falus, 2005, Met. Mat. Trans. A **36A**(6), 1515.

Martin, T., and A. Koch, 2006, J. Synchrotron Rad. **13**, 180.

Mayo, S., T. Davis, T. Gureyev, P. Miller, D. Paganin, A. Pogany, A. Stevenson, and S. Wilkins, 2003, Optics Express **11**, 2289.

Meneses, J., T. Gharbi, and P. Humbert, 2005, Applied Optics **44**(7), 1207.

Mokso, R., P. Cloetens, E. Maire, W. Ludwig, and J. Y. Buffiere, 2006, Appl. Phys. Lett. Submitted.

Monnereau, C., and M. Vignes-Adler, 1998, Phys. Rev. Lett. **80**(23), 497.

Morawe, C., J. C. Peffen, and I. V. Kozhevnikov, 2003, J. Phys. IV **104**, 239.

Mullins, W. W., 1986, J. Appl. Phys. **59**(4), 1341.

Mullins, W. W., 1989, Acta Metall. **37**, 2979.

Neuhausler, U., G. Schneider, W. Ludwig, M. A. Meyer, E. Zschech, and D. Hambach, 2003, J. Phys. D - Appl. Phys. **36**(10A), 79.

von Neumann, J., 1952 (American society for metals, Cleaveland).

NIST, 2006, Nist scientific and technical databases, http://www.nist.gov/srd/physics.htm.

Nugent, A. G., A. G. Peele, H. N. Chapman, and A. P. Mancuso, 2003, Phys. Rev. Lett. **91**(20), 203902.

Op de Beeck, M., D. V. Dyck, and W. Coene, 1996, Ultramicroscopy **64**(1-4), 167.

Paganin, D., S. C. Mayo, T. E. Gureyev, P. R. Miller, and S. W. Wilkins, 2002, J. Microsc. **206**, 33.

Paganin, D., and K. A. Nugent, 1997, Phys. Rev. Lett. **80**(12), 2586.

Pereiro-Lopez, E., W. Ludwig, D. Bellet, P. Cloetens, and C. Lemaignan, 2005, Phys. Rev. Lett **95**, 215501.

Pfeiffer, F., C. David, M. Burghammer, C. Riekel, and T. Salditt, 2002, Science **297**, 230.

Pina, L., A. Inneman, and R. Hudec, 2000, in *Proceedings of the international congress on optical science, SPIE, San Diego*.

Protopopov, V. V., and K. A. Valiev, 1998, Optics Communications **151**(4-6), 297.

Radon, J., 1917, Sächs. Akad. Wiss. **69**, 262.

Ramm, A. G., and A. I. Katsevich, 1996, *The Radon Transform and Local Tomography* (CRC press, Boca Raton Florida).

Raoux, D., 1993, *Introduction to synchrotron radiation and to the physics of storage rings* (Springer-Verlag), volume 2, pp. 37–78.

Robinson, I. K., and J. W. Miao, 2004, MRS Bulletin **29**(3), 177.

Robinson, I. K., I. A. Vartanyants, G. J. Williams, M. A. Pfeifer, and J. A. Pitney, 2001, Phys. Rev. Lett. **87**(19), 195505.

Saint-Jalmes, A., and D. Langevin, 2002, J. Phys. Cond. Matt. **14**(40), 9397.

Salvo, L., 2005, http://www.gpm2.inpg.fr/perso/ls.html.

Schroer, C. S., P. Cloetens, M. Rivers, A. Snigirev, A. Takeuchi, and W. Yun, 2004, MRS Bulletin **29**(3), 157.

Schroer, C. S., and B. Lengeler, 2005, Phys. Rev. Lett. **94**, 054802.

Snigirev, A., V. Kohn, V. Snigireva, and B. Lenger, 1996, Nature **384**, 49.

Suzuki, Y., A. Takeuchi, H. Takano, and H. Takanaka, 2005, Jap. J. of Appl. Phys. Part 1. **44**(4A), 1996.

Talbot, H. F., 1836, Phil. Mag. **9**(56), 401.

Taylor, J. E., 1976, Ann. of Math. **103**, 489.

Teague, M. R., 1983, J. Opt. Soc. Am. **73**, 1434.

Thomas, G. L., R. M. C. de Almeida, and F. Graner, 2006, submitted.

Thomson (Lord Kelvin), S. W., 1887, Acta. Math. **11**, 121.

Turner, L. D., B. B. Dhal, J. P. Hayes, A. P. Mancuso, K. A. Nugent, D. Paterson, R. E. Scholten, C. Q. Tran, and A. G. Peele, 2004, Optics Express **12**(13), 2960.

Volkov, V. V., and Y. Zhu, 2003, Optics Letters **28**(22), 2156.

Wakai, F., N. Enomoto, and H. Ogawa, 2000, Acta Mater. **48**, 1297.

Weaire, D., and J. A. Glazier, 1993, Phil. Mag. Lett. **68**(6), 363.

Weaire, D., and R. Phelan, 1994, Phil. Mag. Lett. **69**, 107.

Weitkamp, T., C. Rau, A. Snigirev, B. Brenner, T. Gunzler, M. Kuhlmann, and C. Schroer, 2002, in *Proc. SPIE*, volume 4503, pp. 92–102.

Youn, H. S., and S. W. Jung, 2005, Phys. Med. Biol. **50**(22), 5417.

Yumoto, H., H. Mimura, S. Matsuyama, H. Hara, K. Yamamura, Y. Sano, K. Ueno, K. Endo, M. Yabashi, Y. Nishino, K. Tamasaku, T. Ishikawa, *et al.*, 2005, Rev. Sci. Instrum. **76**(6), 063708.

Zabler, S., P. Cloetens, J.-P. Guigay, J. Baruchel, and M. Schlenker, 2005, Rev. Sci. Inst. **76**, 073705.